Stimuli-Responsive Amphiphilic Peptides for Biomedical Applications

Inauguraldissertation

zur
Erlangung der Würde eines Doktors der Philosophie
vorgelegt der
Philosophisch-Naturwissenschaftlichen Fakultät
der Universität Basel

von

Severin J. Sigg

aus Zofingen, AG

Basel, 2016

Genehmigt von der Philosophisch-Naturwissenschaftlichen Fakultät der Universität Basel auf Antrag von

Prof. Dr. Wolfgang P. Meier (Universität Basel)
Fakultätsverantwortlicher / Dissertationsleiter

und

Prof. Dr. Nico Bruns (Université Fribourg)
Korreferent

Basel, den 19. April 2016

Prof. Dr. Jörg Schibler
Dekan

Summary

In the present thesis, the development of stimuli-responsive amphiphilic peptides for biomedical applications is described. The thesis is structured into four projects: (i) composite peptide–gold nanoparticle superstructures, (ii) reduction-responsive codelivery of antisense oligonucleotides and drugs, (iii) peptidic gene transfection, and (iv) reduction-responsive highly sensitive MRI contrast agents (Figure I).

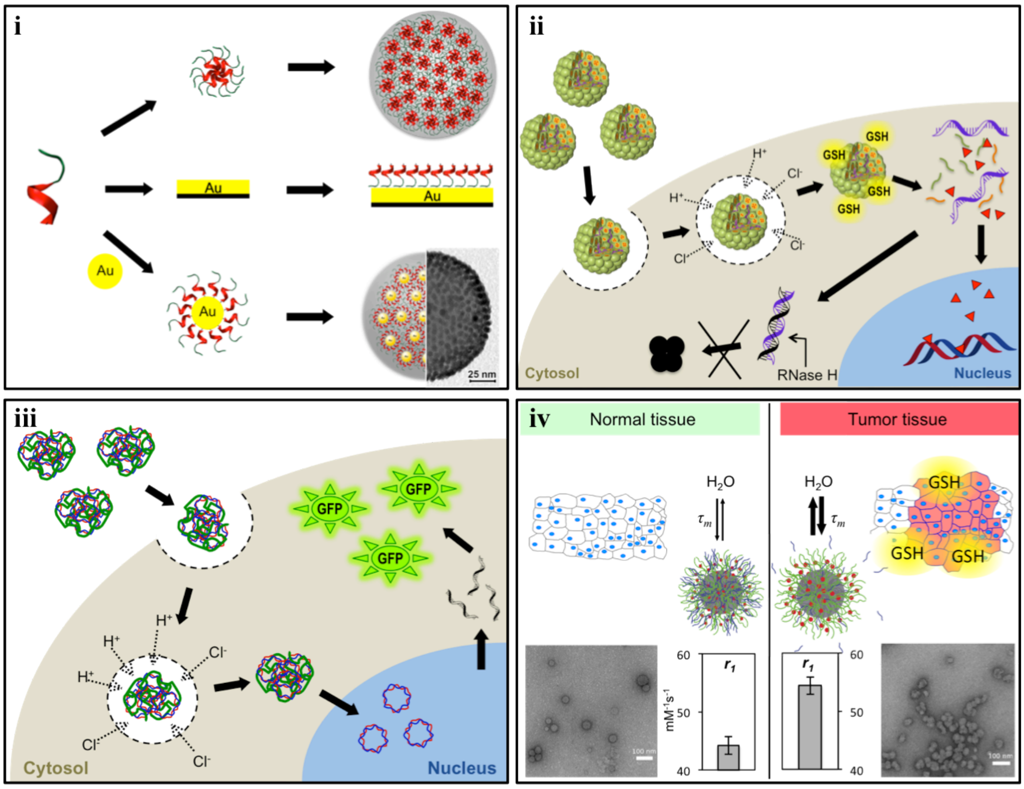

Figure I. Projects described in the present thesis. Adapted from Gunkel-Grabole et al.[1] and deBruyn et al.[2]

Chapter one comprises a general introduction to self-assembled systems in nature and their inspiration and influence on artificially designed functional nanomaterials. Further, concepts and recent achievements of nanoarchitectures for biomedical applications are introduced with focus on peptides as molecular building blocks, including assemblies based on gramicidin A derived amphiphilic peptides. It also contains a brief background of the underlying theory of magnetic resonance imaging (MRI) contrast agents, an overview of FDA-approved contrast agents, and recent advances regarding responsive MRI contrast agents. Furthermore, solid phase peptide synthesis is shortly introduced, and the aim of the thesis is presented.

Chapter two reports the development and investigation of amphiphilic peptides capable of forming composite peptide–gold superstructures (**Figure I–i**). Amphiphilic peptides based on a hydrophobic sequence derived from gramicidin A in conjunction with acetylated polylysine were modified with cysteines offering binding sites for covalent attachment to gold. Peptide-coated gold nanoparticles were able to self-assemble into ordered gold nanoparticle superstructures.

Chapter three addresses the elaboration of a reduction-responsive codelivery carrier for antisense oligonucleotides and small molecule drugs (**Figure I–ii**). Amphiphilic peptides were designed to bear nucleic acid binding units and hydrophobic sequences able to self-assemble into peptide nanoparticles incorporating desired payloads of different physicochemical characteristics. Introduction of a reduction-cleavable linker to the peptide sequence allowed triggered release of the cargoes at elevated levels of reduction potential.

Chapter four reveals peptidic gene transfection studies based on nanocarriers self-assembled from amphiphilic peptides comprising polylysine and polyhistidine sequences (**Figure I–iii**). The constructs were optimized for entrapment of GFP-encoding plasmid DNA, which subsequently served to assess the transfection performance via fluorescence levels. Transfection efficacies and effects on cells were investigated at various conditions.

Chapter five includes the development of highly sensitive magnetic resonance imaging contrast agents with contrast enhancement in reductive milieu (**Figure I–iv**). Gadolinium was complexed with heparin-poly(dimethylsiloxane) block copolymers and coassembled with a reduction sensitive amphiphilic peptide to form spherical nanoparticles. Magnetic resonance imaging contrast enhancement was examined simulating elevated levels of reduction potential, as found in tumor tissue, and compared to nontreated coassembled nanoparticles and a commercially available contrast agent.

Chapter six concludes the findings and achievements of the performed research. The results are discussed and promising further research directions are suggested and highlighted. Further, it comprises general statements regarding rational design of peptide sequences for controlled self-assembly and underlines their large potential towards biomedical applications.

Chapter seven summarizes materials and methods. Individual experimental setups for all presented research projects are described in detail, including source and grade of chemicals, origin of materials, devices, and instruments, as well as measurement parameter and formulae.

Content

List of Tables

List of Figures

List of Schemes

Abbreviations

%	Percent
°C	Degree Celsius
2D	Two-dimensional
3D	Three-dimensional
Å	Angstrom
a.u.	Arbitrary units
AA	Amino acid
ACN	Acetonitrile
AFM	Atomic force microscope
AON	Antisense oligonucleotides
AP	Amphiphilic peptide
Au-NP	Gold nanoparticle
BODIPY	Boron-dipyrromethene
BSA	Bovine serum albumin
Bzl	Benzyl
C	Concentration
CA	Contrast agent
CHCA	α-cyano-4-hydroxycinnamic acid
CLSM	Confocal laser scanning microscope
CM-PLH	Carboxymethyl poly-L-histidine
CMC	Critical micelle concentration
CP-Au-NPs	Composite peptide–gold nanoparticles
CPM	Counts per molecule
CPP	Cell-penetrating peptide
CT	Computer tomography
Da	Dalton
DCC	*N,N’*-dicyclohexylcarbodiimide
DCM	Dichloromethane
DDS	Drug delivery system
DIC	*N,N’*-diisopropylcarbodiimide
DIPEA	*N,N*-diisopropylethylamine
DMF	*N,N*-dimethylformamide
DMSO	Dimethyl sulfoxide
DNA	Desoxyribonucleic acid
DTPA	Diethylene triamine pentaacetic acid
DTT	Dithiothreitol
EDT	1,2-ethanedithiol
EDTA	Ethylenediaminetetraacetic acid
EMSA	Electrophoretic mobility shift assay
EPR	Electron paramagnetic resonance
EPR-effect	Enhanced permeability and retention effect
EtOH	Ethanol
Eq.	Equivalent
FACS	Fluorescence assisted cell sorting
FCCS	Fluorescence cross-correlation spectroscopy
FCS	Fluorescence correlation spectroscopy
FDA	Food and Drug Administration
Fmoc	9-fluorenylmethyloxycarbonyl
FTIR	Fourier transform infrared spectroscopy

G	Autocorrelation amplitude
g	Gyromagnetic factor
gA	Gramicidin-derived sequence
GAG	Glycosaminoglycan
Gd	Gadolinium
GFP	Green fluorescent protein
GSH	Glutathione
gT	Truncated gA
h	Planck constant
H	Spin Hamiltonian
HATU	*O*-(7-azabenzotriazol-1-yl)-*N,N,N',N'*-tetramethyluronium hexafluorphosphate
HBTU	2-(1*H*-benzotriazol-1-yl)-1,1,3,3-tetramethyluronium hexafluorophosphate
HCTU	2-(6-chloro-1*H*-benzotriazole-1-yl)-1,1,3,3-tetramethylaminium hexafluorophosphate
He-Ne	Helium-Neon
HEPES	4-(2-hydroxyethyl)-1-piperazineethanesulfonic acid
HF	Hydrogen fluoride
HOAt	1-hydroxy-7-azabenzotriazole
HOBt	1-hydroxybenzotriazole
HPLC	High performance liquid chromatography
IgG	Immunoglobulin G
IPE	Diisopropyl ether
k_B	Boltzmann constant
kDa	Kilo Dalton
k_{ex}	Water exchange rate
LB	Langmuir–Blodgett
LDL-C	Low-density lipoprotein cholesterol
M	Molar
Maldi-ToF-MS	Matrix assisted laser desorption/ionization - time of flight - mass spectroscopy
MCM	Multicompartment micelle
min	Minute
miRNA	Micro RNA
mL	Milliliter
mM	Millimolar
MmA	Mean molecular area
MRI	Magnetic resonance imaging
mRNA	Messenger RNA
ms	Millisecond
MTS	(3-(4,5-dimethylthiazol-2-yl)-5-(3-carboxymethoxyphenyl)-2-(4-sulfophenyl)-2*H*-tetrazolium)
mW	Milliwatt
MWCO	Molecular weight cut-off
N	Number of particles
n	Refractive index
NP	Nanoparticle
N/P-ratio	Nitrogen-to-phosphorus ratio
NIR	Near infrared
nm	Nanometer
nM	Nanomolar
NMR	Nuclear magnetic resonance
PA	Peptide amphiphile
PAMAM	Polyamidoamine

PB	Poly(butadiene)
PBMA	Poly(butyl methacrylate)
PBS	Phosphate buffered saline
PDMA	Poly(*N,N*-dimethylacrylamide)
PDMAEMA	Poly[(2-dimethylamino)ethyl mathacrylate]
PDMS	Poly(dimethylsiloxane)
pDNA	Plasmid DNA
PEG	Poly(ethylene glycol)
PEI	Polyethylenimine
pH	Potential hydrogen
pK_a	Logarithmic acid dissociation constant
PLGA	Poly(lactic-co-glycolic acid)
PLL	Poly-L-lysine
P_m	Mole fraction of water coordinated to metal center
PM-IRRAS	Polarization modulation infrared reflection absorption spectroscopy
PMCL	Poly(γ-methyl-ε-caprolactone)
PMOXA	Poly(2-methyloxazoline)
PPAA	Poly(propylacrylic acid)
PPI	Poly(propylene imine)
PS	Polystyrene
PyBOP	Benzotriazol-1-yl-oxytripyrrolidino-phosphonium hexafluorophosphate
q	Number of bound solvent molecules
QCM	Quartz crystal microbalance
R	Radius
r.t.	Room temperature
r	Relaxivity
R_1	Longitudinal relaxation rate
R_2	Transverse relaxation rate
R_g	Radius of gyration
R_h	Radius of hydration
RP	Reversed phase
s	Second
SAM	Self-assembled monolayers
SEM	Scanning electron microscopy
shRNA	short hairpin RNA
siRNA	Small interfering RNA
SLS	Static light scattering
SPION	Superparamagnetic iron oxide nanoparticle
SPPS	Solid phase peptide synthesis
ssDNA	single stranded DNA
T	Temperature
T	Tesla
t	Time
T_1	Longitudinal relaxation time
T_2	Transverse relaxation time
T_{2e}	Transverse electronic relaxation time
Tat	Transactivator of transcription
tBoc	Tert-butyloxycarbonyl
TEM	Transmission electron microscopy
TES	Triethylsilane
TFA	Trifluoroacetic acid
TSG	Template-stripped gold

V	Volt
v	Volume
w	Weight
X	Acetylated lysine
ZFS	Zero-field splitting
γ	Nuclear gyromagnetic ratio
ΔH_{pp}	Peak to peak line width
λ	Wavelength
μ_B	Bohr magneton
µL	Microliter
µm	Micrometer
µM	Micromolar
µs	Microsecond
τ_{ci}	Dipole-dipole relaxation correlation time
τ_D	Diffusion time
τ_M	Mean water residence time
τ_R	Rotational correlation time
ω	Beam waist radius
ω_I	Nuclear precession frequency
ω_s	Electron precession frequency

Amino Acids

A	Alanine
C	Cysteine
D	Aspartic Acid
E	Glutamic Acid
F	Phenylalanine
G	Glycine
H	Histidine
I	Isoleucine
K	Lysine
L	Leucine
M	Methionine
N	Asparagine
Q	Glutamine
R	Arginine
S	Serine
T	Threonine
V	Valine
W	Tryptophan
X	Acetylated lysine
Y	Tyrosine

Chapter 1

1 Introduction

The first chapter provides a general introduction to the fields of self-assembly, molecular design, responsive nanomaterials, and their applications in biomedicine, such as for drug and/or gene delivery and as magnetic resonance imaging contrast agents. A special focus is laid on nanostructures built from pure peptides including their advantages compared to other materials. The chapter further encloses a brief introduction to solid phase synthesis as well as a subchapter comprising the scope of the present thesis.

Parts are adapted from Biomaterials Science:

Gunkel-Grabole, G.; Sigg, S.; Lomora, M.; Lörcher, S.; Palivan, C. G.; Meier, W. P. Polymeric 3D nano-architectures for transport and delivery of therapeutically relevant biomacromolecules. *Biomater. Sci.* **2015**, 3, (1), 25-40, with permission from the Royal Society of Chemistry.

Parts are adapted from Chimia:

Sigg, S. J.; Schuster, T. B.; Meier, W. P. Self-assembled Structures from Amphiphilic Peptides. *Chimia* **2013**, 67, (12), 881-884. © 2013, Swiss Chemical Society.

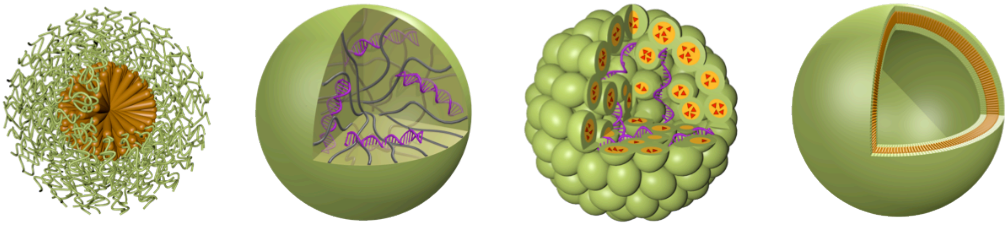

Figure 1. Various self-assembly architectures. Introduced and described in more detail in the following chapter.

1.1 Self-Assembly – The Basis of Life

Why is it necessary to understand self-assembly to understand life? Autonomous organization of components to form structures without external intervention is known as self-assembly. Self-assembly encloses all length scales – from molecular dimensions to planetary systems, galaxies and beyond. It is expressed by the order of systems and is represented by numerous essential mechanisms in nature. Biologic processes are mainly based on highly organized structures. Of particular importance regarding life-essential self-assemblies is the double stranded DNA – the "construction plan" of biological systems. Its nucleotide building blocks can bear four different nucleobases and are coupled in unique sequences encoding for a multitude of functional and regulatory biomolecules. Specific nucleic acids initiate the production of enzymes and proteins, which then form secondary, tertiary and quaternary structures defining their functionality in the living system. Moreover, self-assembly is the underlying physicochemical mechanism for the formation of phospholipid bilayers, essential for creation of confined space in living organisms, for instance in cell walls and compartmentalization inside cells.[3]

1.2 Synthetic Self-Assemblies

In the past decades, numerous material scientists transferred the evolutionary success of nature about self-organization towards the creation of hierarchical structures with tailored properties. Microstructures were initially built by reduction of size, so called "top-down" fabrication, usually generated by lithographic techniques. As top-down approaches reached their limits at about one micrometer, it became increasingly clear that fundamental understanding of self-assembly in biological structures is necessary to close the gap between the nanometer size molecules produced by chemical synthesis and nanoparticles formed by top-down fabrication. The "bottom-up" approach was developed. It deals with the design of molecular structures able to interact due to mutual recognition properties based on noncovalent bonding. Contributing molecular forces are mainly electrostatic and hydrophobic interactions as well as π–π-stacking. Assembling instructions for larger structures are encoded within structural motifs and affinities of the molecular building blocks. DNA origami, for instance, nicely represents the bottom-up approach of self-assembling nanostructures to build various three-dimensional objects (Figure 2).

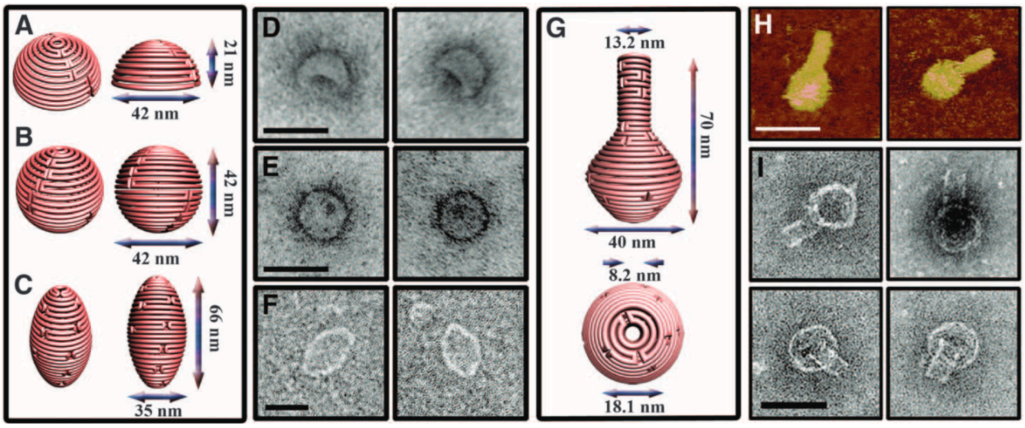

Figure 2. Engineering self-assembling three-dimensional nanoobjects from DNA using DNA origami technique. From Han et al., *Science* (2011).[4] Reprinted with permission from AAAS.

Appropriate molecular design can yield a variety of supramolecular assembly architectures such as micelles, fibers, tubes, multicompartment micelles, vesicles, planar membranes, and lamellar structures (Figure 3). Micelles are spherical objects formed by amphiphilic molecules in aqueous solution. This process is driven by an enhanced level of free energy due to the exposure of hydrophobic moieties to water. To overcome this, the molecules begin to orient themselves, hiding hydrophobic parts in a core surrounded by hydrophilic corona. In vesicles, nanocompartmentalization occurs by separation of the inner medium from its exterior by lipid (liposomes),[5,6] polymer (polymersomes),[7-10] or peptide membranes (peptosomes).[11-13] The cavity is appropriate for sheltering fragile biomolecules such as proteins and enzymes, or to lock up soluble toxic payloads.[14] Moreover, when permealizing the vesicle membranes they have been shown to function as nanoreactors.[15-17] Many of these approaches are nature inspired and adapted from lipid membranes. Lipid membranes are omnipresent in nature and serve as a role model for the design of synthetic analogues with improved stability and functionality.[18]

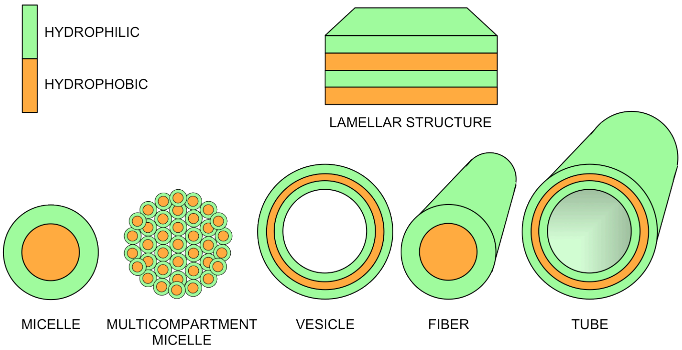

Figure 3. Common architectures of self-assembling amphiphiles. Hydrophilic-to-hydrophobic ratio, chemical and physical properties of the blocks, and assembly conditions among other parameter influence the self-assembly process.

1.2.1 Peptides

Peptides represent a special class of self-assembling molecules due to their ubiquitous appearance as proteins or enzymes, where they exhibit extraordinary folding skills leading to defined tertiary structures. In biomedical applications, such as drug delivery, artificially designed peptides are very promising candidates. This is due to their inherent biocompatibility and biodegradability but also because of the ease of synthesis, functionalization, and their defined molecular structure. The building units are amino acids. There are 20 canonical amino acids used in natural biological systems. With the exception of glycine, all are chiral and hence can have two configurations, although generally only the L-configuration is of biological importance. Depending on their sequence, peptides form ordered secondary structures such as α-helices or β-sheets, stabilized by noncovalent interactions such as hydrogen-bonding, π–π-stacking, and ionic and hydrophobic interactions (Figure 4). Due to the large variety of building units, a nearly endless number of unique peptides can be designed, each with its three-dimensional conformation and properties.

In past decades, many peptide-based materials have been investigated, the main groups being peptide amphiphiles (PAs)[19,20] and amphiphilic peptides (APs). The latter consist solely of amino acids, in contrast to peptide amphiphiles, which comprises other groups such as alkyl chains, phospholipids and polymers.[21,22] There are several recently published reviews covering the field of PAs.[19,21]

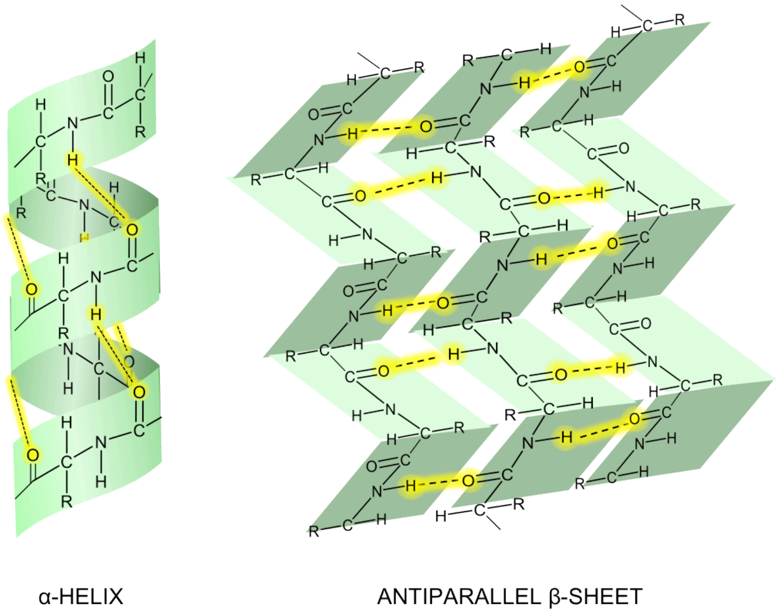
α-HELIX

ANTIPARALLEL β-SHEET

Figure 4. Common secondary structures of peptides stabilized by hydrogen bonding (marked in yellow). The α-helix (left) is righthand-coiled and stabilized by hydrogen bonding from N–H to the C=O four residues earlier. β-sheets (right) are laterally connected by hydrogen bonds.

The sequence of amphiphilic peptides is organized into two regions: the hydrophobic and the hydrophilic. The latter is predominantly occupied by charged and polar amino acids; these are: arginine (R),[23,24] histidine (H),[24,25] lysine (K),[26-32] aspartic acid (D),[33,34] glutamic acid (E),[11,28] serine (S), threonine (T),[35] asparagine (N), glutamine (Q),[36] and cysteine (C).[30] The design of the former region is based on amino acids with neutral and nonpolar side-chains such as glycine (G),[33] alanine (A),[32,37] valine (V),[34,38] leucine (L),[26,34] isoleucine (I),[39] methionine (M), phenylalanine (F),[40,41] tyrosine (Y), and tryptophan (W).[24,27-31,41] Depending on the hydrophobic to hydrophilic ratio and the sequence, various self-assembled structures can be constructed – as indicated in the associated references for the above amino acids – although the hydrophobicity is moderated by the polar character of the peptide backbone.

Nanomaterials created from those amphiphiles allow additional tuning towards the required functions and properties by design and functionalization of sidechains and endgroups. Every amino acid has its benefits; cysteine, for instance, can be used as a connection point for labeling or to covalently attach gold. Mastrobattista's group presented studies of conical shaped amphiphilic peptides self-assembling into vesicles with a hydrodynamic radius of about 60 nm.[11] Their sequences consist of A, L, V, and W for the hydrophobic moity, and various lengths of glutamic acid as the hydrophilic region. Gazit et al. reported short aromatic Fmoc-peptides that form spheres, tubes, and fibrils.[42] Zhang's group published work about surfactant-like peptides, which can self-assemble into vesicles and fibers.[33]

In our group, various different *de novo* designed peptides have been created and investigated (Figure 5). All peptides were designed based on a hydrophobic sequence derived from gramicidin A, an antibiotic that inserts into lipid membranes. The sequence and secondary structure of gramicidin was investigated by Sarges et al.[43] Hydrophobicity is generated by its helical secondary structure, hiding the peptide's backbone from its surrounding milieu. This knowledge can be adapted to a variety of amphiphilic peptides. Based on the native sequence, two hydrophobic sequences were developed, namely gA (-V-G-A-DL-A-DV-V-DV-[W-DL]$_3$-W-NH_2) and a truncated version gT, comprising only the L-tryptophan-D-leucine repeating unit (-[W-DL]$_3$-W-NH_2). Both, the gA and gT hydrophobic segments have a C-terminal amide group. Circular dichroism and infrared spectroscopic investigations revealed a secondary structure that included a β-turn motif and hydrogen bonds for the gT hydrophobic sequence.[31,44] The crucial influence of secondary structure on their self-assemblies was shown by replacing D-leucines with L-leucines, whereby the gT hydrophobic sequence changed its secondary structure such that amphiphilic nature was no longer present, leading to amorphous assemblies.[31] Charged or polar amino acids such as lysine, acetylated lysine (X), and/or glutamic acid served as the hydrophilic sequences.

Oligopeptides comprising trilysine hydrophilic regions, form micelles with hydrodynamic radii of about 10 nm. They similarly exhibit a surfactant-like behavior, e.g. the critical micelle concentration (CMC) is 0.23 mmol L^{-1}.[29] Decreasing the number of charges by acetylating the lysines in the hydrophobic sequence lowers the overall hydrophilicity owing to the formation of spherical objects in the sub-micrometer range. The formation process proceeds over micelles, which then aggregate with decreasing ethanol content to form peptide nanoparticles.

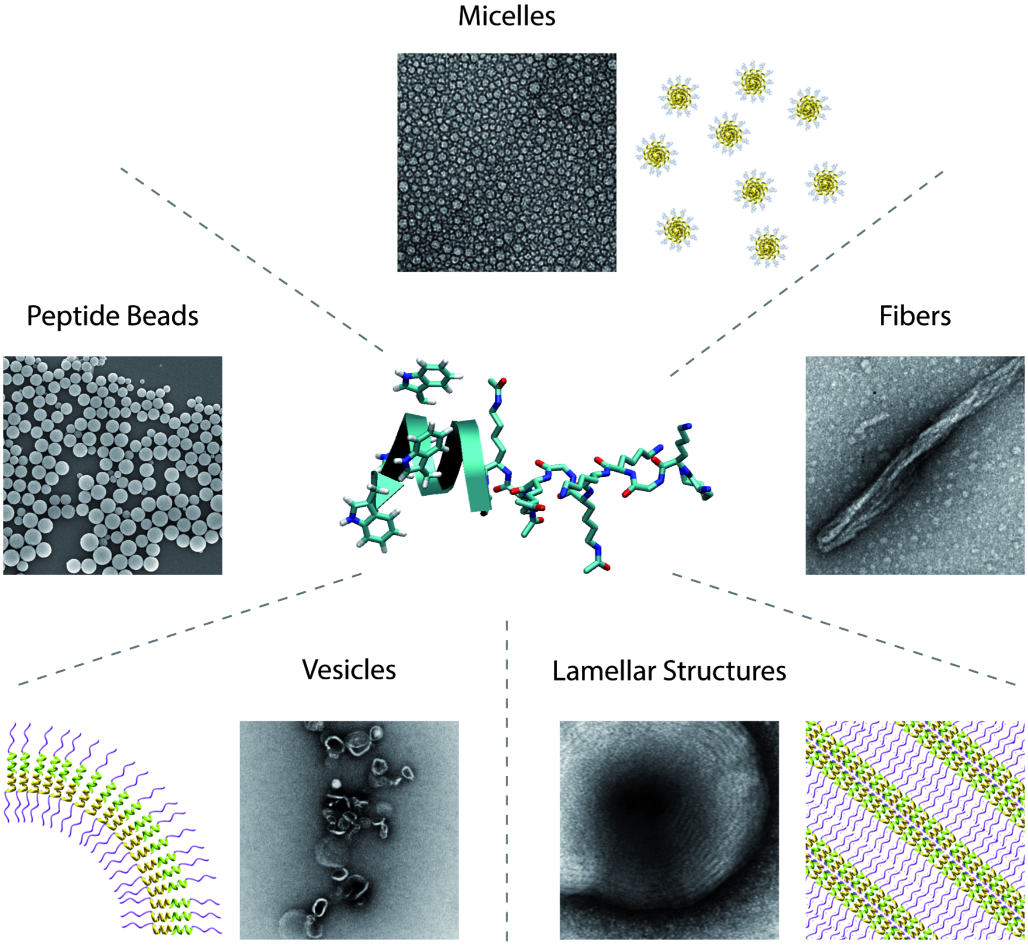

Figure 5. Overview of self-assembled structures using amphiphilic peptides ranging from micelles, fibers, vesicles and lamellar structures to spherical nanoparticles. Reproduced from Sigg et al.[45]

To understand the impact of changes in the primary sequence on self-assembly a library of peptides were produced systematically changing properties. Beginning with K8gA, the lysines were successively acetylated to AcX8gA, comprising no charges and therefore no electrostatic repulsion. Interestingly, between K2X6gA and K3X5gA the secondary structure of the hydrophilic region changed dramatically from β-sheets to α-helices, accompanied by different properties. K2X6gA was self-assembling into fibers with a length ranging from 30 to 800 nm while K3X5gA formed micelles and worm-like micelles.[27] These results concur with recently published studies by Lee and coworkers.[46] According to those studies, peptides with β-sheet secondary structure preferentially form fibers, due to the stacking of the radially ordered unimers. The micellar core also provides space for hydrophobic drug encapsulation and can thus be used as drug delivery system.[47-49]

To create polymersomes or polymeric membranes block-copolymers are regularly used, including poly(2-methyloxazoline)-*b*-poly(dimethylsiloxane)-*b*-poly(2-methyloxazoline) (PMOXA-*b*-PDMS-*b*-PMOXA),[17] polyethyleneglycol-*b*-poly(γ-methyl-ε-caprolactone) (PEG-*b*-PMCL),[50] poly(ethylene glycol)-*b*-poly(γ-methyl-ε-caprolactone)-*b*-poly[(2-dimethylamino)ethyl methacrylate] (PEG-*b*-PMCL-*b*-PDMAEMA),[51] and poly(butadiene)-*b*-poly(ethylene glycol) (PB-*b*-PEG).[52] Similarly, peptidic analogues can be constructed. For tuning amphiphilic peptides based on gA or gT hydrophobic sequences to form peptosomes, hydrophobic interactions and geometrical parameters have to be adjusted and optimized. Masking the C-terminal amide of fully acetylated AcX8gA by esterification (AcX8gA-OEt) led to the formation of vesicles. Improving perpendicular interaction with respect to a membrane facilitated membrane formation. Additionally, an increase of lateral interactions similarly promoted the formation of membranes. Replacing the hydrophilic sequence with hexaglutamic acid allowed intermolecular interaction of the carboxylic group, which stabilized the formation of micelles and vesicles.[53,54] From a conceptual point of view, peptide membranes are fascinating as analogues to lipid and polymer membranes. However, the low number of publication may illustrate the challenges associated, in particular when using short, amphiphilic oligopeptides. Nevertheless, encapsulation properties of such amino acid based materials may allow their use as a drug and gene delivery vehicles.[55] In this respect, proven polymersomes concepts, such as targeting, may also lead to a fast development of advanced peptosomes.[56,57] The variety within the amino acid alphabet opens a vast playground for controlling self-assembly. By introducing desired interactions such as hydrogen bonds and charge compensation, highly ordered organizations can be created.[58,59]

Shorter variants of the acetylated peptides (AcX3gT) yielded spherical nanoparticles.[30,31] Characterization of the nanoparticles exhibited a particle scattering factor and a ρ-parameter (R_g/R_h) that confirm the beads to be solid spheres.[29,30] Their density was determined to be about 1.4 g cm^{-3}.[30,31] Their size was dependent on the initial peptide concentration, ranging from a diameter of 260 to 800 nm.[30] Underlying self-assembly process and inner structure of the peptide nanoparticles are based on micelles, which then aggregate in a controlled manner to form highly spherical nanoparticles (Figure 6).

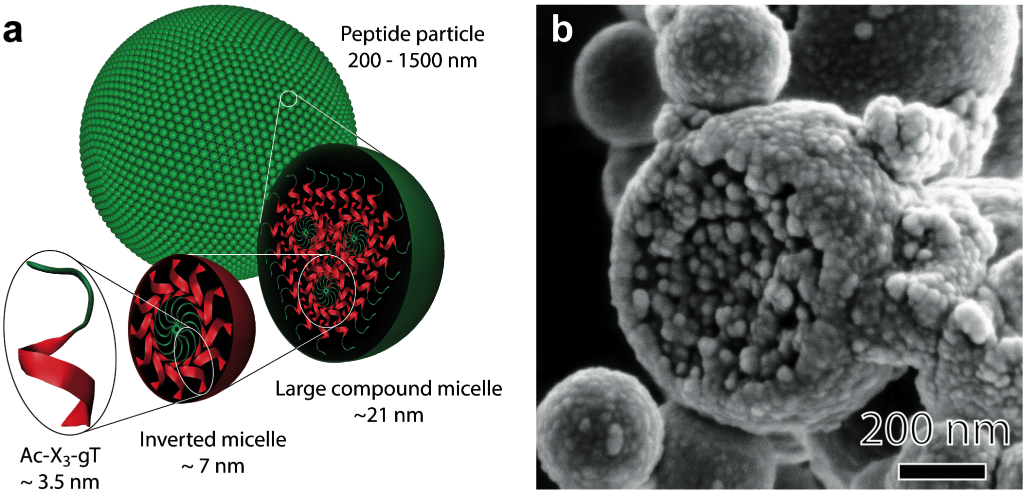

Figure 6. Hierarchical self-assembly of AcX3gT into multicompartment micelles (a). SEM micrograph of an AcX3gTC peptide nanoparticle, revealing insight into the inner structure (b). Reproduced from Sigg et al.[45]

Based on the available data they have been hypothesized to be multicompartment micelles (MCM).[30] Multicompartment micelles exhibit outstanding properties and are therefore attractive for a broad variety of applications in nanotechnology.[60-62] Similarly, peptidic analogues provide new opportunities concerning drug delivery applications and functional materials.

1.3 Drug/Gene Delivery

Nanotechnology provides a vast array of opportunities and tremendous promise for the rational design of multifunctional drug delivery systems. Nanocarriers are designed for delivery of therapeutics: protecting them from being metabolized,[63,64] enhancing bioavailability,[65,66] lowering off-target effects, and decreasing the necessary drug dose by increasing accumulation at the diseased site. Ideally, drug delivery systems have sizes of 100 to 200 nm[67,68] to avoid excessive clearance by phagocytic cells in liver and spleen,[69,70] and renal filtration.[71] Further improvement of efficacy can be achieved by utilizing physiological microenvironments at pathological sites such as pH,[72-75] temperature,[76] and redox potential[77,78] as release triggers.

1.3.1 Nanocarrier Architecture

To develop nanocarriers capable of delivering drugs and/or genes with high efficiency the carrier architecture is a crucial factor. Although there is no gold standard nanocarrier design, numerous publications in the field allow drawing trends and conclusions. Importantly, the chemical structure, size and properties of the desired payload, as well as the target location in the body play an important role in choosing the right nanocarrier design. They can be divided into four main groups independently of their chemical nature: dendrimers, micelles, vesicles, and nanoparticles (Figure 7). Each design bears advantageous individual features matching the needs of specific applications. Building blocks can be made of diverse chemical compositions comprising lipids, polymers, peptides, and inorganic materials. Important properties arising from the underlying molecular design are size, functional groups, nature of compartmentalization, surface properties, stability, compatibility, and degradability among others.

Dendrimers are normally synthesized to 4th or 5th generation for biomedical applications. The comparably small constructs are monodisperse, therefore well defined single molecules, which exhibit high stability and the ability be chemically modified with payload binding or recognition moieties. On the other hand, based on the small sizes, *in vivo* application usually lacks efficiency due to rapid clearance via renal pathways. Furthermore, dendrimers developed for delivering nucleic acids revealed high cytotoxicity because of the high charge density disrupting cell membranes.[79,80] Similarly, micelles exhibit rather small sizes for *in vivo* applications dependent on the length of the single molecules. However, the assembly architecture offers a hydrophobic environment in the core, allowing entrapment of hydrophobic payload.[47,48,81] In contrast, vesicular constructs bear a hydrophilic inner cage with larger spatial dimensions compared to micelles. The larger volume of the inner cavity enables the delivery of higher doses; furthermore, renal clearance is avoided. However, reaching diameters above 200 nm considerably large amounts of the applied constructs are being removed from the blood stream by phagocytosis. For drug delivery purposes the stability of vesicles is a major issue. Originally built from lipids inspired by nature, vesicles were increasingly designed from polymers and peptides revealing higher stabilities.[10,82] Spherical nanoparticles enclose all remaining nanoscale assembly architectures, which are not specifically defined. The assembled nanostructures are usually described via size, shape and abilities to entrap and release drugs and/or genes, rather than via specific bottom up molecular self-assembly.[83-87]

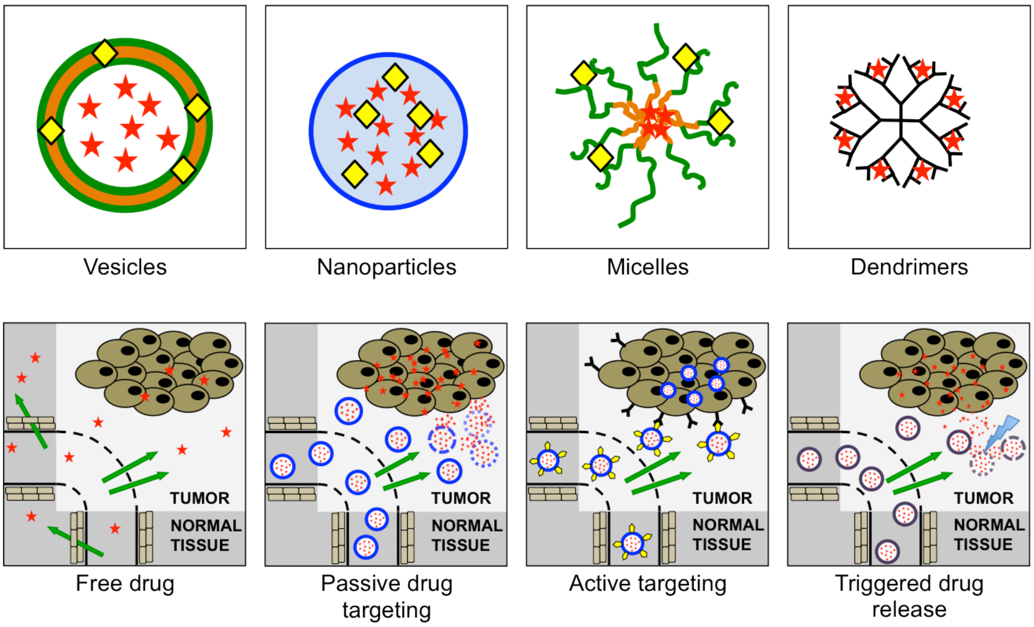

Vesicles Nanoparticles Micelles Dendrimers

Free drug Passive drug targeting Active targeting Triggered drug release

Figure 7. Different architectures of drug delivery devices (top row). Strategies to deliver drugs compared to the application of free drugs (bottom row).

1.3.2 Stimuli-Responsiveness

The efficiency of drug delivery systems is often limited by the control of the release of the payload. Nonspecific release follows the Fickian diffusion and is not sufficient for many applications. Furthermore, systemic biodistribution of the nanocarriers alters efficacy of the delivered drugs by nonspecific release. More efficient strategies include on-demand processes, which enable control over the drug release profile. On-demand drug delivery can be achieved by endogenous or extracorporeal stimuli. Former targets distinct physiologic microenvironments at pathological sites such as pH, redox potential, temperature, or concentration of certain enzymes, and reacts by releasing the payload. Latter involves extracorporeal physical stimuli including light, temperature, and ultrasound.[88]

pH-responsive systems are designed to react to elevated proton concentrations. The pH of extracellular environments of solid tumors (6.5–7.2) is slightly lower compared to healthy tissue (~7.4).[88] In order to obtain an efficient release of payload, the nanocarrier must be designed to give a sharp response to this small change in pH. For example, PEG-poly(amino ester) micelles were reported to release camptothecin upon a pH change to 6.4.[89] Other acidic compartments develop during the endocytotic cell uptake pathway. The pH drops gradually from early endosomes (6.5) to late endosomes (~6.0) to lysosomes (4.5–5.0).[90] Complexes of styrene-maleimic acid copolymer and the anticancer drug cisplatin revealed much faster *in vitro* release at pH 5.5 compared to physiological pH (7.4).[91] pH-responsive release of small molecule drugs at acidic conditions was also reported for poly(β-amino ester)-capped mesoporous silica nanoparticles[92] and core cross-linked polyphosphoester micelles.[93] Another study describes hollow chitosan-silica nanospheres that reveal faster release profiles of bovine serum albumin, as a model enzyme, at pH 4.0 compared to physiological conditions.[94]

Inflamed areas and tumors are often hyperthermic,[76] thus differing in temperature compared to healthy regions in the body. In order to develop effective nanocarriers exploiting this small temperature differences a sharp change in properties with temperature is required. Nanocarrier designs involving poly(*N*-isopropyl acrylamide) demonstrated improved drug release at hyperthermic regions due to a lower critical solution temperature close to body temperature.[95-100] Other architectures include thermo-responsive poly(amino acid)-based micelles,[101] block copolymer coated magnetic iron oxide nanoparticles,[102] and various liposome designs.[103]

Redox sensitive drug delivery systems react to intracellular glutathione (GSH) concentrations that are three orders of magnitude higher (2–10 mM) compared to extracellular levels (2–10 μM). Reduction-triggered release is also promoted by higher reduction potential in tumor tissue compared to healthy tissue. The development of reduction sensitive drug delivery systems is focused, but not limited to disulfide linkages cleavable by GSH. Recent studies report disulfide cross-linked polymeric micelles designed to deliver the anticancer drugs doxorubicin,[104] paclitaxel,[105] methotrexate,[106] and vincristine,[107] as well as DNA[108] with high efficiencies. Other examples include bioreducible systems based on heparin nanogels that release doxorubicin after addition of GSH[109] and peptide amphiphile-capped mesoporous silica nanoparticles that release doxorubicin after addition of physiological concentrations (10 mM) of dithiothreitol (DTT).[110]

Light-triggered drug delivery systems are responsive to illumination with light in the ultra violet (UV), visible, or near infrared (NIR) region.[111] UV- and visible-light responsive drug delivery systems utilize *cis–trans* isomerization of azobenzene derivates,[112-114] spiropyran–merocyanine isomerization,[115] and photodimerization–cleavage cycles of thymine,[116] among others. However, UV and visible light induced drug release is limited by the low penetration depth due to strong scattering inside soft tissues, thus only applicable to eyes and skin. Drug delivery systems triggered by light in the NIR-region has the advantages of deeper tissue penetration and minimal harm to tissue. The thermoplasmonic properties of gold nanoparticles provide a promising platform for NIR-induced drug release. Examples include NIR-triggered release of a model drug[117,118] or doxorubicin[117] from mesoporous silica-coated gold nanorods, release of single stranded DNA (ssDNA) from gold-coated silica nanoparticles via dehybridization,[119] and controlled release from polyelectrolyte coated gold nanorods.[120]

1.3.3 Nucleic Acid Delivery

Besides small molecule drugs, nucleic acids, such as plasmid DNA (pDNA), short interfering RNA (siRNA), and therapeutic antisense oligonucleotides (AON) demand for multifunctional delivery systems. For delivery, nucleic acids are condensed to smaller sizes using polycations such as polyethylenimine (PEI), poly-L-lysine (PLL), spermidine, histones, and other cationic lipids, peptides or polymers. Enhancement of cell uptake can be achieved by recognition sequences or specific moieties interacting with cell membranes. These can be directly included in the sequence of peptides used for nanoparticle formation while for polymeric systems they need to be coupled post-synthesis. Naturally occurring cell-penetrating peptides (CPPs) like RGD, polyarginine, MPG, MAP, KALA, pVEC, and Tat are often used in this respect (Table 1). Successful DNA delivery has been reported with modified pVEC,[121] and KALA peptides modified with an additional RGD cell adhesion motif.[122] Efficient transfection was obtained using peptide amphiphiles bearing both an RGD sequence and an octaarginine (R8) cell penetrating peptide.[123] To improve the localization of nanocarriers, specific targeting to LHRH-receptors (usually overexpressed in breast cancer cells)[124] was achieved with lysine- and histidine-rich peptides.[25] pH-triggered release of DNA was facilitated by using nanoparticles of carboxymethyl poly-L-histidine (CM-PLH) and poly-β-amino ester. The CM-PLH coating significantly decreased the cytotoxicity and at the same time improved the specific localization at tumor sites due to the enhanced permeability and retention effect (EPR effect).[125] Dendronized polypeptides, containing histidine, phenylalanine, and a backbone bearing disulfide bonds were able to release siRNA upon reduction.[126] Moreover, KALA peptides decorated with RGD-moieties were used to condense DNA. These peptides were oligomerized to obtain di-, tri-, and tetramers via a disulfide linker during the formation process, which subsequently acted as reduction sensitive part of the nanoparticles.

Table 1. Names and Sequences of Cell-Penetrating Peptides. Sequences are Noted According to the Mentioned References. Length of Sequences may Differ From Other Literature.

code/name	sequence	reference
RGD	RGD	123
MPG	GALFLGFLGAAGSTMGAWSQPKKKRKV	127
MAP	KLALKLALKALKAALKLA	127
KALA	WEAKLAKALAKALAKHLAKALAKALKACEA	127
pVEC	LLIILRRRIRKQAHAHSK	121
R8	RRRRRRRR	123
R9	RRRRRRRRR	128
Tat	GRKKRRQRRRPPQ	127
PTD4	YARAAARQARA	128
Transportan	GWTLNSAGYLLGKINLKALAALAKKIL	128

Besides, nucleic acid cargo can also be delivered and released from polymeric nanoparticles. Linear cationic click polymers containing disulfide bonds, secondary amine groups, and amide–triazole moieties were reported to deliver and release pDNA in a reductive environment, if the DNA had been condensed with PEI first.[129] Moreover, efficient delivery of a nucleic acid payload to mesenchymal stem cells, which is of high interest in regenerative medicine, was recently reported.[128,130] In this study, a pH-responsive diblock copolymer composed of PDMAEMA, poly(butyl methacrylate) (PBMA) and poly(propylacrylic acid) (PPAA) was used to form nanoparticles of siRNA and the copolymer. In addition, successful dual gene knockdown in ovarian tumors *in vivo* is described for short hairpin RNA (shRNA) condensed with PLL/PLGA nanoparticles.[131] In addition to purely peptidic and purely polymeric systems, polymer-protein conjugates can also form nanoparticles and deliver pDNA, as shown for example using BSA-poly(dimethylamino) ethyl methacrylate (PDMA) based nanoparticles.[132]

To date, a variety of nanoparticles have been developed and proved their functionality *in vitro*. However, only a few of them also showed applicability *in vivo*.[124,125,129,131,133,134] Despite favorable effects on internalization, positively charged nanoparticles tend to agglomerate upon contact with serum proteins, leading to accumulation in thin capillaries and ultimately cause blockage of the blood stream. Further, a balance has to be kept between the several desirable requirements for drug delivery systems and the need to reduce the complexity of assembled nanoparticles. This is of particularly importance to avoid possible sources of error since the preparation process is statistical.

Antisense oligonucleotides represent a special form of therapeutic nucleic acids. AON are typically short single-stranded oligonucleotides with about 20 bases and backbones that are usually chemical modified phosphothioate linkages between the nucleosides to obtain better stability.[135] They inhibit target mRNA by Watson-Crick base pairing leading to down-regulation of protein production. For the delivery of AON, two main strategies are followed: either synthetically conjugated to the carrier or noncovalently condensed.[63] Covalent strategies were recently reviewed and describe the linkage of lipids, peptides, carbohydrates and small molecule moieties to the 5' or 3' positions of the AON.[136] The bound moieties should not interfere with the binding to target RNA to obtain efficacious delivery systems. Noncovalent condensation is achieved via electrostatic interaction with the negatively charged backbone of the AON to positively charged carrier molecules. Noncovalent nanocarriers for AON delivery are usually better able to cross cell membranes and deliver the cargo than conjugated ones.[137] Mipomersen is the first FDA-approved AON drug targeting the mRNA encoding for a protein involved in the production of the low-density lipoprotein cholesterol (LDL-C), also called bad cholesterol. Clinical studies showed 25% lower LDL-C levels in patients with homozygous familial hypercholesterolaemia.[135] Further AON drugs are curstirsen, which targets an upregulated protein in prostate cancer, and fomivirsen, for the treatment of cytomegalovirus-induced retinitis for patients with AIDS.[135]

1.3.4 Combined Treatments

Many studies about combined treatment with different therapeutics (drug–drug, drug–nucleic acids) showed very promising synergistic effects. To exploit the full potential of combined treatments, multifunctional delivery systems must be capable of delivering various kinds of payloads simultaneously to the desired place. This can be a combination of small molecule drugs, which exhibit a synergistic characteristic when applied in combination. For instance, combined treatment with the anticancer drugs dihydroartemisinin and doxorubicin, revealed synergistically increased inhibition of cell proliferation.[138] Synergistic effects were also observed for the treatment of prostate cancer with a combination of the flavonoid vicenin-2 and docetaxel.[139] A further example is the use of small doses of curcumin and paclitaxel, which showed synergistic effects in the treatment of the highly chemo-resistant human brain tumor stem cells.[140] Synergistic characteristics were also shown for combinations of micro RNA (miRNA) with small molecule anticancer drugs such as gemcitabine, doxorubicin, doxetaxel, epirubicin, and adriamycin[141] as well as for oligonucleotides combined with anticancer drugs 5-fluorouracil, gemcitabine, paclitaxel, vinorelbine ditartrate, or irinotecan.[142] A recent report describes tenfold increased doxorubicin efficiency when codelivered in liposomes with siRNAs targeting antiapoptotic cellular defense and multidrug-resistance, compared to free and liposomal doxorubicin.[143] However, the major obstacles constructing nanocarriers for drug delivery applications are a lack of biocompatibility and biodegradability as well as the stimuli-responsive release triggered by physiological microenvironment at the site of disease.

1.3.5 Self-Assembling Peptides – Promising Drug Carriers

Peptides are very promising candidates to be used for self-assembling nanostructures for biomedical applications. Increasing understanding of protein folding mechanisms facilitates rational design of peptide sequences to self-assemble into predefined structures. The assembly process is driven by inter- and intramolecular interactions such as electrostatic and hydrophobic interactions, hydrogen bonds, π–π stacking, and van der Waals forces. Peptides were created to self-assemble into micelles,[144,145] vesicles,[11,146,147] fibers,[148,149] and spheres.[2,31] The relatively low synthesis effort and the extraordinary versatility of designs, based on amino acid sequences are just two among other advantages over other materials. Furthermore, naturally occurring peptide sequences with defined secondary structures, such as β-sheet and α-helices, can be adapted for creating *de novo* peptides. Being considered as inherently biocompatible and biodegradable, they are predestinated for biomedical use.[19,146] For instance, drug delivery carriers are usually complex systems requiring diverse functionalities to achieve high efficacy. Their formation often involves complicated procedures with multiple components and post-assembly modifications. Using the outstanding properties of designable peptide sequences it is possible to unify all desired functions within one multifunctional peptide sequence, thereby obviating complex formulation work. In addition, the self-assembly process become very defined by using only one type of amphiphile enabling production of uniform constructs necessary to provide distinct properties and/or effects.

1.4 MRI Contrast Agents

Magnetic resonance imaging (MRI) is a widely used diagnostic tool in modern medicine to visualize structures of the body. MRI is a noninvasive method with no radiation harm, in contrast to computer tomography (CT), providing excellent spatial resolution in a sub-millimeter range. It is based on the nuclear magnetic resonance (NMR) of water protons in different body environments. To increase the contrast chemical contrast agents (CAs) are extensively used in clinical imaging. Most common CAs are based on paramagnetic transition metals, predominantly gadolinium (Gd), and superparamagnetic iron oxide nanoparticles (SPIONs). Using paramagnetic transition metal-based CAs the MRI signal intensity is increased by decreasing the longitudinal relaxation time (T_1) of water protons in close proximity to the CA. Gadolinium is a trivalent lanthanide and reveals high complexing abilities to biomolecules in the body, which results in high toxicity of aqueous gadolinium. To avoid toxic effects, gadolinium is sequestered by acyclic and macrocyclic polyaminocarboxylic acids, such as diethylenetriaminepentaacetic acid (DTPA) and 1,4,7,10-tetraazacyclododecane-1,4,7,10-tetraacetic acid (DOTA).[150] To date, eleven MRI CAs have been approved by the FDA, typically having r_1 relaxivities of around 4–5 $mM^{-1}s^{-1}$ at 1.5 T.[151] Nine are gadolinium-based (Figure 8), only two were built from other metals; one from iron nanoparticles, one from manganese complexes. However, neither of these nongadolinium contrast agents are commercially available anymore.[152] Typically administered doses for standard clinical applications are 0.1–0.3 mmol kg^{-1}, requiring injection of several grams of CA.[152] To lower the necessary dose and monitor physiologic conditions at target pathological sites in the body, functional high-relaxivity CAs are essential. To increase the relaxivity of contrast agents, numerous parameters and influence factors have to be considered, effectively described by the Solomon-Bloembergen-Morgan theory.[153-157]

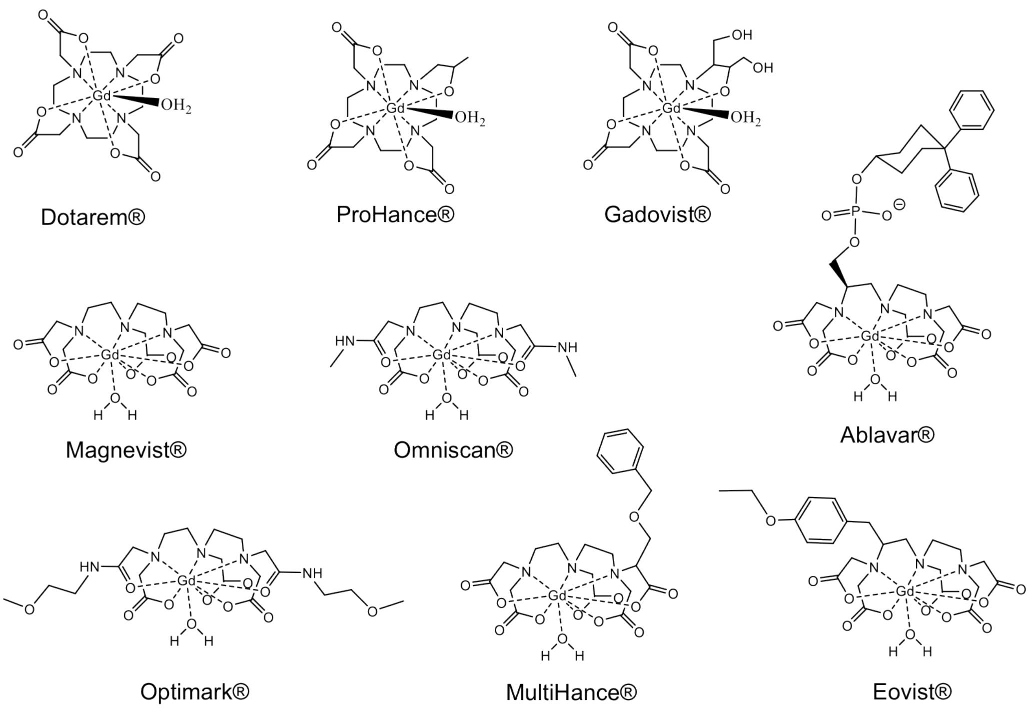

Figure 8. FDA-approved commercial MR contrast agents based on macrocyclic and linear polyaminocarboxylate-gadolinium complexes.[150]

1.4.1 Solomon-Bloembergen-Morgan Theory

The quality of a contrast agent is determined by its relaxivity. It describes the ability to increase relaxation rates of water at given concentrations of paramagnetic metal ions, mostly Gd. The contributions of diamagnetic and paramagnetic relaxation rates to the observed relaxation of water protons are additive and given by Equation 1.[158]

$$\left(\frac{1}{T_i}\right)_{obs} = \left(\frac{1}{T_i}\right)_d + \left(\frac{1}{T_i}\right)_p \tag{1}$$

$(1/T_i)_{\mathrm{obs}}$ is the observed water relaxation rate; subscript d stands for diamagnetic and subscript p stands for paramagnetic. The paramagnetic contribution to the relaxation rate is linearly dependent on the concentration of the paramagnetic species. The relaxivity (r_i, i=1,2) is defined as the slope of $(1/T_i)$ versus Gd-concentration (Equation 2).[158]

$$\left(\frac{1}{T_i}\right)_{obs} = \left(\frac{1}{T_i}\right)_d + r_i[Gd] \tag{2}$$

Two components contribute to the paramagnetic relaxation enhancement: the inner-sphere relaxation of the water directly coordinated to Gd(III) and the outer-sphere water in the second coordination sphere including the bulk water. If the water exchange rate at the metal center is fast, or the mean residence time (τ_M) is low ($\tau_M \ll T_{1m}$), the contrast enhancement comes from the increase of the relaxation rate ($1/T_{1m}$) of the coordinated water molecules.[158]

$$\left(\frac{1}{T_i}\right) = qP_m \frac{1}{T_{1m}+\tau_M} \tag{3}$$

P_m is the water bound to the metal center (mole fraction), q is the number of bound water molecules per metal ion and τ_M is the mean water residence time at the inner-coordination sphere (τ_M is the reciprocal of the water exchange rate, k_{ex}). The relaxation rate is therefore directly related to the number of bound water molecules. T_1 for the dipol-dipol (DD) relaxation mechanism is described by the paramagnetic relaxation theory by Solomon-Bloembergen-Morgan (Equation 4).[151]

$$\frac{1}{T_1^{DD}} = \frac{2}{15}\frac{\gamma^2 g^2 S(S+1)\mu_B^2}{r_{Gd-H}^6}\left[\frac{3\tau_{c1}}{1+\omega_I^2\tau_{c1}^2}+\frac{7\tau_{c2}}{1+\omega_S^2\tau_{c2}^2}\right] \tag{4}$$

γ is the nuclear gyromagnetic ratio, g stands for the electronic g-factor, μ_B is the Bohr magneton, r_{Gd-H} is the electron spin water nuclear spin distance, ω_I is the nuclear precession frequency, ω_S is the electron precession frequency and τ_{ci} are dipole-dipole relaxation correlation times. For optimizing relaxivities of CAs τ_{ci} become important. It can be influenced by modulating the rotational correlation time (τ_R) and τ_M.[158]

$$\frac{1}{\tau_{ci}} = \frac{1}{\tau_R}+\frac{1}{T_{ie}}+\frac{1}{\tau_M} \tag{5}$$

The theory demonstrates the interplay of numerous of factors to be considered when designing new or optimizing current contrast agents. Extracting the most influencing parameter, which can be optimized for engineering high relaxivity CAs, we obtain three factors: the molecular tumbling (τ_R), the hydration number (q) of the metal ion, and the solvent exchange rate (τ_M). Figure 9 shows a schematic view of the parameter in the case of Magnevist.

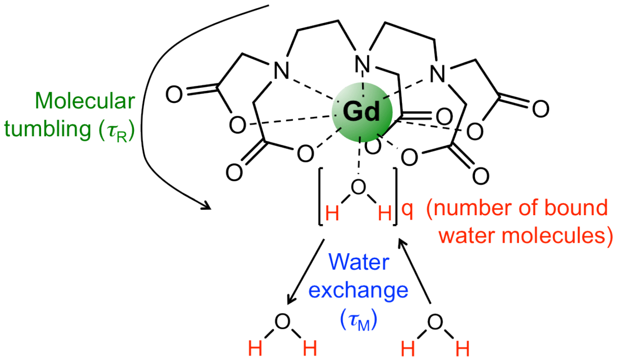

Figure 9. Key factors that influence the relaxivity of a contrast agent. To obtain a higher relaxivity the water exchange rates have to be increased and the molecular tumbling decreased compared to commercial contrast agents.[151]

Molecular tumbling, which is in the picosecond range for commercial CAs,[151] is decreased by increased molecular weights of the complexes. Therefore, retarding the rotational motion of complexes increses τ_c. This can be achieved by coupling complexes to macromolecules such as polymers or proteins. Lauffer et al. pioneered this approach by conjugating DTPA-Gd and ethylenediaminetetraacetic acid-Gd (EDTA-Gd) complexes to bovine serum albumin (BSA) and bovine immunoglobulin G (IgG) yielding a significant higher relaxivity.[159,160] Coupling Gd-complexes to linear or dendritic polymers revealed the same tendencies as found for protein conjugates.[161-163] Interestingly, the rigidity and nature of polymers had a significant effect on r_1. Linking complexes to more rigid polymers resulted in substantially higher contrast enhancement compared to more flexible constructs of the same molecular weight. DTPA-Gd, for instance, conjugated to poly(propylene imine) (PPI) dendrimers was found to reveal increasing relaxivities with increasing generations of the dendrimer due to growing rigidity and reached an r_1 of 19.7 $mM^{-1}s^{-1}$ in the fifth generation, compared to 4.7 $mM^{-1}s^{-1}$ for DTPA-Gd.[164] In contrast, flexible polyethylene glycol (PEG) had almost no retardation effect on the rotational motion, thereby r_1. On the other hand, conjugation to macromolecules may interfere with the water exchange at the metal ion and thus, lead to lower relaxivity. Studies have shown that introducing PEG to a Gd-chelates with a hydration number of two ($q = 2$) led to a decrease of q to one compensating the decreased tumbling yielding r_1-values comparable to the nonconjugated analog.[165] Throughout the years of extensive research in this field a large variety of Gd-chelates evolved ranging from linear and cyclic polyaminocarboxyl derivates to bifunctional chelates bearing functional groups such as anhydride, isobutyl chloroformate, isothiocyanate, or amine.[166]

1.4.2 Responsive Contrast Agents

The main influence factors, which are tuned and optimized to increase contrast can be exploited to develop functional CAs responsive to abnormal conditions in the body such as; metals, pH, redox state, temperature, light, or enzyme activity. The signal enhancement of responsive contrast agents (sometimes also called “smart” or “activatable” contrast agents) depends not only on the relaxivity but also on the concentration, which allows for two approaches: targeting the region of interest and responsive relaxation enhancement at conditions of the region of interest. Reduction-responsive contrast agents were constructed based on different oxidation states of a free radical or metal ion of the CA. Paramagnetic nitroxide radicals were shown to lose their relaxation properties when reduced to the hydroxylamine analog.[167] Another example comprises manganese (Mn) chelates, which revealed increased relaxivity in their reduced state (Mn(II)) compared to the oxidized chelates (Mn(III)).[168] Redox states can also lead to changes in water coordination and accessibility of the metal center. For instance, a hypoxia-sensitive CA was developed bearing nitrobenzene, reducible to an aminobenzene, which leads to protonation of a gadolinium-coordinating secondary amine in the chelate. Thus, the amine is no longer coordinated to the metal center, which increased the hydration number, thereby r_1.[169] A further example describes the change in rotational motion upon oxidation demonstrated for thiol-containing Gd-chelates forming disulfide coupling with cysteines of albumin.[170] For the detection of acidic compartments, in order to recognize cancer or inflammations, or to visualize drug delivery, pH-sensitive CAs are of high importance. A convenient way to develop pH-responsive contrast agents is the dissolvation or degradation of assembled materials when acidified. For instance, pH-sensitive liposomes loaded with Gd-chelates released its payload when acidified, decreasing the relaxation time (T_1), thus increasing r_1.[171] *In vivo* diagnosis of acidic tumors were performed using imidazole-containing micelles with incorporated Gd-chelates, which disassemble and increase r_1 upon acidification.[172] Although, many responsive CA systems have been developed to date most of them do not show high relaxivity ($>30\,mM^{-1}s^{-1}$) thus lack properties to significantly increase contrast and decrease limit of detection for diagnostic purposes.

1.5 Peptide Synthesis

Peptide synthesis describes the chemical synthesis of peptides by serially coupling desired amino acids to obtain a defined peptide sequence. For research and development purposes the synthesis is in almost all cases performed on solid state. Only when synthesizing on large-scale liquid phase synthesis is used.

1.5.1 Solid Phase Peptide Synthesis

Solid phase peptide synthesis (SPPS) allows the construction of defined peptide sequences by successive coupling of amino acids to a peptide chain covalently attached to insoluble resin beads. The method was first introduced by Merrifield in 1963, using crosslinked polystyrene as the insoluble carrier and a *t*-butoxy-carbonyl/benzyl (tBoc/Bzl)-strategy.[173] The first amino acid was attached to the resin by an acid-labile linker having the α-amino position (Nα) protected by tBoc and the side chains protected by a more acid stable Bzl protecting group. To couple further amino acids the N-terminal amine was deprotected using trifluoroacetic acid (TFA). After several neutralization and washing steps, the second amino acid was coupled by the formation of an amide bond in the presence of an activator. Repetition of this procedure (deprotection and coupling) led to the growth of the desired peptide on the resin. After coupling the last amino acid the final peptide was obtained by simultaneous deprotection of the side chains and cleavage from the resin by treatment with hydrogen fluoride (HF), which is highly toxic, thus needs special equipment and handling.

In 1970, Carpino and Han introduced 9-fluorenylmethyloxycarbonyl (Fmoc) as a base labile Nα-protecting group (Scheme 1). Eight years later the Fmoc/tBu strategy was proposed by Meienhofer, using acid labile tButyl or tBoc for the protection of amino acid side chains and Fmoc to protect the Nα-position.[174] This new strategy offered a mild alternative to the tBoc/Bzl-strategy by eliminating the need of HF for cleavage and evolved to the most used solid phase peptide synthesis strategy over the years. Before presenting solid supports, linkers, and coupling reagents (activators), the general process of solid phase peptide synthesis is briefly described:

The first step is the swelling of the linker-functionalized solid support in an appropriate solvent to offer the best possible accessibility of the functional groups to the first reagent. Then, the first amino acid is coupled to the linker in the presence of an activator followed by several washing and filtration steps to remove all non-reacted amino acids from solution before further couplings (Scheme 2A). The remaining free amines on the resin are then reacted with acetic acid anhydride (capping) to avoid reaction with any further amino acids in the following steps. The Fmoc in Nα-position is deprotected by addition of piperidine, followed by washing and filtration steps as for the first coupling (Scheme 2B). The peptide is elongated repeating the described steps until the desired peptide sequence is obtained (Scheme 2C,D). For the cleavage and simultaneous deprotection of the side chains, a mixture of mainly TFA with water and scavengers ("cleavage-cocktail") is used (Scheme 2E). The final peptide is then separated from the resin by filtration and precipitated in diisopropyl ether.

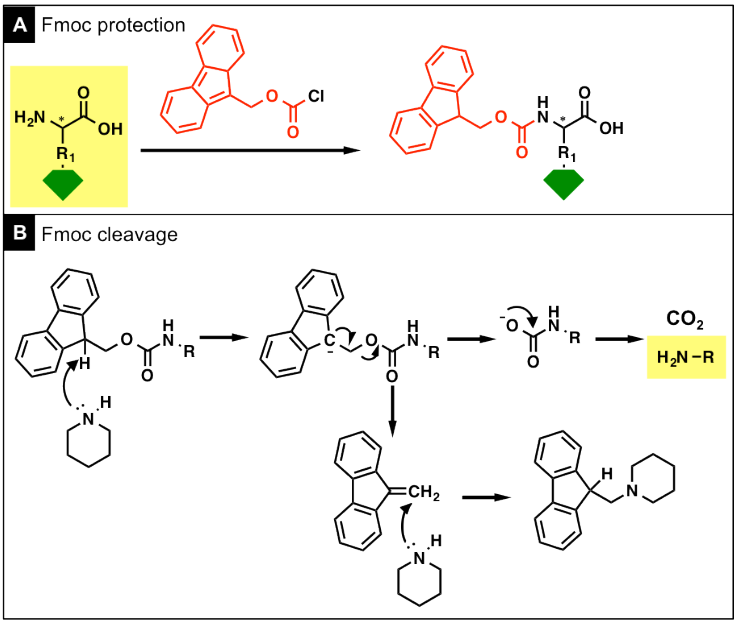

Scheme 1. Fmoc protection (red) of an amino acid using fluorenylmethyloxycarbonyl chloride (Fmoc-Cl) (A). Deprotection occurs via nucleophilic attack with piperidine to obtain the free amine of the amino acid (B).

1.5.1.1 Solid Supports and Linkers (Fmoc Strategy)

The requirements for the solid support (resin) are: stability to all solvents used during the synthesis, deprotection, and cleavage; mechanical stability towards the filtration steps; low crosslinking to allow good accessibility; and good swelling properties. Furthermore, the resin should be equipped with functional groups enabling chemical coupling to linkers. To date, three types of resins are mainly used being polystyrene (PS), polyethylene glycol (PEG) functionalized PS, and PEG-based resins. Swelling and loading performances of commonly used resins are summarized in a recent publication of Sheldon et al.[175] The linker provides reversible binding sites for coupling of the first amino acid to the solid support. Linkers are designed to be resistant to the coupling and deprotection of amino acids during synthesis but cleavable under well-defined conditions. Moreover, depending on the chemical structure and the cleavage mechanism of the linker peptides can be obtained with a variety of C-terminal functionalities. Most common C-termini are amides and acids, as these are natural peptide end groups. But also, aldehydes, alcohols, hydrazides, thioesters and other functionalities are accessible through different linker designs. For Fmoc-SPPS, 4-alkoxybenzyl alcohol-type linker (Wang-linker) and chlorotrityl chloride linker (Barlos-linker/resin) are frequently used for synthesizing peptide acids. To obtain peptide amides, the benzhydryl-type linker (Rink amide linker) is predominantly used.[175]

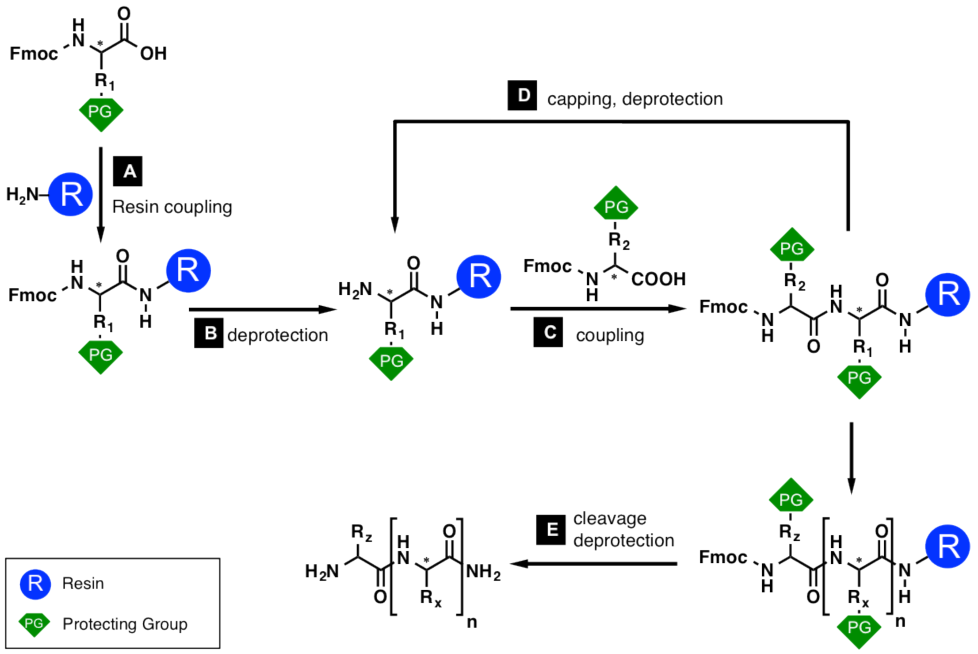

Scheme 2. General procedure for solid phase peptide synthesis using the Fmoc-strategy. First amino acid is coupled to the resin via an acid cleavable linker (A), Fmoc deprotection by piperidine (B), amino acid coupling supported by activators (C), capping of non-reacted amines by acetic acid anhydride (Ac_2O) and deprotection of Nα by piperidine (D), and cleavage and deprotection with a TFA-based cleavage cocktail containing scavengers (E) (the composition is dependent on amino acids present in the particular sequence).

1.5.1.2 Coupling Reagents (Activators)

Activation of the C-terminal acid is required to form peptide bonds between individual amino acids. This was originally achieved by using *N,N'*-dicyclohexylcarbodiimide (DCC) or *N,N'*-diisopropylcarbodiimide (DIC). Due to the tendency of these activators to racemize the amino acids new, racemization suppressant activators were developed such as 1-hydroxybenzotriazole (HOBt), 1-hydroxy-7-azabenzotriazole (HOAt), 2-(1H-benzotriazol-1-yl)-1,1,3,3-tetramethyluronium hexafluorophosphate (HBTU), *O*-(7-azabenzotriazol-1-yl)-*N,N,N',N'*-tetramethyluronium hexafluorphosphate (HATU), benzotriazol-1-yl-oxytripyrrolidino-phosphonium hexafluorophosphate (PyBOP), and 2-(6-chlor-1H-benzotriazol-1-yl)-1,1,3,3-tetramethylaminium hexafluorophosphate (HCTU) (Figure 10).[176]

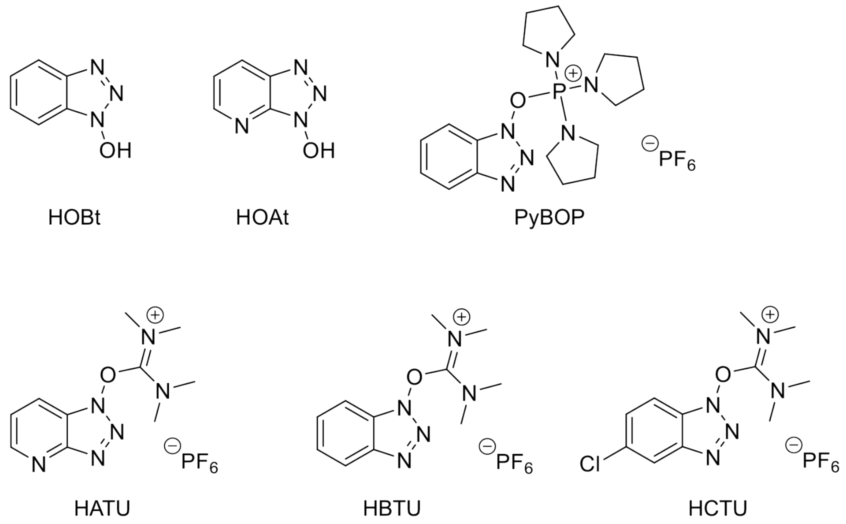

Figure 10. Different activators used in SPPS to form peptide bonds suppressing racemization of amino acids as observed for initially used DCC and DIC.

1.6 Aim of the Thesis

The overarching goal of the present thesis is the *de novo* design and synthesis of responsive and functional amphiphilic peptides as molecular building blocks to self-assemble into smart nanoparticles for biomedical applications. These encompass two functional classes: diagnostic nanoparticles and therapeutic nanoparticles.

In the past decades numerous drug- and gene-delivery carriers have been developed to increase therapeutic efficacy, decrease drug doses, and minimize side effects. While drug delivery carriers for small molecule drugs became well established, noncytotoxic gene delivery remains a major challenge. Additionally, emerging beneficial synergistic effects, combining therapeutic drugs and/or genes created a tremendous demand for sophisticated and responsive codelivery systems. Similarly, current diagnostic nanoparticles still lack high sensitivity and specificity. There is, for instance, a great need for highly sensitive and responsive MRI contrast agents for early diagnosis of diseases.

For these reasons, the scope of this thesis addressed the elaboration of functional self-assembled peptide nanoparticles for diagnostic and therapeutic applications. A first strategy for the development of diagnostic tools encompassed the incorporation of gold nanoparticles within self-assembled peptide nanoparticles. These offer the additional feature of being responsive to external trigger due to their thermoplasmonic properties. A second strategy aimed for the development of highly active MRI contrast agents, built from novel gadolinium complexes, in conjunction with responsive peptides to provide targeted contrast enhancement in tumor tissue for early diagnosis of cancer. Another scope of the present dissertation was the creation of a purely peptidic, stimuli-responsive small molecule drug/antisense oligonucleotide codelivery system readily taken up by cells to achieve high therapeutic efficacy. A further goal comprised the construction of a peptidic gene transfection carrier for the delivery of plasmid DNA.

For tailoring amphiphilic peptides lysines, histidines, and cysteines are of particular interest due to their specific chemical and physicochemical properties. They enable distinct interactions not only to payloads but also to physiologically relevant environments. Accumulation of various individual characteristics into one single peptide sequence while minimizing complexity of the assembly process to achieve smart nanomaterials, which fulfill application-oriented requirements, is very desirable.

Physicochemical characterization and biologic evaluation of the created nanoparticles provided essential information about their applicability and compatibility as well as about their self-assembling behavior. This allowed for tuning the peptides to assemble into smart, responsive, biocompatible, and biodegradable nanomaterials suitable for these applications. Straightforward rational design incorporating specific function to the sequences by point mutations served as a promising strategy to achieve these goals.

Chapter 2

2 Self-Assembled Peptide Nanoparticles Used as a Template For Ordered Gold Nanoparticle Superstructures

In this chapter, the formation of ordered peptide–gold nanoparticle superstructures via a two-step procedure is described. The particles are thoroughly analyzed and the underlying structure is discussed based on studies on planar coatings. Moreover, the composite nanoparticles are tested on the effect of NIR-illumination.

Reproduced in part with permission from Colloids and Surfaces B, Biointerfaces:
de Bruyn Ouboter, D.; Schuster, T. B.; Sigg, S. J.; Meier, W. P. Self-assembled peptide beads used as a template for ordered gold nanoparticle superstructures. *Colloids Surf., B* **2013**, 112, 542-547. © 2013, with permission from Elsevier.

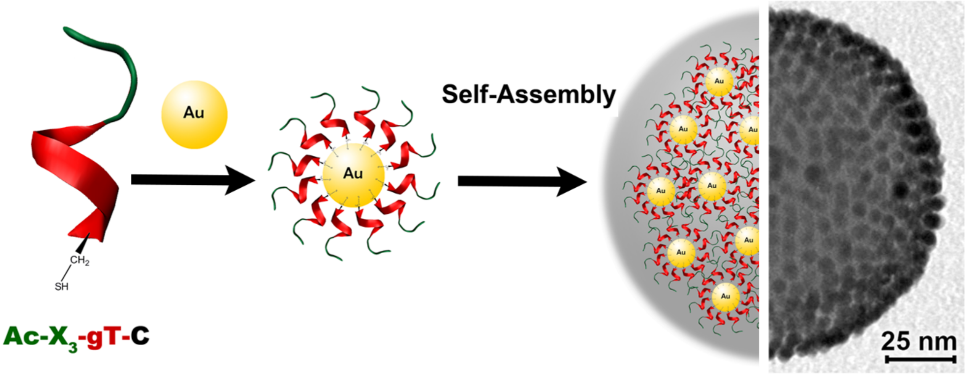

Scheme 3. Self-assembled beads from the amphiphilic peptide AcX3gTC are able to embed gold nanoparticles within their structure and thus act as a 3D template.

2.1 Abstract

Using peptide-based materials to tailor self-assembled, nanoscaled hybrid materials with potentially high biocompatibility/biodegradability is gaining importance in developing a broad range of new applications, in areas such as diagnostics and medicine. Here, we investigated how the self-assembly capacity of self-assembling, purely peptidic amphiphiles can be used to create organized inorganic materials, i.e. gold nanoparticles. A nanoparticle-forming, amphiphilic peptide *Ac*-[K*(Ac)*]$_3$-[W-DL]$_3$-W-*NH*$_2$, containing acetylated (Ac) L-lysine (K), L-tryptophan (W), and D-leucine (DL), was C-terminally modified with a cysteine (C) and linked to gold nanoparticles. Subsequent peptide-driven self-assembly of the peptide-coated gold nanoparticles with increasing water content led to controlled aggregation of the gold-core micelles, forming composite peptide–gold superstructures. The individual gold nanoparticles did not agglomerate but were separated from each other by a peptide film within the composite material, as revealed by electron microscopy studies. Structural investigation on 2D template-stripped gold demonstrated the ability of the peptides to form self-assembled monolayers. Structural elements of β-turns and weak hydrogen bonding of the hydrophobic moiety of the peptide were evident, thereby suggesting that the secondary structure remains intact.

2.2 Introduction

Exploiting the beneficial properties of two distinct nanomaterials in one hybrid can lead to advanced functional materials, thereby opening the door to a broad range of new applications in diagnostics and medicine. Materials based on colloidal, inorganic nanoparticles that exhibit exceptional properties[177,178] have led to the development of magnetic nanoparticles,[179] biosensors,[180] tools for bioimaging,[181,182] and MRI contrast agents,[183,184] thereby improving the areas of medical imaging and diagnostics. The use of peptides to design tailor-made, tunable, responsive, and nanoscaled materials[185] has also become popular and is particularly advantageous in medical applications such as biodegradable implant interfaces,[186] scaffolds for regenerative tissue growth,[187] and nanosized drug delivery vehicles.[188] Great potential derives from the benefits that accompany peptide-based materials featuring a multitude of functionalities and unique secondary structures based on controllable primary sequences and environmental conditions. In self-assembled structures, peptides can act as specific ligands or targeting moieties. In addition, peptides and proteins are built up from a library of 20 α-amino acids (AAs), which are generally considered to be biocompatible and biodegradable, although some toxic AAs are known.[189,190] Therefore, it is not surprising that peptides have been used to form fascinating hierarchical inorganic nanomaterials. There are many examples of peptides, containing a thiol group to bind gold and exhibiting a distinct affinity, such as CALNN (referring to its AA sequence), which was reported to form self-assembled monolayers (SAM) on gold nanoparticles (Au-NPs).[191] Aili et al. demonstrated a new route for nanofabrication by the association of functionalized Au-NPs via a polypeptide in a folding-dependent manner and well-defined interparticle spacing.[192] By using the peptide AG4 as a reducing agent to guide the nucleation and growth of the Au-NPs, self-assembled hybrid spheres were obtained. It was noted that, the primary sequence of the peptide, especially AA containing aromatic functional groups, altered the assembly.[193] This strong dependency on changes in the peptide conjugates towards the formation of spherical Au-NP superstructures was also observed by Song et al.[194]

Recently, it was shown that synthetic, short, purely peptidic amphiphiles can be used to produce a variety of self-assembled structures – such as micelles and fibers,[148] vesicles,[28] and peptide nanoparticles (multicompartment micelles)[29,30] – in a well-controlled manner. A truncated version of gramicidin A (gA) was used for the hydrophobic moiety of the amphiphiles (gT, Table 2). The β-helical structure of gA is unique and defines the hydrophobic character.[195]

Table 2. Codes and Sequences of Amphiphilic Peptides Used to Study the Formation of Peptide–Gold Nanoparticles Superstructures.

code	sequence
Gramicidin A	HCO-V-G-A-DL-A-DV-V-DV-[W-DL]$_3$-W-$NHCH_2CH_2OH$
-gT	-[W-DL]$_3$-W-NH_2
AcX3gT	Ac[K(Ac)]$_3$-[W-DL]$_3$-W-NH_2
AcCX3gT	Ac-C-[K(Ac)]$_3$-[W-DL]$_3$-W-NH_2
AcX3gTC	Ac[K(Ac)]$_3$-[W-DL]$_3$-W-C-NH_2

The hydrophilic, peptidic backbone is hidden within the helix, as the hydrophobic tryptophan (W) and leucine (DL) side chains shield it. Thus, this structure as a purely peptidic hydrophobic sequence allows the construction of an amphiphile. The hydrophilic sequence consists of oligolysine, either acetylated (X) or native (K). The uncharged peptides AcX3gT as well as AcX3gTC (with a C-terminal cysteine, Table 2) form spherical nanoparticles in aqueous solution. Their size can be controlled within a diameter range of 260–800 nm by means of the initial peptide concentrations prior to the self-assembly process.[30] Therefore, the secondary structure of the amphiphilic molecule is essential. It was shown that if the three D-leucines are replaced by L-leucines, peptide nanoparticles will not be formed.[31] A hierarchical organization of micelle-like structures within the peptide nanoparticles was found and the structures assigned to multicompartment micelles (MCM).[30]

In this study, we focused on structural elements; that is, how the self-assembly ability of short and purely peptidic amphiphiles can be used in interaction with gold nanoparticles (Au-NPs) to obtain hierarchically organized composite peptide–gold NPs, i.e. the peptide would act as a template for the ordered assembly of Au-NPs to create a new composite material.

2.3 Results and Discussion

2.3.1 Peptide Nanoparticles – Templates for 3D Incorporation of Gold Nanoparticles (Au-NPs)

The objective was to use the peptide nanoparticles assembly as a template for the organization of Au-NPs therein. As illustrated in Scheme 4, AcX3gT self-assembles in peptide nanoparticles with a multicompartment micelles (MCM) structure.[29,31] Therefore, we included a thiol functional group (cysteine) at the hydrophobic C-terminal end of the peptide for a possible connection of the peptide to the Au-NPs (AcX3gTC, Table 2). Ethanolic peptide solution was pretreated with DTT to avoid disulfide formation of the peptide before being mixed together with Au-NPs (8.1 ± 1.0 nm) for 6 h. Therefore, an excess of peptide ($10^2\times$) was provided to enable a maximum coverage of Au-NPs. Afterwards the Au-NPs were separated from free, unbound peptide in the solution by dialysis in 50% ethanol (no self-assembly[30]) and subsequently dialyzed against water, which induced the self-assembly process revealing composite peptide–gold nanoparticles. The resulting solution was typically a turbid, reddish solution with observable sedimentation.

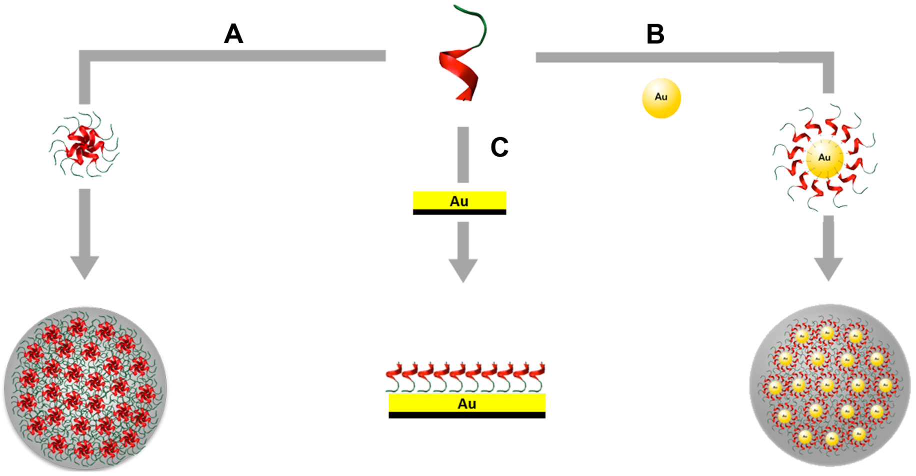

Scheme 4. Illustration of formation processes: micelle and peptide nanoparticle formation (A), coating of gold nanoparticles with the peptide AcX3gTC and subsequent formation of composite peptide–gold nanoparticles enabled by the self-assembly features of the peptide (B), and formation of a peptide SAM on template-stripped gold using AcCX3gT (C).

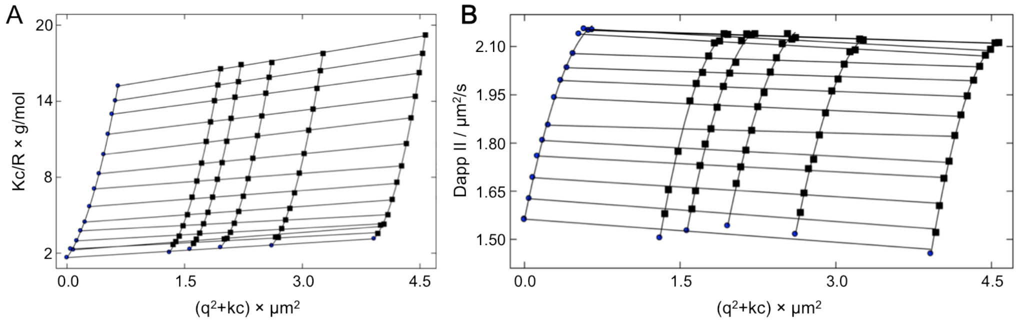

Figure 11. SLS analysis (Zimm plot) of CP-Au-NPs revealing an R_g of 124 ± 9 nm (A). DLS analysis (D-II, cumulant fit) resulting in an R_h of 154 ± 16 nm (B).

Analysis was performed by static and dynamic light scattering (SLS and DLS), transmission electron microscopy (TEM), and scanning electron microscopy (SEM). SLS provided a radius of gyration (R_g) of 124 ± 9 nm, while the hydrodynamic radius (R_h) was calculated to 154 ± 16 nm (Figure 11), thus resulting in a ratio R_g/R_h of 0.80 – close to the theoretical value of a solid sphere (0.775). The detected particles were thus far bigger than the 8.1 nm Au-NPs. As shown in Figure 12A, small particles showed homogenously distributed Au-NPs in a dense arrangement within the peptide nanoparticles. However, the formed nanoparticles also exhibit a certain size distribution and variation in Au-NP density (Figure 12C), which may require isolation of a particular species depending on the application.

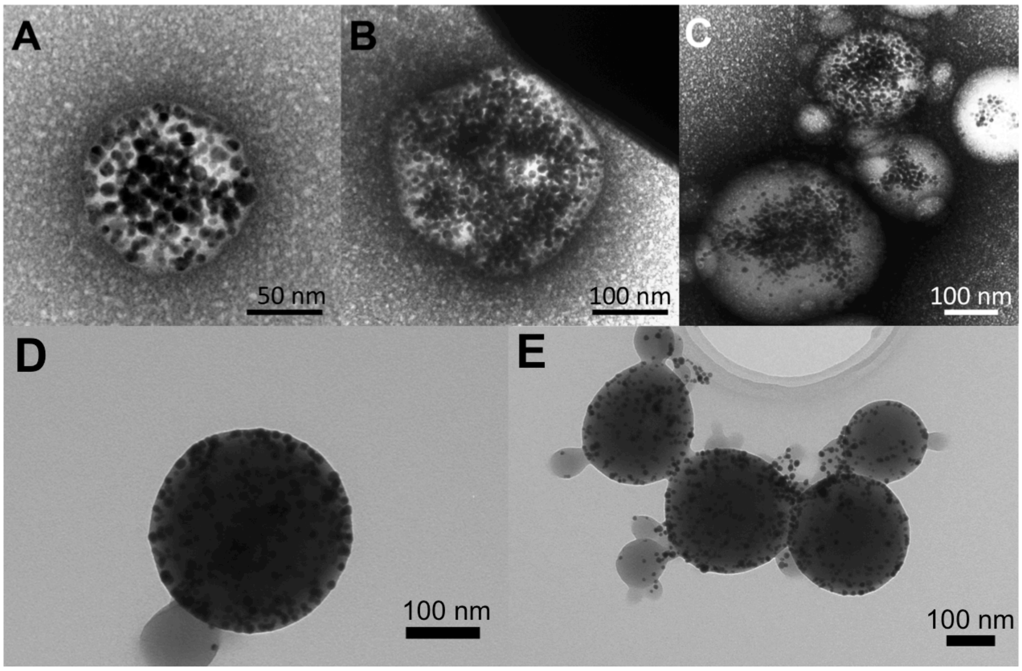

Figure 12. TEM micrographs of self-assembled CP-Au-NPs showing: dense packing of Au-NPs within particles (A, B, D) and an overview of size distribution and gold particle distribution (C, E).

It can be clearly seen that Au-NPs did not aggregate within the peptide nanoparticles but were separated by the peptide material. The thickness of the peptide layer around the Au-NPs, which was measured on its edge, was 1.3 ± 0.6 nm. Considering the length of the peptides of around 1.6 nm, this indicates peptide monolayers around the Au-NPs, i.e. Au-NPs which are separated from each other by peptide double layers, though a partial overlap cannot be excluded.[28] These expected findings are consistent with the MCM structure of the peptide nanoparticles. SEM showed similar particle sizes compared to TEM micrographs (Figure 13). These findings allow the description of a possible formation process. Via the described two-step, one-pot protocol, first, Au-NPs were coated by AcX3gTC in ethanol solutions, which was followed by the self-assembly of the obtained gold-core micelles into composite peptide-gold nanoparticles (CP-Au-NPs) during dialysis against water (Scheme 4). The self-assembly capacity of the peptidic amphiphiles acted as a template for 3D organization of Au-NPs.

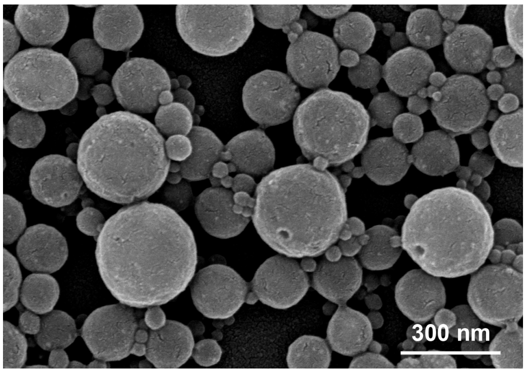

Figure 13. SEM micrograph of composite peptide gold nanoparticles revealing similar sizes and morphologies compared to TEM pictures.

2.3.2 Model Studies – AcCX3gT Peptide Films on Planar Gold Surfaces

We investigated 2D peptide films on a planar gold surface to deduce more information about peptide gold interaction and the ability of the peptides to form monolayers. As a gold surface, template-stripped gold (TSG) was used, which is known to exhibit a very smooth surface.[196] To access defined peptide monolayers we used the Langmuir-Blodgett (LB) technique. It was therefore judged to be prudent to use AcCX3gT instead of AcX3gTC, to be able to transfer the LB film – in which amphiphilic peptides are orientated with the more hydrophilic sequence (AcCX3) towards the water and the hydrophobic sequence (gT) towards the air – covalently onto TSG. The possibility to substitute AcX3gTC by AcCX3gT was further supported by their similar self-assembly properties.[29,31] An isotherm of AcCX3gT is shown in Figure 14. Peptide films were produced by the LB technique, transferred onto freshly cleaved

TSG and subsequently analyzed by atomic force microscopy (AFM). Figure 15 presents an AFM image of a transferred AcCX3gT film. The films showed a very homogenous, featureless, and smooth surface. A slightly rougher surface compared to bare TSG indicated deposition but also illustrated the excellent quality of the peptide films. The partial removal of the peptide film upon scratching with the AFM tip and subsequent scanning further indicated the successful transfer of the LB film to the solid substrate and revealed a film thickness of about 1.2 nm. Considering the length of a molecule to be 1.6 nm, this value might arise from either low surface coverage (unlikely for LB transfer at high surface pressure) or a tilt angle of approximately 40° (Figure 15, wild-type gA at the air–water interface: 30°).[197]

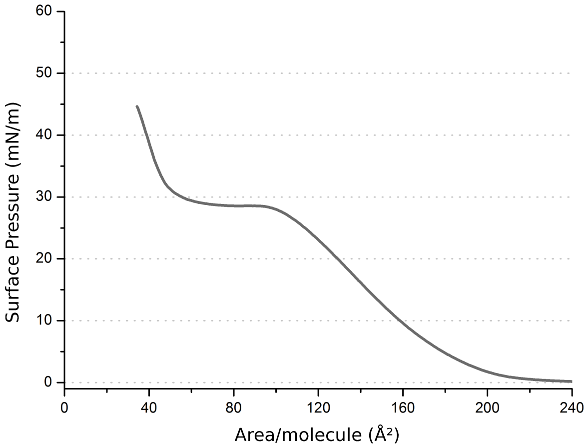

Figure 14. Isotherm of AcCX3gT peptide. The mean molecular area (MmA) of 196 ± 3 Å^2/molecule arises from extrapolation to zero surface pressure, which reflects a helix radius (r) of 7.9 Å and is consistent with literature values for the gA helices.[195,197]

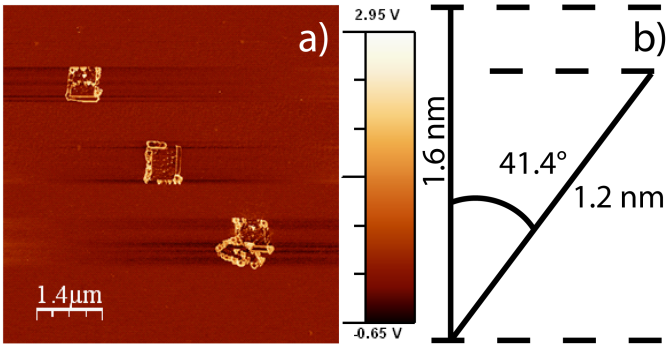

Figure 15. AFM image of a partly removed AcCX3gT film on a Si-wafer via scratching shows a thickness of 1.2 nm (a). Tilt angle based on a peptide length of 1.6 nm (b).

Additionally to LB transfer, we investigated the formation of peptidic self-assembled monolayers (SAM). In this technique, peptides are not compressed into a 2D arrangement as in the LB technique, but will have to arrange themselves onto the gold substrate without external pressure, which corresponds more to the processes of peptide adsorption onto Au-NPs from solution.

Using the thiol-functionality for the formation of a SAM is best known for alkyl chains, but also the rod-like structure of the hydrophobic gT-trunk is expected to form an ordered alignment.[198] The TSG samples were then immersed in an AcCX3gT ethanolic solution for 12 h and analyzed by AFM. The resulting thin films showed very smooth surfaces, similar to LB-films, as illustrated in the height profiles in Figure 16.

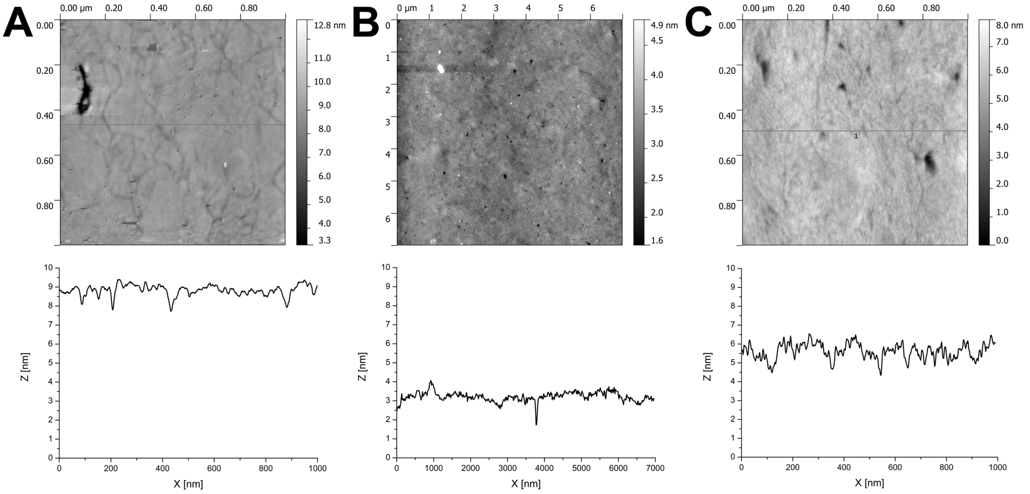

Figure 16. AFM images and corresponding height profiles of (A) template-stripped gold (TSG) (B) AcCX3gT monolayer on TSG via Langmuir-Blodgett transfer (π_{TR} = 25 mN/m) and (C) AcCX3gT monolayer on TSG via immersion.

Adsorption of AcCX3gT on gold was monitored by a quartz crystal microbalance (QCM). The mass kept increasing up to 150 ng/cm^2 while dissipation stayed constant (Figure 17) indicating a surface adsorption of dissolved peptide molecules to form a rigid, thin film (~1.5 nm), not removable by washing. The binding of the N-terminally functionalized purely peptidic amphiphiles to gold demonstrates the capacity of the peptides to bind to gold as with the well-known thiol–gold bonds.[199]

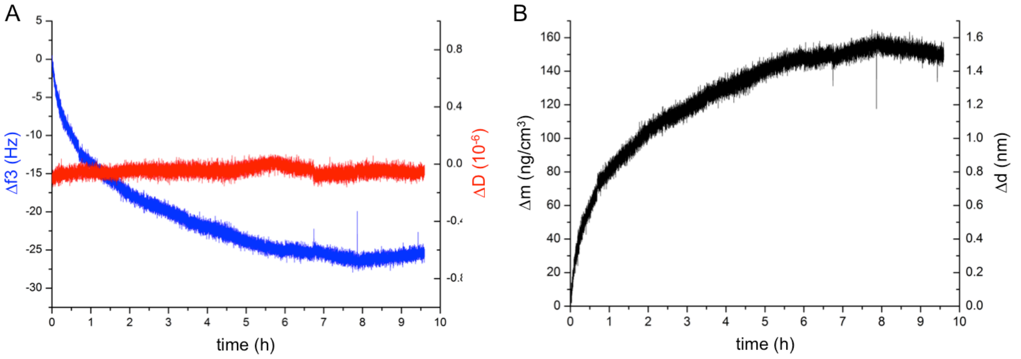

Figure 17. QCM analysis of AcCX3gT. QCM frequency shift (blue) and dissipation (red) of an ethanolic peptide solution (A). Mass adsorption via Sauerbrey, which translate into a thickness, assuming a density of the peptide layer of 1 g/cm^3 (B).

To gain further information on the obtained film, we performed IR, i.e. polarization modulation infrared reflection absorption spectroscopy (PM-IRRAS) measurements on two samples (from LB transfer and immersion techniques). First, the results prove the presence of a peptide film on the TSG (Figure 18). Second, the amide I adsorption of both samples at 1662–1675 cm^{-1} (weak signal at ~1612 cm^{-1}) differs significantly from the known spectra for gA conformations, and also from the random coil spectra (~1630–1640 cm^{-1}).[200-202] Nevertheless, the amide I adsorption was related to β-turns and weak hydrogen bonding.[200] In addition, the circular dichroism spectra, presented earlier,[31] support its helical configuration, with a maximum at 223 nm, related to the [W-DL]$_3$-W moiety, that was also found for L- and D-amino acids containing cyclic peptides.[203] Therefore, based on similarity with these peptides, we propose the secondary structure of gT to contain a β-turn stabilized by intramolecular hydrogen bonding.

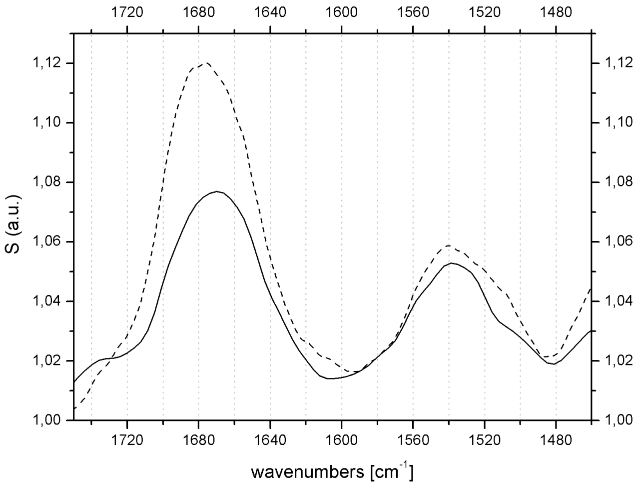

Figure 18. PM-IRRAS: Immersion in ethanolic AcCX3gT peptide solution (solid) and AcCX3gT LB-film (dashed).

However, caution must be taken when transferring results from a planar surface to the Au-NPs and *vice versa* based on the differences in curvature. Nevertheless, because the results from IR measurements for transferred LB-films are comparable with the results for self-assembled monolayers, it indicates that covalent adsorption without the deformation of the peptide secondary structure is possible.

To assess the responsiveness of the incorporated gold nanoparticles to near infrared (NIR) irradiation composite peptide–gold nanoparticles were exposed to 805 nm laser light. The particles were monitored on their size distribution using DLS at 90°. However, irradiation with 100 mW 805 nm laser light for up to 1 h did not significantly affect the sizes of the particles, thus indicating no decomposition in the tested range (Figure 19). This can be attributed to the relatively low intensity and the wavelength, which is at the border of visible light to infrared, necessary to not cause harm to the skin and for a deeper penetration to soft tissue.

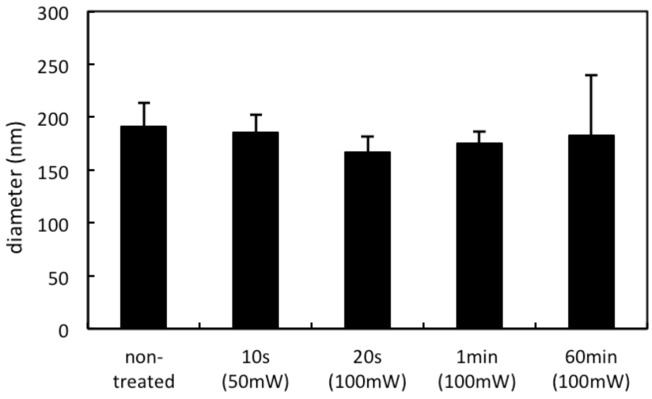

Figure 19. Hydrodynamic diameters of CP-Au-NPs irradiated with 805 nm laser light obtained from DLS measurements.

2.4 Conclusion

C- or N-terminal modification of the nanoparticle forming peptide AcX3gT with cysteine (AcX3gTC and AcCX3gT) led to similar self-assembly behavior and allowed the linkage of the peptide to gold. A homogenous, 2D peptide alignment was illustrated by transferred monolayers and, similarly, via immersion and the formation of peptide SAMs. For the secondary structure of the hydrophobic gT region, a β-turn and intramolecular hydrogen bonds were proposed, these being assigned for both films: the transferred LB and the SAM. The latter indicates the possibility that, also on the Au-NP, an intact configuration remains, which is also supported by the thickness of the peptide layer around the Au-NP within the nanoparticles.

An *in situ* reaction with Au-NPs allowed us to transfer the self-assembly properties of the peptide to new, composite material, which led to the aggregation of the gold-cored micelles forming particles of sizes similar to the original peptide nanoparticles without gold. We showed that the newly formed composite peptide–gold nanoparticles are densely packed, but the individual gold nanoparticles remain separated by a thin peptide bilayer. The newly formed CP-Au-NPs may find application as a drug delivery system using the intrinsic thermoplasmonic properties of the incorporated gold nanoparticles to trigger release of payload. Furthermore, the created CP-Au-NPs lay the basis for the development of theragnostic agents exploiting the intermicellar space to incorporate payloads while the attenuation of X-rays by the gold nanoparticles enables high contrast in computer tomography. However, further investigation and optimization of the system is required to exploit full potential.

Chapter 3

3 Stimuli-Responsive Codelivery of Oligonucleotides and Drugs by Self-Assembled Peptide Nanoparticles

This chapter aims for the rational design of responsive peptide nanoparticles for simultaneous delivery of antisense oligonucleotides and small molecule drugs. It includes the design, synthesis, and nanoparticle formation as well as the loading and controlled release of the payloads upon a reductive trigger. Furthermore, the potential of the novel nanoparticles is demonstrated by the delivery of a clinically relevant drug.

Reproduced in part with permission from Biomacromolecules:
Sigg, S. J.; Postupalenko, V.; Duskey, J. T.; Palivan, C. G.; Meier, W. Stimuli-Responsive Codelivery of Oligonucleotides and Drugs by Self-Assembled Peptide Nanoparticles. *Biomacromolecules* **2016**, 17, (3), 935-945. © 2016 American Chemical Society.

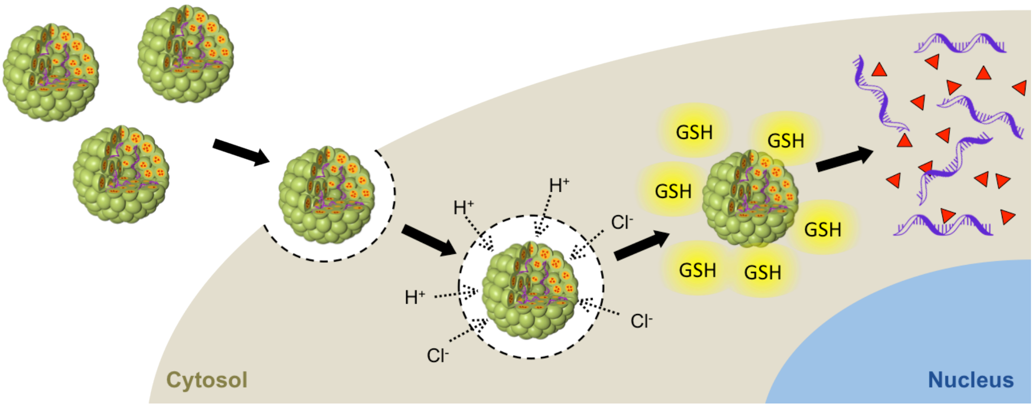

Figure 20. Coloaded reduction-responsive peptide nanoparticles internalize to cells. In contact with elevated glutathione levels in the cytosol the peptide nanoparticles disintegrate and release their payloads.

3.1 Abstract

Ever more emerging combined treatments exploiting synergistic effects of drug combinations demand smart, responsive codelivery carriers to reveal their full potential. In this study, a multifunctional stimuli-responsive amphiphilic peptide was designed and synthesized to self-assemble into nanoparticles capable of co-bearing and -releasing hydrophobic drugs and antisense oligonucleotides for combined therapies. The rational design was based on a hydrophobic L-tryptophan-D-leucine repeating unit derived from a truncated sequence of gramicidin A (gT), to entrap hydrophobic cargo, which is combined with a hydrophilic moiety of histidines to provide electrostatic affinity to nucleotides. Stimuli-responsiveness was implemented by linking the hydrophobic and hydrophilic sequence through an artificial amino acid bearing a disulfide functional group (H3SSgT). Stimuli-responsive peptides self-assembled in spherical nanoparticles in sizes (100–200 nm) generally considered as preferable for drug delivery applications. Responsive peptide nanoparticles revealed notable nucleotide condensing abilities while maintaining the ability to load hydrophobic cargo. The disulfide cleavage site introduced in the peptide sequence induced responsiveness to physiological concentrations of reducing agent, serving to release the incorporated molecules. Furthermore, the peptide nanoparticles, singly loaded or coloaded with boron-dipyrromethene (BODIPY) and/or antisense oligonucleotides, were efficiently taken up by cells. Such amphiphilic peptides that led to noncytotoxic, reduction-responsive nanoparticles capable of codelivering hydrophobic and nucleic acid payloads simultaneously provide potential toward combined treatment strategies to exploit synergistic effects.

3.2 Introduction

Combined treatments are gaining increasing impact in medicine not only to exploit synergistic effects of therapeutics, but also to overcome multidrug resistance (MDR) in cancer therapies.[204] This creates a tremendous demand for sophisticated carrier systems capable of codelivering therapeutics simultaneously for higher efficacy. For this purpose combinations of small drugs are beneficial, but drug/gene combinations are also of high interest, especially in the case of P-glycoprotein (P-gp) mediated MDR.[204] Nanotechnology provides a vast array of opportunities and promise in the rational design of multifunctional drug delivery systems. Nanocarriers can be designed for the delivery of therapeutics: protecting them from being metabolized,[63,64] enhancing bioavailability, lowering off-target effects, and decreasing the necessary drug dose by increasing accumulation at the diseased site.[205] Of particular interest for P-gp mediated MDR is the codelivery of drugs and nucleic acids in a single nanocarrier system. Promising results were obtained by antisense oligonucleotide-mediated down-regulation of the overexpressed P-gp, responsible for drug efflux, in combination with small molecule anticancer drugs.[206,207] For incorporation of payloads, two main strategies are followed, where nucleic acids or drugs are either synthetically conjugated to the carrier or noncovalently condensed or entrapped.[63,208] Covalent strategies involve the linkage of polymers, proteins, peptides, and inorganic nanoparticles to nucleic acids or drugs,[136] while noncovalent condensation is achieved via electrostatic interaction, hydrogen bonding, and hydrophobic interactions. Noncovalent nanocarriers for oligonucleotide delivery are usually able to cross cell membranes and deliver the cargo better than conjugated ones, but are in general more difficult to control.[137,208] Current strategies for codelivery of small molecule drugs and nucleic acids rely on lipids,[209,210] polymers,[211,212] and conjugates,[213,214] which form structures able to entrap small drugs as well as to noncovalently condense DNA or RNA. Further improvement of efficacy can be achieved by utilizing physiological microenvironments at pathological sites such as pH,[72-75] temperature,[76] and redox potential[77,78] as release triggers. Responsive polymeric systems and conjugates for codelivery were developed recently, bearing moieties sensitive to physiological triggers such as pH[215-218] or redox potential.[219-222]

Emerging peptide based self-assembled nanostructures in the field of nanomedicine are particularly interesting because they are considered to be inherently biocompatible and biodegradable.[19,22,146] Specific inter- and intramolecular interactions between amino acids such as electrostatic interactions, hydrogen-bonding, hydrophobic interactions, and π–π-stacking can be implemented to obtain highly ordered and defined assemblies. The bottom up rational design is based on selecting amino acids with the desired properties in order to create novel amphiphilic peptides able to self-assemble into defined architectures. Furthermore, the combination of distinct functionalities, such as responsiveness, can be implemented within one molecule enabling the development of peptides self-assembling into well-defined and multifunctional nanoparticles, which is a tremendous advantage due to simplicity and applicability for biomedical applications.[145,223,224] Reported peptidic carriers for delivering a single drug comprise polyplexes,[25,121,123] hydrogels,[225] and micelles.[122,144,145,224,226] There are only a few peptidic codelivery systems described to date capable of delivering nucleic acids and small molecule drugs simultaneously.[144,224,226] Recent reports describe peptides, consisting of a polyhistidine–polylysine hydrophilic peptide sequence coupled with a hydrophobic sequence comprising of alanine, phenylalanine, and/or leucine, which show synergistic cytotoxic effects when delivering p53 plasmid in combination with doxorubicin (Dox) or paclitaxel (PTX).[144,226] Another report describes a slow release (20–30 h) of Dox from a polyhistidine–TAT conjugate at pH 5 compared to neutral pH accompanied by synergistic effects when codelivered with p53 plasmid.[224] However, further improvement for stimuli responsiveness is essential to enhance a rapid delivery and/or release of coloaded payloads.

Here, we aim for a straightforward rational design of new peptide nanoparticles that enhance the properties of the AcX3gT nanoparticles to favor codelivery and rapid release of small molecule drugs and nucleic acids simultaneously by reduction-responsiveness. The new peptides are separated into three key structural features: the hydrophilic region (region 1), linker unit (region 2), and hydrophobic region (region 3) (Figure 21). The hydrophilic moiety was redesigned from the previous peptide AcX3gT by implementing nucleotide condensing sites, based on oligohistidine, known to promote these interactions.[227] By introducing oligohistidine the slight surface charge is in addition intended to prevent aggregation, which limited AcX3gT potential use, when loaded with hydrophobic molecules.[31] Moreover, using oligohistidine as the hydrophilic sequence preserves secondary aggregation to nanoparticles due to a pK_a of 6.0 in contrast to previously reported nonacetylated K3gT, bearing lysines with a pK_a of 10.7, which form micelles.[30]

Increasing the number of aromatic side chains is expected to support molecule incorporation as already reported for AcX3gT. The nanoparticles were also expected to be smaller, thus more suitable for biomedical applications due to higher water solubility compared to AcX3gT.[29,30] The stimuli-responsiveness to cellular redox potential was integrated to the sequence by using an artificial disulfide amino acid (region 2, Figure 21). By adding this linker in between the hydrophilic and hydrophobic sequences, we favor a higher release upon external stimuli, which was previously not available when designed only with peptide bonds. Therefore, in the structure of this new peptide, only the gramicidin-inspired seven-amino-acid repeating unit gT remained from the previously reported peptide AcX3gT in order to maintain the previously observed self-assembly into nanoparticles that are capable of entrapping hydrophobic payloads. Characterization revealed that the three functional units enabled assembly of spherical peptide nanoparticles that were reduction sensitive (H3SSgT) and capable of loading desired model drug (boron-dipyrromethene (BODIPY)) and nucleic acid (antisense oligonucleotides (AON)) payloads simultaneously.

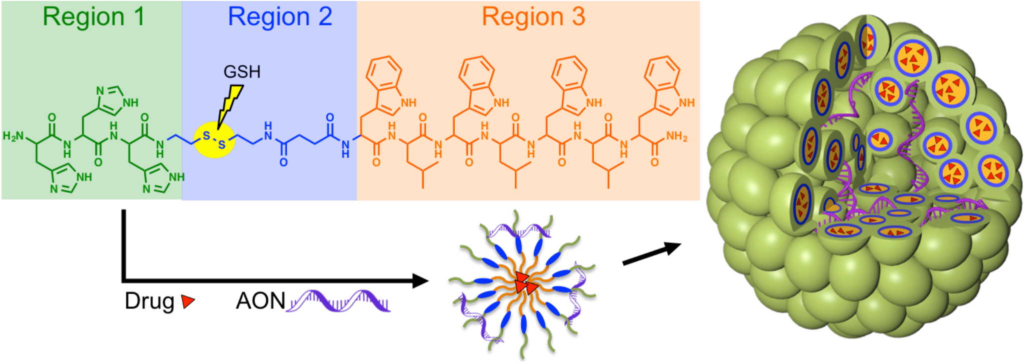

Figure 21. Schematic representation of nanoparticle assembly incorporating AON and drugs. Designed amphiphilic peptide consists of three regions: hydrophilic (region 1), reducible linker (region 2), and hydrophobic (region 3). Amphiphilic peptide assembles in a first step into micelles, incorporating drug in the hydrophobic region and nucleotides along their hydrophilic region. Further self-assembly leads towards spherical nanoparticles, potentially multicompartment micelles.[29] Adapted from Gunkel-Grabole et al.[1] Reproduced by permission of The Royal Society of Chemistry.

We selected BODIPY as the model molecule with the appropriate hydrophobicity and molecular weight, while the hydrophilic DoxHCl served only to demonstrate the ability of the peptide nanoparticles to encapsulate hydrophilic molecules as well. Fluorescence correlation spectroscopy (FCS) analysis was used to evaluate whether the reduction responsive particles were able to rapidly release all payloads in a reducing environment. A final analysis in HeLa cells was performed to show that the reduction-sensitive H3SSgT peptide nanoparticles are taken up and the cargo retains its functionality. Although stimuli-responsive codelivery architectures have been developed for polymer, lipid, and peptide-conjugate self-assemblies our strategy has the advantage of providing purely peptidic and biodegradable nanoparticles for efficient codelivery and release of oligonucleotides and drugs simultaneously upon reduction.

3.3 Results and Discussion

3.3.1 Design, Synthesis, and Characterization of Peptides and Their Self-Assemblies

Two new amphiphilic peptides, H3gT and H3SSgT, were designed from the previously reported peptide, AcX3gT (Figure 22A). The first, H3gT, was designed with the cationic histidine amino acids in place of the acetylated lysines in order to improve the encapsulation of charged species such as AON into the self-assembled nanoparticles (Figure 22B). In order to improve the release of cargo molecules from H3gT nanoparticles, a second peptide H3SSgT was designed by incorporating an artificial disulfide amino acid to serve as a reduction cleavable linker (Figure 22C).

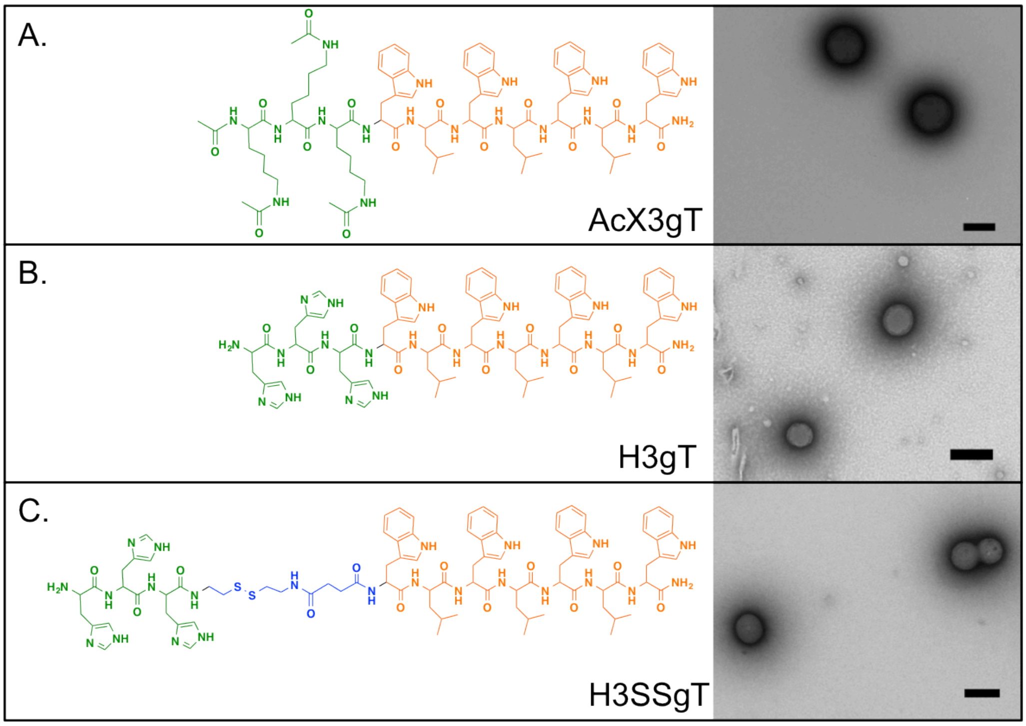

Figure 22. Synthesized peptide sequences of AcX3gT (A),[31] H3gT (B), and H3SSgT (C). The hydrophobic gT sequence is orange, the hydrophilic sequence is green, and the reducible S–S linker is blue. TEM micrographs represent self-assembled structures of each peptide. Scale bar: 200 nm.

Inserting the linker between the hydrophilic oligohistidine and hydrophobic gT will lead to separation of the charged interactions of the oligohistidine and the hydrophobic interaction by the gT, leading to dissolution of the nanoparticle and release of the encapsulated molecules. The amphiphilic peptides AcX3gT, H3gT, and H3SSgT were synthesized using conventional solid phase peptide synthesis (SPPS) and purified by high-performance liquid chromatography (HPLC). The peptide masses of AcX3gT, H3gT, and H3SSgT were measured by liquid chromatography electron spray ionization mass spectrometry (LC-ESI-MS) to match the expected values of 1653.9 g/mol, 1512.8 g/mol, and 1746.8 g/mol, respectively (Figure 23A–C).

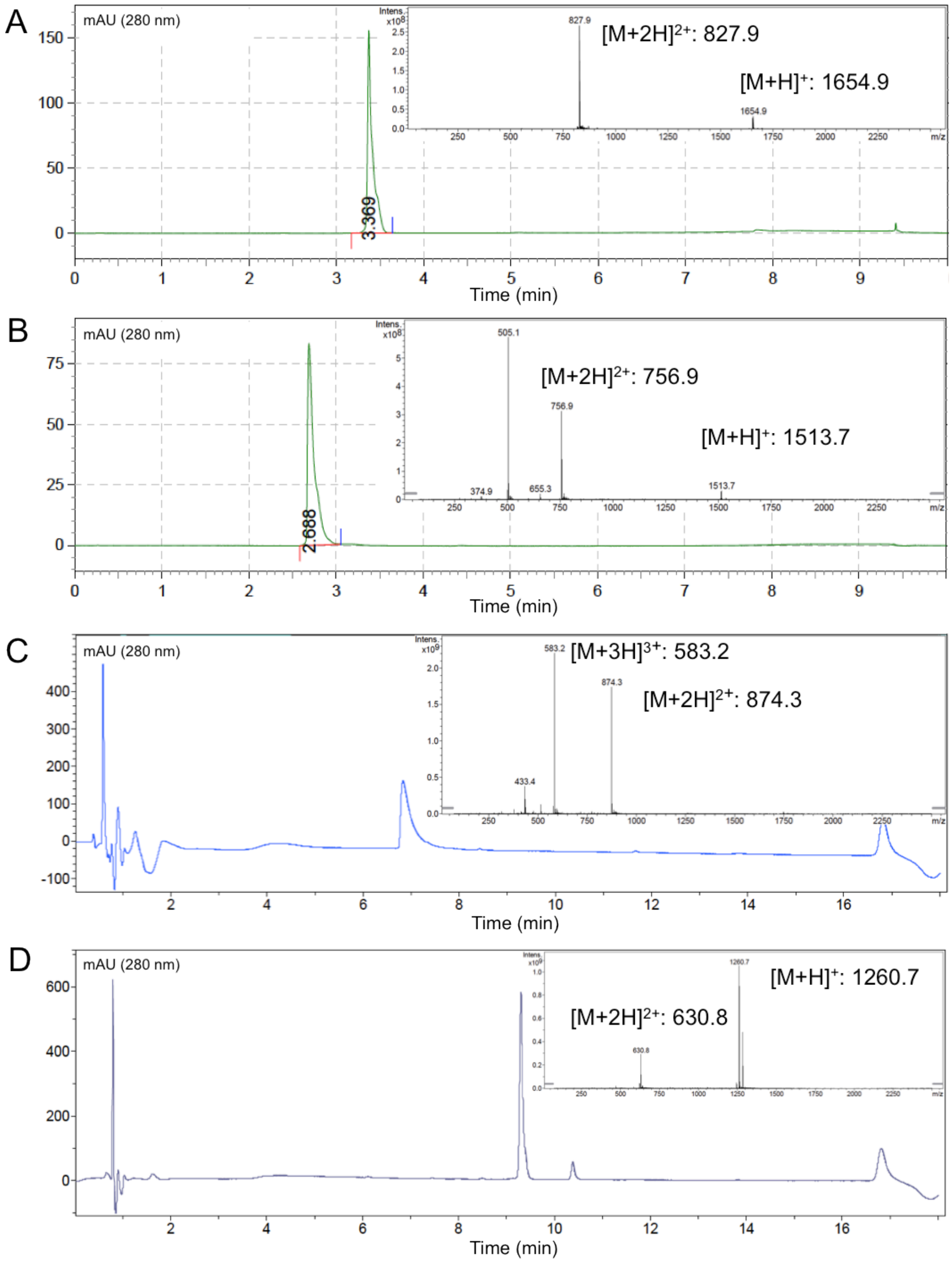

Figure 23. HPLC chromatogram (detection of tryptophan at 280 nm) and LC-ESI-MS data of purified AcX3gT (A), H3gT (B), and H3SSgT before (C) and after (D) treatment with DTT.

Similar to AcX3gT, both H3gT and H3SSgT self-assembled in water leading to spherical nanoparticles. The change in the sequence from acetylated lysines of AcX3gT to oligohistidine of H3gT or H3SSgT did not affect the assembly properties of the amphiphilic peptides, revealing spherical shapes and a smooth surface by transmission electron microscopy (TEM) (Figure 22). However, the initial concentration of each peptide led to differences in nanoparticle size. There is a linear relation between initial concentration and nanoparticle size for AcX3gT, with a lower plateau at 260 nm for concentrations below 0.5 mg/mL.[30] In contrast, H3gT and H3SSgT exhibited sizes of about 150 nm and 100 nm, respectively, for nanoparticles assembled from peptide concentrations of 0.2 mg/mL. This is regarded as optimal size for drug delivery systems to have sufficient loading but still avoid excessive clearance by macrophages.[67,68] Replacing the acetylated lysines of AcX3gT with histidines of H3gT did not alter the ability to form spherical nanoparticles in contrast to nonacetylated analogs of AcX3gT (K3gT).[30] This can be attributed to a closer proximity between the side chain functional groups and its aromatic nature, which enables π–π-stacking, cation–π interactions, and hydrogen–π interactions.[228]

3.3.2 Encapsulation of Payload and Characterization of Loaded Nanoparticles

The ability of the new peptides H3gT and H3SSgT to embed payloads was compared to AcX3gT using a hydrophobic small drug molecule model (BODIPY), or Atto550 labeled antisense oligonucleotides (AON). First, fluorescence correlation spectroscopy (FCS), which distinguishes fluorescent species diffusing free in solution compared to those associated with nanoparticles, was measured to ensure the new peptides maintained the ability to load hydrophobic payloads. Varying the peptide sequence to include histidines or a reduction sensitive linker did not affect the incorporation of the hydrophobic molecule BODIPY (Table 3). AcX3gT and H3SSgT showed high loading efficiencies; however, upon encapsulating BODIPY in H3gT nanoparticles, the particles quickly shifted to large aggregates, which cannot be measured by FCS. The ratio of loaded cargo was obtained by fitting the autocorrelation functions using two component fits: free dye and dye-loaded peptide nanoparticles (Table 3). Next, AONs were loaded into each peptide nanoparticle. By FCS, AcX3gT showed a correlation curve identical to that of the free AON (Figure 24A). This indicated that AcX3gT was incapable of binding AON due to a lack of charge interactions. However, both the H3gT and H3SSgT, which contain the oligohistidine sequence, were able to bind AON showing an increased diffusion time compared to free AON alone (Figure 24A, Table 3).

Table 3. FCS Characterization of Singly and Coloaded Peptide Nanoparticles.[a]

peptide nanoparticles	payload	diffusion time (μs)	hydrodynamic diameter (nm)	loading efficiency[b] (%)
Free species	BODIPY	61 ± 2.8	N/A	N/A
	AON	102 ± 7.3	N/A	N/A
AcX3gT	BODIPY	7700 ± 439	174 ± 10	82 ± 7
	AON	N/A	N/A	N/A
H3gT	BODIPY	N/A	N/A	N/A
	AON	8430 ± 2400	235 ± 67	89 ± 3
H3SSgT	BODIPY	4550 ± 330	103 ± 8	93 ± 6
	AON	5640 ± 390	157 ± 11	99 ± 1
Coloaded H3SSgT	BODIPY	4270 ± 756	96 ±17	91 ± 2
	AON	3226 ± 636	90 ± 18	90 ± 3

[a] Data represents average ± SD (n = 3).
[b] Two component model fit of the autocorrelation function.

In contrast, the effective drug embedding efficiency of DoxHCl (as a hydrophilic small molecule drug) to H3gT and H3SSgT was determined to be 1.5 and 2.3 mg/g by fluorescence emission. The low embedding efficiencies resulted from the hydrophilicity of DoxHCl, thus lacking entropic driving forces in contrast to hydrophobic payloads. Due to the inability of AcX3gT to bind AON and the formation of large nanoparticles when H3gT encapsulates BODIPY, we will further focus on H3SSgT with the other two peptides being analyzed for comparison when appropriate.

The successful incorporation of BODIPY and AON into H3SSgT nanoparticles was confirmed by confocal laser scanning microscopy (CLSM) (Figure 24F,G). Even the low DoxHCl loading was confirmed by CLSM micrographs (Figure 24H). The size and morphology of the nanoparticles were measured by dynamic light scattering (DLS) and scanning electron microscopy (SEM), respectively (Figure 24B–E) and was confirmed by atomic force microscopy (AFM) for DoxHCl-loaded H3SSgT particles (Figure 35 (Supporting Information)). For AON- and DoxHCl-loaded particles only marginal differences in size and morphology were detected revealing smooth surfaces by SEM and diameters of 135 ± 22 nm and 165 ± 40 nm, respectively. In DLS similar diameters have been obtained (148 and 187 nm, respectively; Figure 24, Table 4), the differences being related to the drying effect in SEM measurements. Particles loaded with BODIPY preserved the size as AON-loaded nanoparticles (149 nm; Figure 24, Table 4), but smaller diameters and rougher surfaces were observed by SEM, compared to nonloaded H3SSgT nanoparticles (Figure 34 (Supporting Information), Table 4).

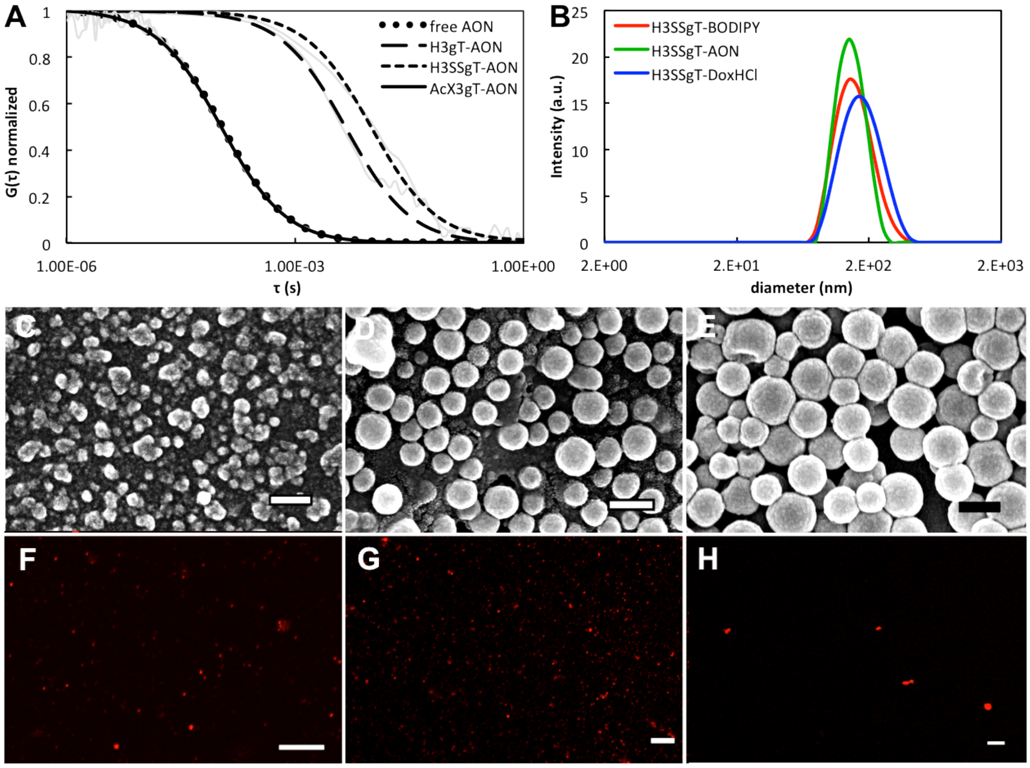

Figure 24. FCS autocorrelation curves (A) comparing free AON (dots) and AON complexed with AcX3gT (solid line), H3gT (broken line), and H3SSgT (dashes) nanoparticles. DLS data (B) for H3SSgT particles loaded with BODIPY (red), AON (green), and DoxHCl (blue). SEM and CLSM micrographs of H3SSgT nanoparticles loaded with BODIPY (C,F), AON (D,G), and DoxHCl (E,H). Scale bars for SEM micrographs are 500 nm (C–E), and 10 µm for CLSM micrographs (F–H).

Table 4. Hydrodynamic Diameters and PDIs from DLS Measurements of H3SSgT Nanoparticles Loaded with BODIPY, AON, and DoxHCl.

peptide nanoparticles	hydrodynamic diameter (nm)	PDI
H3SSgT-BODIPY	149	0.23
H3SSgT-AON	148	0.20
H3SSgT-DoxHCl	187	0.24
H3SSgT	218	0.37

The difference in morphology of BODIPY-loaded particles can be attributed to hydrophobic interactions of BODIPY with the hydrophobic gT sequence of the peptide and the formation of intermolecular π–π-stacking between BODIPY and tryptophan[229] interfering with the self-assembly process. The smaller sizes for AON-loaded compared to nonloaded particles can be attributed to the charge interaction resulting in more compact assemblies. Further analysis of the AON-loaded nanoparticles was also performed using energy dispersive X-ray spectroscopy (EDX) to identify the simultaneous presence of the sulfur in the linker and the phosphorus of the AON backbone. Indeed, both elements were detected in AON-loaded nanoparticles while no phosphorus signal was observed for particles loaded with BODIPY (Figure 25B,C). Also, zeta potential analysis showed an optimal DNA to peptide ratio at 40 µg AON/mg peptide where the surface charge approached from cationic, known to promote cell uptake,[230] toward neutral, known to decrease protein interactions and clearance (Figure 25A).[231]

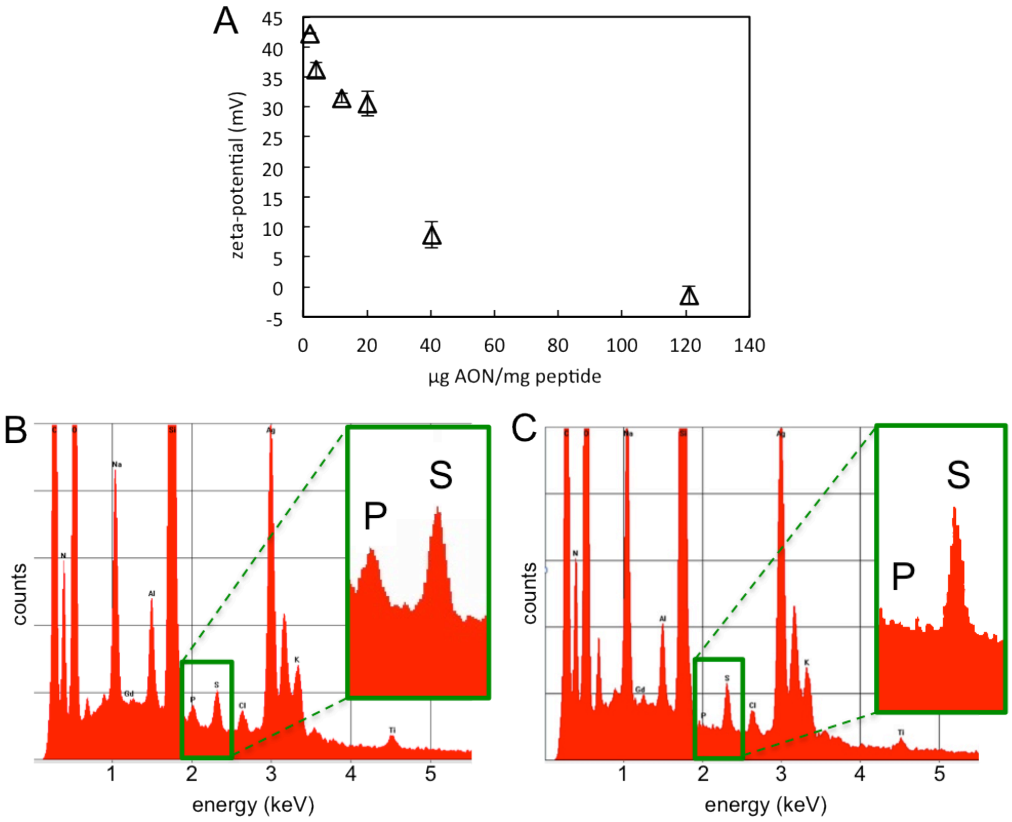

Figure 25. Zeta potential of various AON to H3SSgT peptide ratios (A). Energy-dispersive X-ray (EDX) spectrum of AON-loaded H3SSgT peptide nanoparticles (B). EDX spectrum of BODIPY-loaded H3SSgT nanoparticles (C).

3.3.3 Stimuli-Responsive Disintegration of Peptide Nanoparticles and Release of Payload

The implementation of a disulfide linker should allow H3SSgT nanoparticles to efficiently release loaded cargo molecules when exposed to physiological concentrations (10 mM) of dithiothreitol (DTT) through reductive cleavage of the hydrophilic from the hydrophobic sequence. LC-ESI-MS was used to detect the decomposition of H3SSgT peptide before and after addition of reducing agent, corresponding to the full length peptide ($[M+2H]^{2+}$: *m/z* 874.3; $[M+3H]^{3+}$: *m/z* 583.2) (Figure 23C) and the cleaved hydrophobic S–gT ($[M+H]^{+}$: *m/z* 1260.7; $[M+2H]^{2+}$: *m/z* 630.8) (Figure 23D). The detection of the H3–S sequence was not found due to it having a drastically lower molar absorption at 280 nm compared to the tryptophans on the gT sequence and it being hidden in the baseline. Next, H3SSgT nanoparticles were investigated using TEM and SEM to visualize if the cleavage of the peptide led to subsequent destruction of the nanoparticles. After addition of DTT the micrographs showed decomposition of the spherical nanoparticles compared to H3SSgT nanoparticles without DTT (Figure 26). The smaller particles represent partly decomposed peptide nanoparticles due to the disintegration of the particles. The population with larger diameters suggests the aggregation of the cleaved hydrophobic gT sequence due to their instability in aqueous solution (Figure 26B). TEM micrographs indicate the coexistence of various stages of decomposition, from intact peptide nanoparticles up to aggregates. AcX3gT and H3gT did not show particle decomposition when treated with DTT (Figure 27).

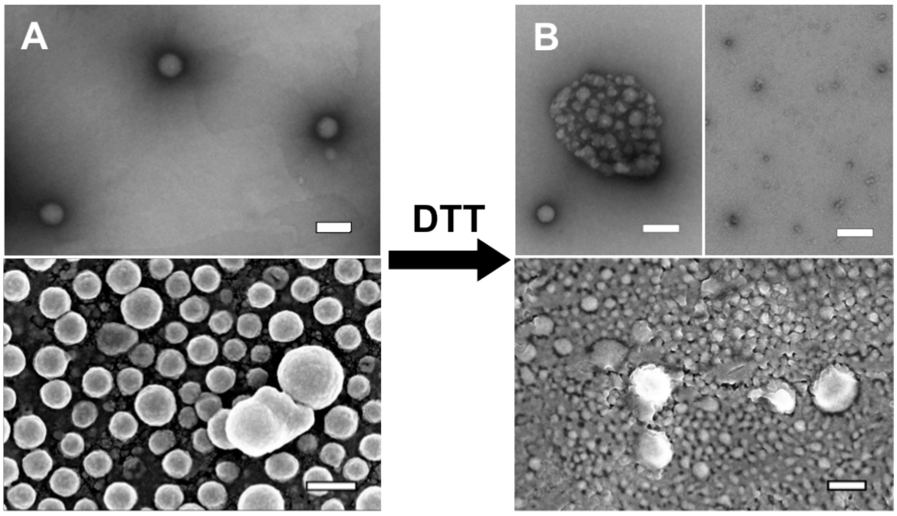

Figure 26. TEM (top) and SEM (bottom) micrographs of responsive H3SSgT nanoparticles before (A) and after treatment with DTT (B). Scale bars: 200 nm.

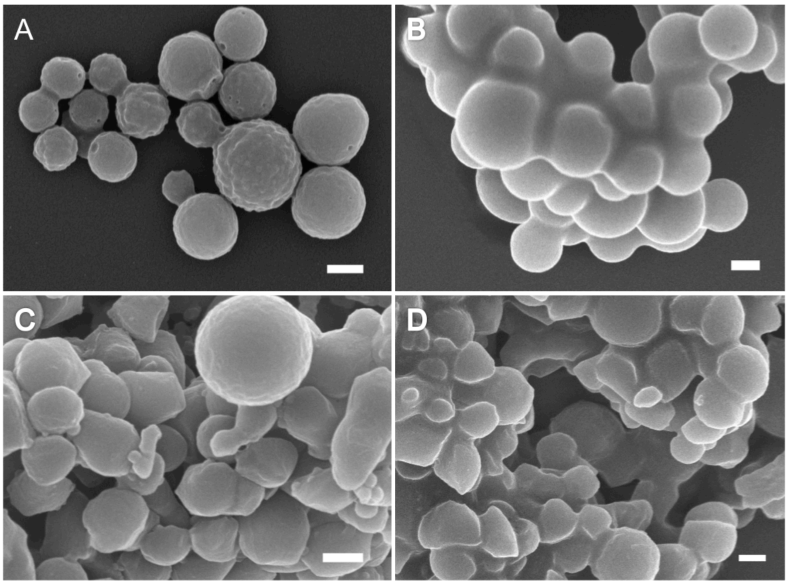

Figure 27. SEM micrographs of AcX3gT before (A) and after (B) DTT treatment, and H3gT before (C) and after (D) DTT treatment. Scale bars: 200 nm.

FCS was then used to assess the release of payload during particle decomposition. We selected BODIPY to be codelivered with AON because it is appropriate as a model molecule in terms of hydrophobicity and molecular weight, as well as being easily detected by FCS. Due to the incompatibility of DoxHCl with FCS detection, it was not feasible to use this small molecule drug for these release assays. 10 mM DTT was added to H3SSgT nanoparticles loaded with BODIPY or AON. Nanoparticles loaded with AON showed a fast release profile reaching approximately 50% after 15 min, while with BODIPY 50% release was not achieved until 30 min (Figure 28). Fast release under reductive conditions while maintaining payloads, when incubated in buffer differentiates our system from slowly releasing, pH-sensitive peptide nanoparticles showing a pH 5/pH 7.4-release ratio of 2.[224] Similarly, our system is faster than amphiphilic peptides passively releasing hydrophobic payload from gene/drug coloaded particles to 35% after 18 h,[144] or 40% after 60 h.[226] Both BODIPY- and AON-loaded nanoparticles showed almost complete disintegration by 120 minutes in the presence of DTT, with no release occurring without DTT (Figure 28).

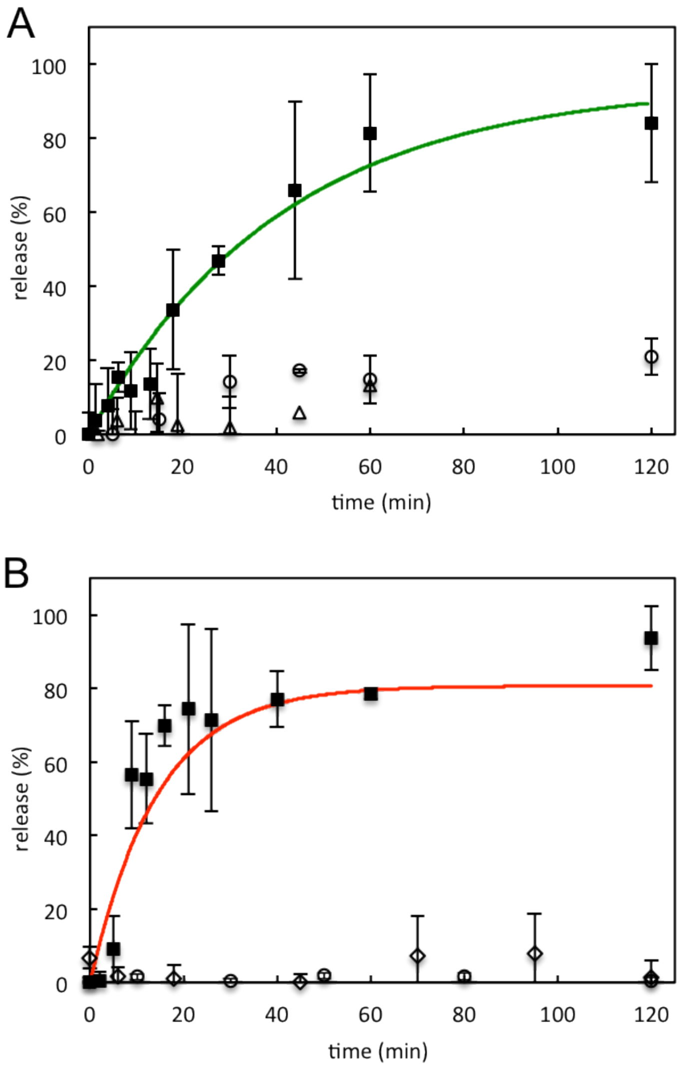

Figure 28. Release curves of BODIPY (A) or AON (B) loaded nanoparticles: squares represent H3SSgT+DTT, circles are H3SSgT–DTT, triangles are AcX3gT+DTT, and diamonds represent H3gT+DTT. Green and red lines are exponential fits of the H3SSgT data points using the Levenberg–Marquardt algorithm. Data represents average ± SD (n=3).

The slightly higher release rate of AON can be associated with their hydrophilicity, positioning them on the outer hydrophilic corona of the individual micelles, whereas the hydrophobic payload is trapped in the micelle core, shielded by the hydrophilic sequence of the peptide. The release from H3SSgT in the presence of DTT was then compared with AcX3gT, for BODIPY-loaded nanoparticles, or H3gT, for AON-loaded nanoparticles. AcX3gT and H3gT, treated with DTT, did not result in an increased population of freely diffusing payload indicating no release (Figure 28).

3.3.4 Coloading and Combined Release from H3SSgT Nanoparticles

To assess the suitability of the stimuli-responsive H3SSgT nanoparticles to serve as multifunctional codelivery carriers they were coloaded with both AON and BODIPY. The coloaded peptide nanoparticles were analyzed with CLSM to evaluate the simultaneous existence of both payloads in the particles (Figure 29A–C). An intensity profile through the micrograph indicated that not all particles are loaded equally (Figure 29D), but most of the particles contained both AON and BODIPY.

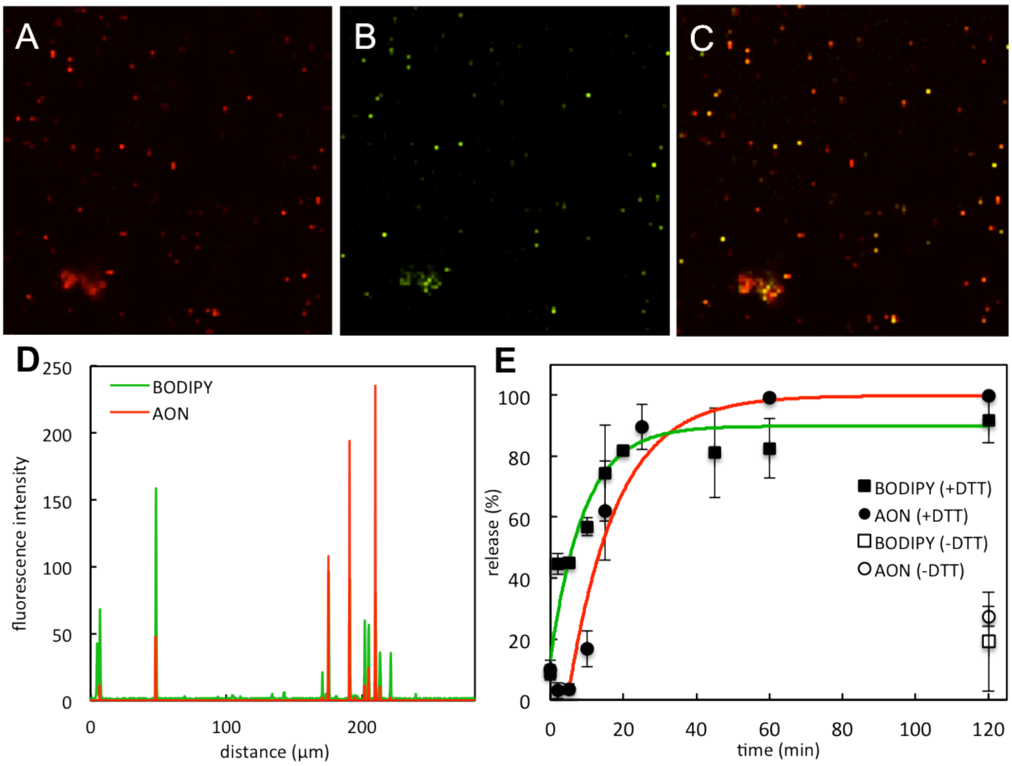

Figure 29. CLSM micrographs of AON- (A, red channel) and BODIPY- (B, green channel) coloaded H3SSgT nanoparticles (C, merged). Fluorescence intensity profile of a cross section of micrograph C (D). FCS release curve of BODIPY and AON from H3SSgT coloaded nanoparticles (E). Data represent average ± SD (n=3).

This observation is consistent with a colocalization analysis of an overlay image, revealing mostly colocalized fluorescence signals (Figure 30). The Mander coefficient was calculated to 0.844, where 1 represents perfect colocalization and 0 represents no colocalization.[232] Fluorescence cross-correlation spectroscopy (FCCS) was used to quantify the fraction of coloaded nanoparticles. FCCS is a dual-color variant of the FCS technique for the colocalization of two different fluorophores by cross-correlation of the individual channels.[233]

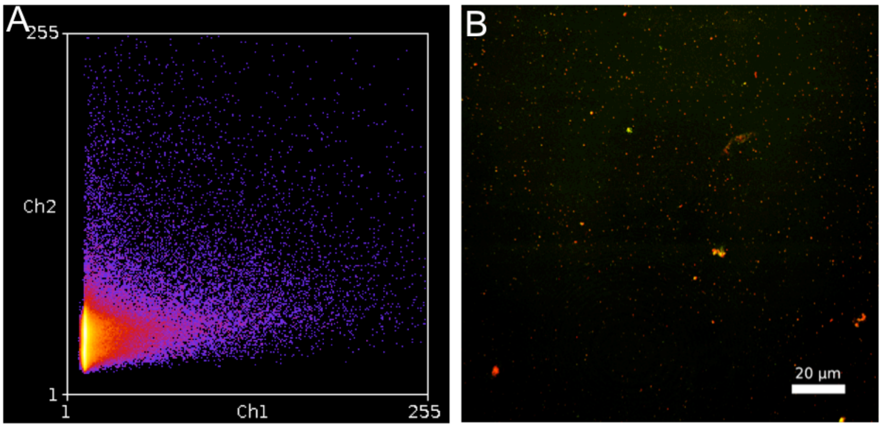

Figure 30. Colocalization analysis (A) and CLSM picture (B) of AON/BODIPY coloaded peptide nanoparticles. The fluorescence information was transformed to single channel 8-bit pictures. The Mander coefficient was calculated to 0.844 using the Mander coefficient plugin in ImageJ with CH1 corresponding to AON (red channel) and CH2 corresponding to BODIPY (green channel).

All data were normalized with the free cargo mixture equaling 0% cross-correlation and a standard double-labeled DNA equaling 100% cross-correlation. It resulted in a calculated complete coloading of the particles (Figure 31). To evaluate, if the responsiveness was influenced by coloading, corelease of both BODIPY and AON was compared by FCS to singly loaded nanoparticles. 50% of BODIPY was released faster from coloaded nanoparticles at around 10 min (Figure 29E) compared to singly loaded ones (≈ 30 min) (Figure 28A). This could be attributed to the additional interaction of both cargoes with the peptide, affecting the hydrophilic and hydrophobic interactions and potentially disturbing the assembly leading to less density within the nanoparticles, in contrast to peptide nanoparticles bearing only one type of guest molecules (Figure 28). The AON release behavior is almost congruent with singly loaded analogues due to different binding mode to the carrier.

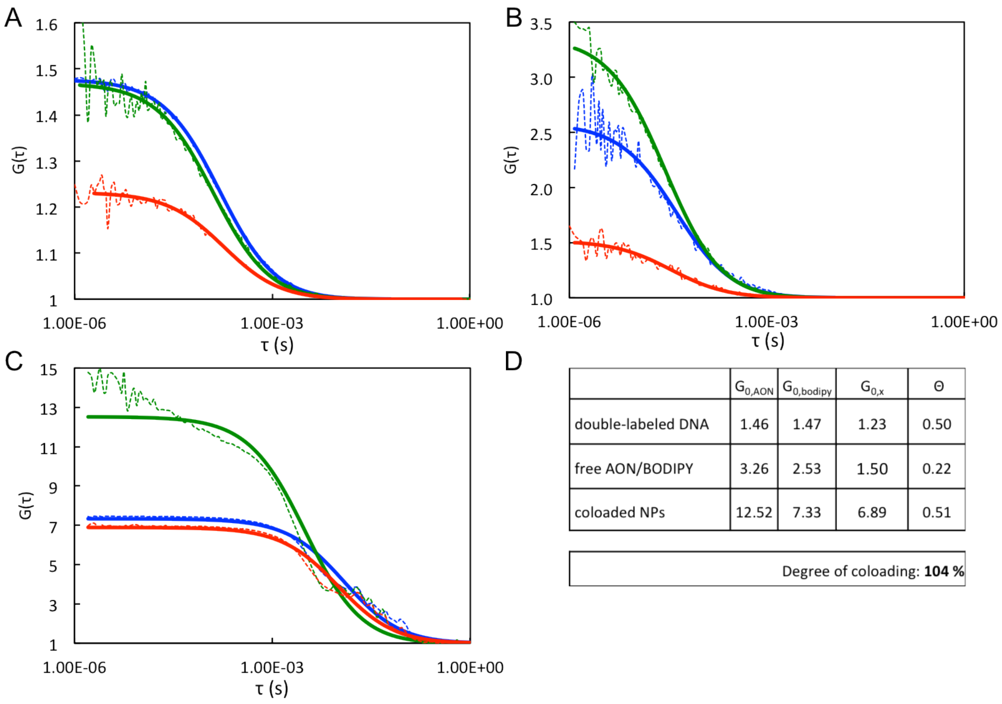

	$G_{0,AON}$	$G_{0,bodipy}$	$G_{0,x}$	Θ
double-labeled DNA	1.46	1.47	1.23	0.50
free AON/BODIPY	3.26	2.53	1.50	0.22
coloaded NPs	12.52	7.33	6.89	0.51

Degree of coloading: **104 %**

Figure 31. Correlation functions and fits of double labeled DNA (A), free payloads (B), and coloaded H3SSgT peptide nanoparticles (C). Cross-correlation (red), BODIPY (blue), and AON (green). Degree of coloading with respect to all BODIPY-loaded particles is given by $\theta = c_x/c_{total,\ BODIPY} = (G_{0,x}-1)/(G_{0,AON}-1)$, where G is the autocorrelation amplitude.[233]

3.3.5 Cell Uptake and Anti-Proliferation Activity

The reduction sensitive H3SSgT nanoparticles were evaluated for cytotoxicity to ensure the particles do not rapidly cause cell death. Peptide nanoparticles were nontoxic for concentration up to 1000 µg/mL at incubation times of 24 and 48 h (Figure 36A (Supporting Information)). Also, when the nanoparticles were treated with DTT prior to viability experiments the fragments did not show any toxicity after 48 h incubation (Figure 36C (Supporting Information)). Cell toxicity for the free peptides could not be achieved due to the spontaneous self-assembly in aqueous media. Cell uptake and intracellular behavior in HeLa cells were investigated with H3SSgT nanoparticles loaded with BODIPY or AON or coloaded with both BODIPY and AON. Qualitative analysis of the cells by CLSM showed increased uptake for singly loaded (Figure 37–38 (Supporting Information)) and coloaded peptide nanoparticles with BODIPY (Figure 32A) and AON (Figure 32C). Cellular uptake was additionally demonstrated to be comparable for coloaded particles when initially incubated in serum-containing medium (Figure 33). The increased uptake to cells was subsequently quantified by fluorescence-assisted cell sorting (FACS) analysis. This resulted in a 10-fold higher uptake of embedded AONs compared to free AONs when equivalent AON concentrations were applied to the cells (Figure 32E).

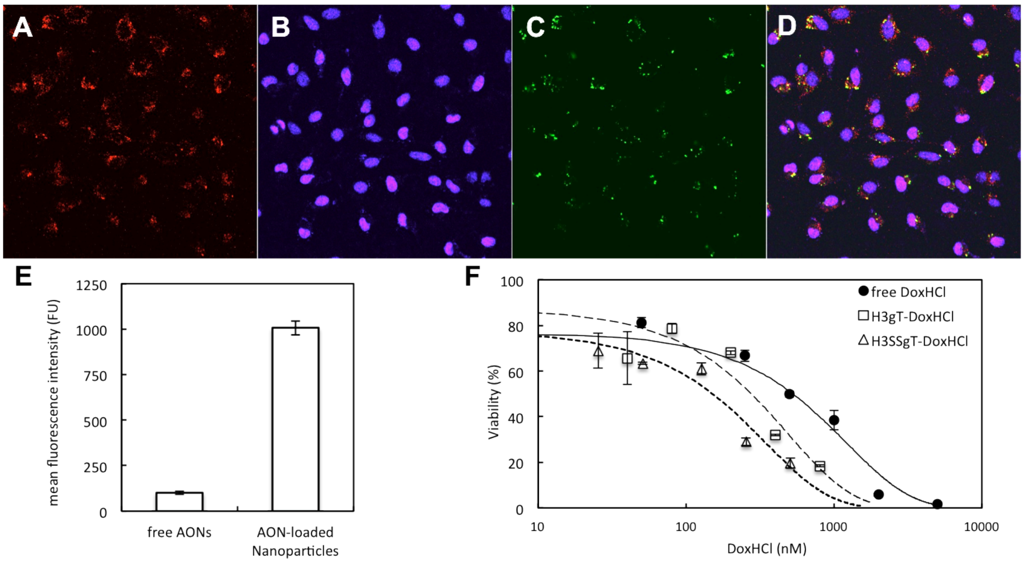

Figure 32. CLSM micrographs of coloaded H3SSgT peptide nanoparticle accumulation in HeLa cells with BODIPY channel (A), Hoechst nucleus stain (B), AON channel (C), and merged (D). FACS data of cell uptake for AON-loaded particles obtained from mean fluorescence intensities (E). Cell growth inhibition studies of free DoxHCl (solid line), or DoxHCl-loaded H3gT (broken line) and H3SSgT (dashed line) peptide nanoparticles (F). Data represents average ± SD (n = 3).

Free cargo as well as a mixture of BODIPY and AON (to ensure no cross interaction of molecules leading to uptake) did not show any detectable uptake (Figure 37–39 (Supporting Information)). This was expected for the negatively charged AON because it is commonly known that large anionic molecules do not internalize into cells. Free BODIPY is often shown to enter the cell; however, the amount of free BODIPY was the same as that in the particle solutions. At such low concentrations, free BODIPY was not enough to be seen by CLSM whereas when colocalized into peptide nanoparticles and more readily taken up due to the positive surface charge, higher signals have been observed.

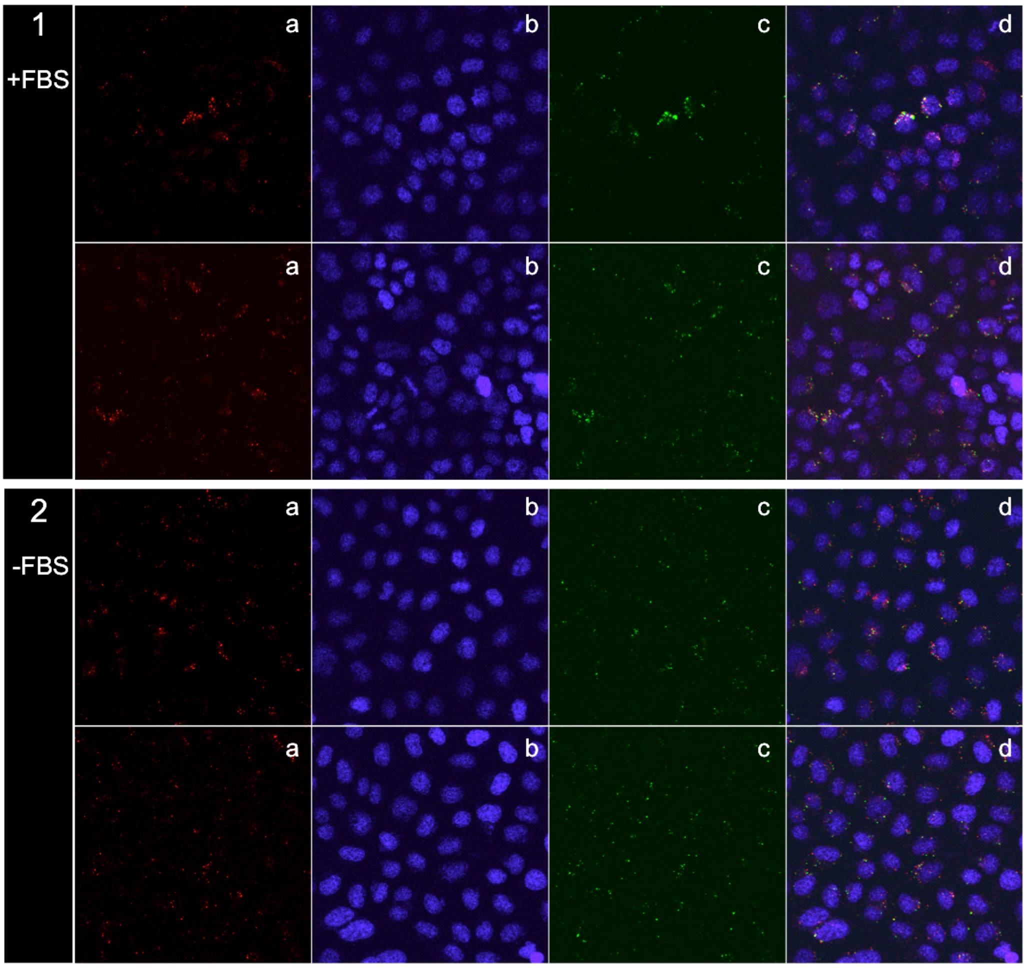

Figure 33. CLSM micrographs of coloaded nanoparticles with (1) and without (2) FBS. AON (a), Hoechst 33342 cell nuclei stain (b), BODIPY (c), and merge (d).

For subsequent cell growth inhibition studies only the H3gT and H3SSgT particles were loaded with hydrophilic DoxHCl to demonstrate the cell uptake and delivery qualities as well as the protection of the drug for more effectiveness. To assess the applicability of stimuli-responsive peptide nanoparticles as drug delivery system, DoxHCl was loaded into H3SSgT nanoparticles and applied to HeLa cells. The IC50 value of DoxHCl-loaded peptide nanoparticles was determined for H3SSgT compared to free DoxHCl (Figure 32F). The IC50 of DoxHCl-loaded H3SSgT peptide nanoparticles (H3SSgT) was found to be 150 nM, approximately four times lower than for free DoxHCl (530 nM). The decrease of IC50 is due to the hydrophilic character of DoxHCl, which has limited cell permeability compared to the nanoparticles. The decrease of IC50 value compared to free DoxHCl in HeLa cells is indirect proof of DoxHCl release from nanoparticles upon uptake, and supports our system as a good candidate for codelivery of small molecular weight molecules and AON. In addition, as the peptide fragments did not show any toxicity after 48 h incubation (Figure 36C (Supporting

Information)), we consider that the lower IC50 of DoxHCl-loaded H3SSgT nanoparticles than DoxHCl-loaded H3gT nanoparticles is the results of better DoxHCl release from H3SSgT nanoparticles due to the S–S breakage.

Also, when compared to the nonreducible DoxHCl-loaded H3gT nanoparticles (280 nM), H3SSgT had an IC50 about two times lower. This difference demonstrates the influence of the added stimuli-responsive linker. H3gT nanoparticles are taken up by cells similarly to H3SSgT but do not rapidly or efficiently release the DoxHCl, which is why the IC50 remains higher. The stimuli-responsive H3SSgT particles reveal, in addition to a similar uptake performance compared to H3gT, a potent release mechanism allowing the drug to achieve its full potential.

3.4 Conclusion

Development of nontoxic, biocompatible, and biodegradable nanocarriers for codelivery and stimuli-responsive release of oligonucleotides and small drugs remains a remarkable challenge. We designed and synthesized responsive amphiphilic peptides, which assemble into peptide nanoparticles that were engineered to condense oligonucleotides via electrostatic interactions with histidine and to incorporate small molecules within their multicompartment micellar structure. The nanoparticles are able to carry hydrophobic and hydrophilic payloads as well as oligonucleotides, which can be released upon a physiological trigger. In addition, the histidines in the primary sequence will support uptake to cells and subsequent proton sponge effect accelerating endosomal escape by its buffering capacity. Unlike most reported codelivery systems, our stimuli-responsive nanoparticles are purely peptidic in nature and therefore intrinsically biodegradable. In contrast to the previously reported peptidic codelivery system based on Fmoc-lysine-histidine constructs revealing sizes of up to 550 nm,[224] the diameters of the present nanoparticles match desired values for intravenous application. Furthermore, the implemented release mechanism is highly sensitive to a reduction potential in the cytosol to release coloaded payloads with great efficiency. All of these characteristics make our peptide nanoparticles a promising candidate for codelivery of multiple therapeutic payloads including hydrophobic Dox and plasmid DNA. Therefore, ongoing optimization experiments exploring the biocompatibility of these nanoparticles, their stability in animal blood serum, and *in vivo* biodistribution and pharmacokinetic studies are planned to improve this system into a functional delivery system with high therapeutic effects.

3.5 Supporting Information

3.5.1 Further Characterization of Nonloaded and Loaded Nanoparticles

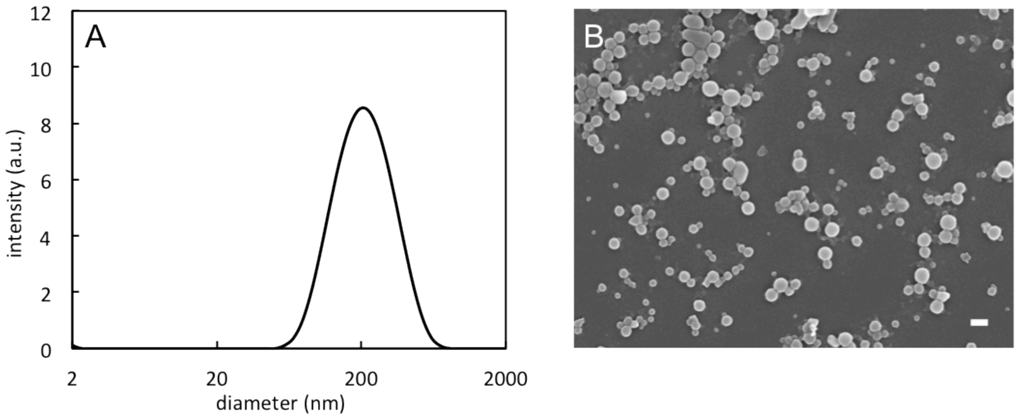

Figure 34. DLS of nonloaded H3SSgT peptide nanoparticles (A). SEM micrograph of nonloaded H3SSgT nanoparticles (B). Scale bar: 200 nm.

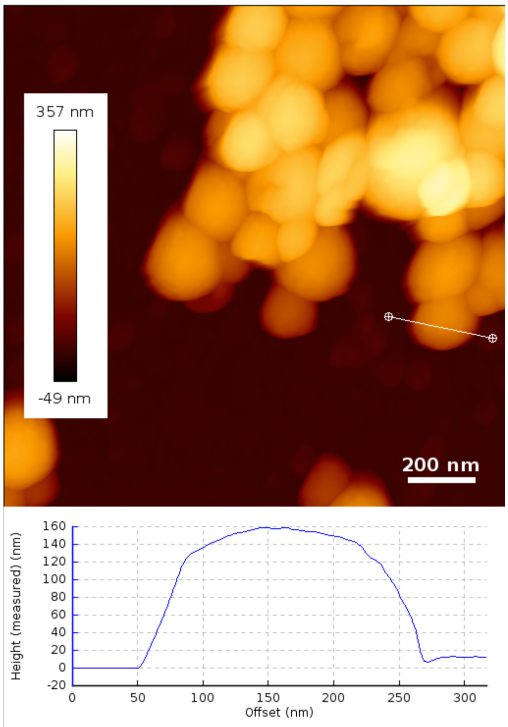

Figure 35. AFM profiles of DoxHCl-loaded H3SSgT peptide nanoparticles.

3.5.2 Toxicity Studies

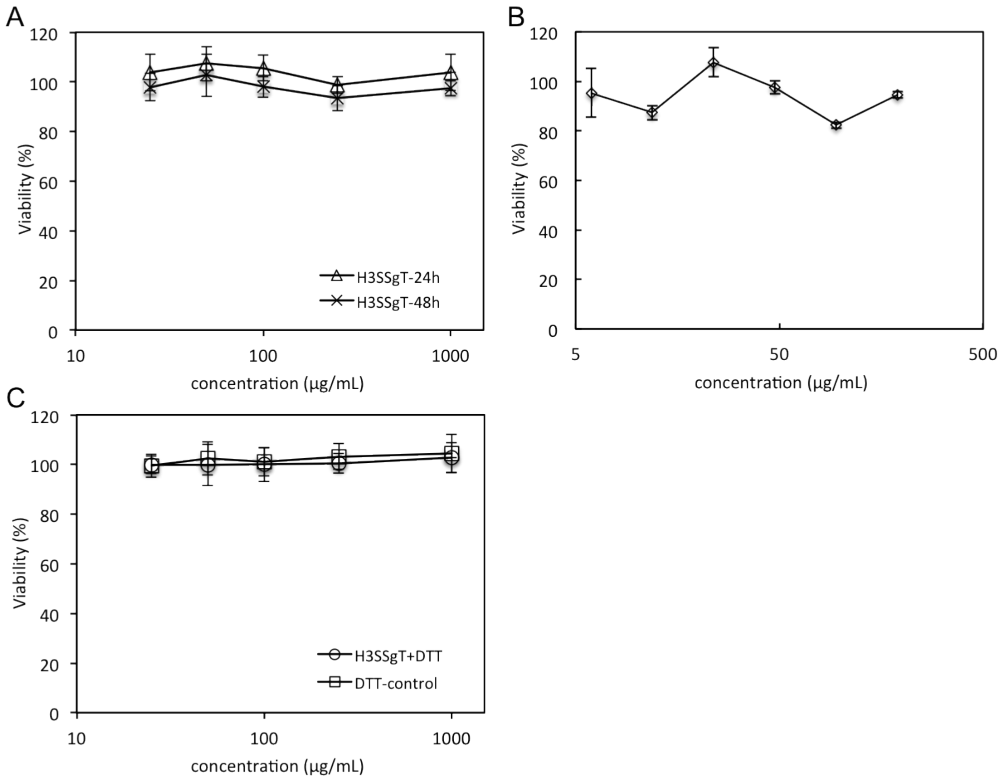

Figure 36. MTS cell viabilities of HeLa cells treated with H3SSgT nanoparticles for 24 and 48 h (A) and H3gT nanoparticles for 24 h (B). MTS viability of DTT treated H3SSgT (C). Values represent average ± SD (n=5 (A/C), n=3 (B)).

3.5.3 Cell Uptake of Singly Loaded Nanoparticles and Free Payloads

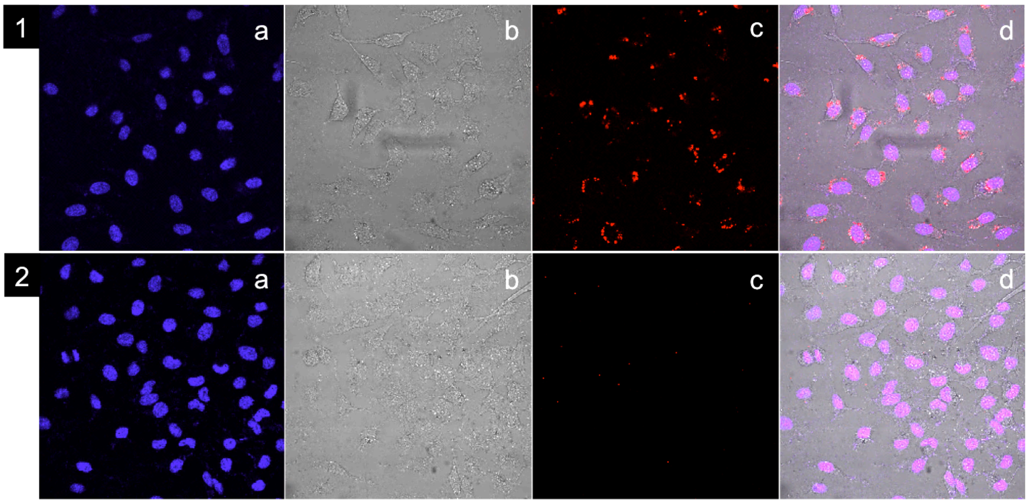

Figure 37. LSM micrographs of AON-loaded particle uptake to HeLa cells (1). Free AON on HeLa cells (2). Hoechst 33342 cell nuclei stain (a), transmission (b), AON (c), and merge (d).

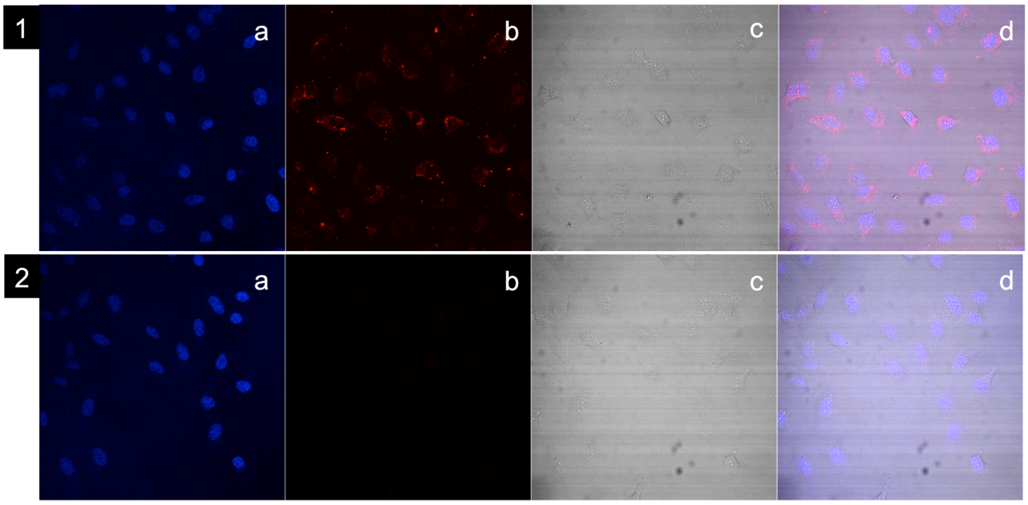

Figure 38. LSM micrographs of BODIPY-loaded particle uptake to HeLa cells (1). Free BODIPY on HeLa cells (2). Hoechst 33342 cell nuclei stain (a), BODIPY (b), transmission (c), and merge (d).

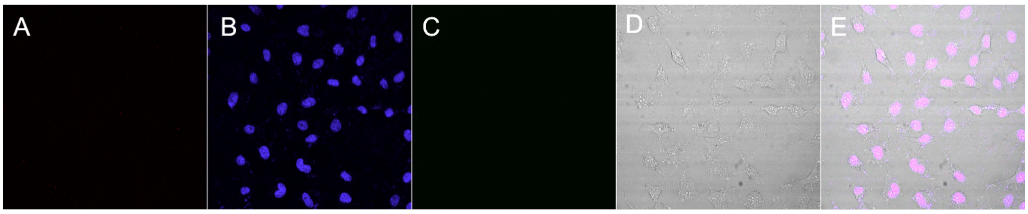

Figure 39. CLSM micrographs of HeLa cells incubated with a mixture of AON and BODIPY. AON (A), Hoechst 33342 cell nuclei stain (B), BODIPY (C), transmission (D), and merge (E).

Chapter 4

4 Polylysine- and Polyhistidine-Based Amphiphilic Peptides for Plasmid DNA Transfection

The following chapter describes the development of transfection agents for plasmid DNA delivery self-assembled from amphiphilic peptides. Various peptide architectures, comprising different lengths of hydrophobic sequences, derived from gramicidin A, in conjunction with polyhistidine or polylysine are examined and discussed on their transfection performance and toxicity to mammalian cells.

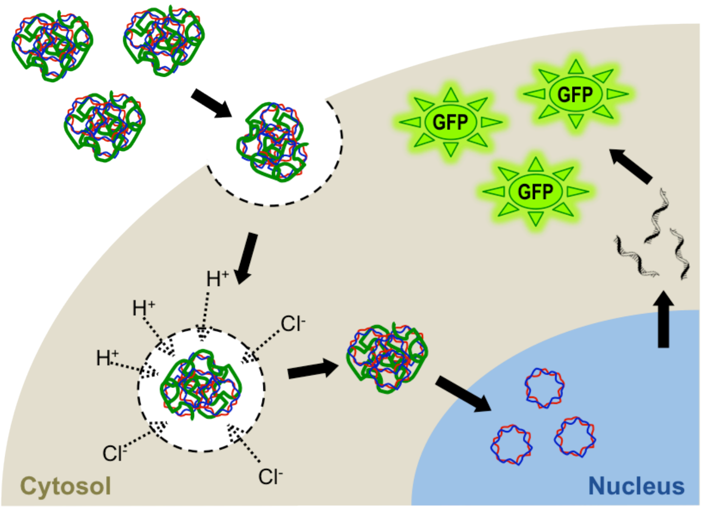

Figure 40. Polylysine- and polyhistidine-based amphiphilic peptides condensing and delivering plasmid DNA to the cell nucleus inducing production of mRNA encoding for green fluorescent protein.

4.1 Abstract

In this study, amphiphilic peptides comprised of polylysine or polyhistidine in conjunction with hydrophobic sequences derived from gramicidin A are described and synthesized to study the effect of the lysine block length and the differences between polyhistidine and polylysine regarding gene delivery. The peptides were synthesized by standard Fmoc-based solid phase peptide synthesis. Peptide nanoparticles were formed by first condensing plasmid DNA (pDNA) at various nitrogen-to-phosphorus ratios (N/P-ratios) followed by self-assembly. pDNA-loaded constructs were thoroughly characterized and examined on their *in vitro* transfection performance using U87 cells. First, H3SSgT, introduced in chapter three, capable of codelivering and -releasing antisense oligonucleotides (AON) and small molecule drugs in a reduction-responsive manner was examined on its suitability for delivering pDNA. The N/P-ratios were optimized to 10 according to electrophoretic mobility shift assays (EMSA) and zeta-potential measurements. Incubation with reducing agent led to partial release of the incorporated pDNA. Secondly, the newly introduced polylysine peptides AcK6gA and K10gA were examined on their pDNA condensing and particle formation abilities. They revealed high pDNA-loading capability and formed nanoparticles similar in shape and size compared to pDNA-loaded H3SSgT nanoparticles. AcK6gA and K10gA nanoparticles achieved transfection efficacies at levels of the gold standard Lipofectamine (~60 %) while H3SSgT nanoparticles revealed a fourfold lower efficiency (15 %). Increased surface charge induced enhanced transfection efficiencies; however, it also led to elevated cytotoxicity, which is frequently observed for polycationic transfection agents. Intense GFP fluorescence of transfected U87 cells demonstrated functionality of the rationally designed amphiphilic peptides and suggests further optimization of the presented system to achieve a nontoxic highly efficient gene transfection agent.

4.2 Introduction

In the past decades, nonviral gene therapy gained considerable attention, due to a much better safety profile compared to viral gene delivery vectors.[234] A vast array of transfection agents have been developed based on polycations such as poly-L-lysine,[235-237] poly(ethyleneimine) (PEI),[238-240] and polyamidoamine (PAMAM).[241,242] However, the resulting polyplexes usually exhibit an excess quantum of positive charge, interacting with cell membranes and inducing lethal cytotoxicity, which remains a major challenge.[79,80,243-246] To overcome this drawback, polycations were conjugated to molecules with various physicochemical properties to promote nanoparticle formation driven by entropic forces. Numerous architectures of lipids, polymers, and peptides have been investigated on their capability of delivering nucleic acids (Chapter 1). In this chapter, we will focus on lysine- and histidine-rich molecular designs to achieve this goal via well-defined monodisperse peptide sequences. While polylysine has exceptional nucleic acid condensing capabilities, polyhistidine has the additional feature of supporting the proton sponge effect and therefore, accelerating endosomal escape of the nanoparticles to the cytosol, which is essential for an effective treatment.[247]

Studies have shown that relatively short and defined polylysine sequences, conjugated to hydrophobic moieties are promising noncytotoxic transfection carriers. Pentalysine peptides were reported to have moderate nontoxic transfection capabilities when coupled to different lengths of hydrophobic peptide sequences.[248] Histidine–lysine peptides exhibit also great promise in noncytotoxic gene delivery. Various nonapeptides comprising histidines and lysines conjugated to PEI demonstrated increased gene transfection efficiency compared to bare PEI, thereby highlighting the positive transfection effect mediated by these peptides.[249] Also, polylysine–Tat constructs[250] and disulfide-linked histidine–arginine peptides[251] revealed promising transfection performances. Although, polylysine has been reported to be cytotoxic at certain conditions,[252] other studies have also shown nontoxicity and immunocompatibility of these peptides.[253]

Herein, we describe the design and synthesis of amphiphilic peptides comprising polylysine and hydrophobic sequences inspired form gramicidin A (gA). The sequences are constructed to interact with plasmid DNA via electrostatic interaction. Nanoparticles are formed by self-assembly of the amphiphilic molecules. The polylysine sequences were designed to contain a glycine spacer after every third amino acid, providing better flexibility of the peptides to arrange along the pDNA. The transfection efficiency was investigated using pDNA encoding for green fluorescent protein (GFP) and compared to previously introduced H3SSgT. Similarly, the cytotoxicity was evaluated using different methods.

4.3 Results and Discussion

4.3.1 Synthesis and Characterization of Peptides

In this study, AcK6gA and K10gA were examined on their capability to form nanoparticles with pDNA and compared to previously reported H3SSgT (Chapter 3). All peptides were synthesized on Rink amide resin using standard Fmoc solid phase peptide synthesis (SPPS) technique and purified via high performance liquid chromatography (HPLC). The hydrophilic regions of the newly introduced peptides consist of different lengths of polylysine separated by glycine after every third lysine to provide flexibility along the backbone, potentially increasing plasmid DNA condensing capabilities (Table 5). AcK6gA and K10gA bear hydrophobic sequences derived from gramicidin A (gA) while H3SSgT is equipped with a hydrophobic region comprised of gT, a truncated version of gA. AcK6gA was previously reported to form multilamellar structures when mixed with the oppositely charged glutamic acid analogue,[28] H3SSgT was described to form nanoparticles with sizes around 100–200 nm (Chapter 3). The codes and sequences of the peptides as well as the chemical composition of the linker-unit are listed in Table 5. Lysines and histidines are known to condense pDNA efficiently.[227,254] Furthermore, histidines or combinations of lysines and histidines promote cell uptake and have a positive effect on transfection efficiency.[254-257] The number of charges per molecule, chemical nature, and resulting cooperative effects of carrier molecules are crucial factors for pDNA binding and condensing abilities, which also affect cell uptake and transfection performance.[258,259]

Table 5. Codes, Sequences, and Chemical Structure of Amphiphilic Peptides and Reducible Linker, Including Molecular Masses.

code/name	sequence/chemical structure	mass (g mol^{-1})
Z	-NH-(CH$_2$)$_2$-S–S-(CH$_2$)$_2$-NH-CO-(CH$_2$)$_2$-CO-	
-gA	-V-G-A-DL-A-DV-V-DV-[W-DL]$_3$-W-*CONH*$_2$	1711.1
-gT	-[W-DL]$_3$-W-*CONH*$_2$	1100.3
H3SSgT	*H*$_2$*N*-H$_3$-Z-[W-DL]$_3$-W-*CONH*$_2$	1746.8
AcK6gA	*Ac*-K$_3$-G-K$_3$-V-G-A-DL-A-DV-V-DV-[W-DL]$_3$-W-*CONH*$_2$	2678.3
K10gA	*H*$_2$*N*-K-[G-K$_3$]$_3$-V-G-A-DL-A-DV-V-DV-[W-DL]$_3$-W-*CONH*$_2$	3263.1

4.3.2 Plasmid DNA Condensation and Nanoparticle Formation

The synthesized peptides AcK6gA, K10gA, and H3SSgT were used to form nanoparticles with pDNA via electrostatic interaction and subsequent self-assembly driven by the amphiphilic character of the peptides. The hydrophilic sequences were synthesized to different lengths of polylysine (hexalysine and decalysine) or polyhistidine. Both amino acids differ in their pK_a. While lysine has a pK_a of 10.7 for the ε-amino group, histidine exhibits a pK_a of 6.0 for the imidazole nitrogen. Plasmid DNA encoding for GFP was condensed within peptide nanoparticles at different N/P-ratios.

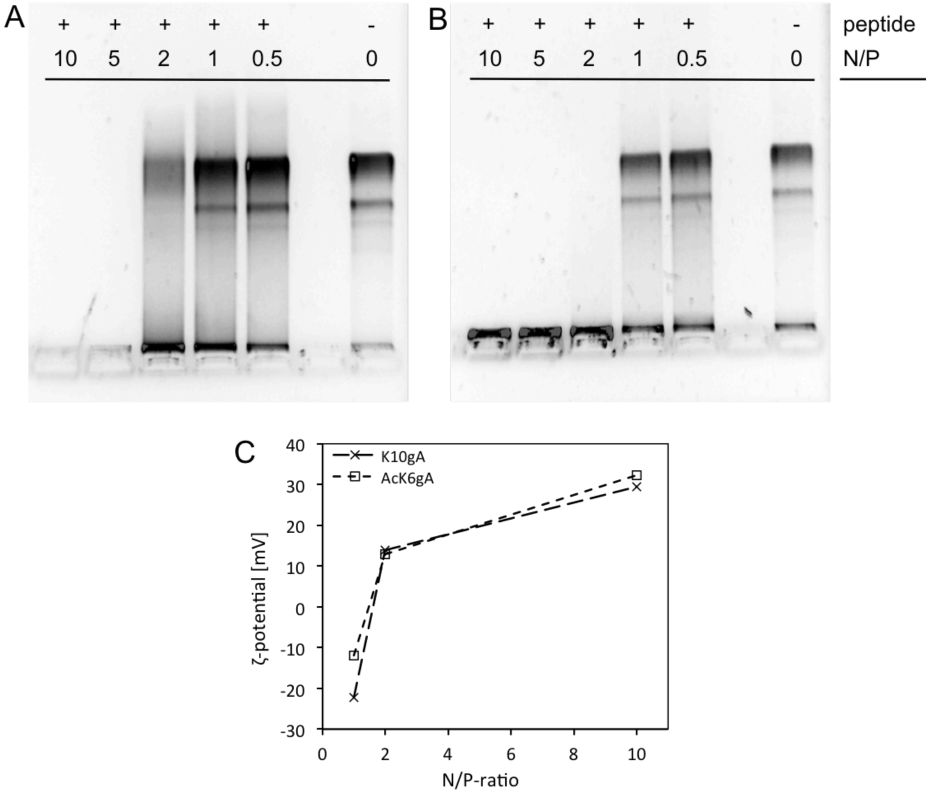

Figure 41. EMSA (1.2 % agarose gel) and zeta potential of pDNA-loaded AcK6gA and K10gA nanoparticles. pDNA-loaded AcK6gA nanoparticles at N/P-ratios of 0.5, 1, 2, 5, and 10 (A); pDNA-loaded K10gA nanoparticles at N/P-ratios of 0.5, 1, 2, 5, and 10 (B); zeta potential of pDNA-loaded AcK6gA and K10gA nanoparticles at N/P-ratios of 1, 2, and 10 (C).

In order to optimize the N/P-ratio of each individual peptide the binding abilities were determined by electrophoretic mobility shift assays (EMSA) using 1.2 % (w/v) agarose gels and zeta potential measurements. EMSA indicated a shift from partially bound pDNA at an N/P-ratio of 1 to fully condensed pDNA at an N/P-ratio of 5 for AcK6gA (Figure 41A). K10gA revealed complete condensation of pDNA at an N/P-ratio of 2 (Figure 41B), slightly lower compared to AcK6gA. This could be attributed to a cooperative binding effect. K10gA reveals a higher number of charges per molecule, which cooperatively supports overall condensation of pDNA, compared to AcK6gA. However, zeta potential measurements revealed rather similar values for both peptides, changing to positive surface charges above an N/P-ratio of 2 (Figure 41C). The required N/P-ratios for a complete pDNA condensation are in the range of other reported peptide-based systems.[260,261] These indicate very effective pDNA-binding of the peptides via electrostatic interaction. It allows for the formation of moderately positively charged constructs presumably avoiding toxic effects emerging from interaction of positive charges with the phospholipid bilayer of cell membranes. The amphiphilic peptides probably arrange along the pDNA by electrostatic interaction and assemble subsequently to spherical nanoparticles through intermolecular hydrophobic interaction of the gA-sequence.

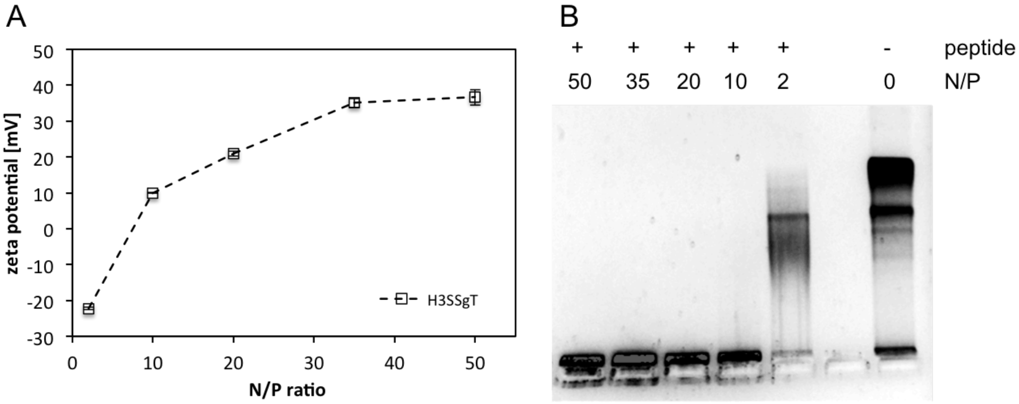

Figure 42. Zeta potentials and EMSA of H3SSgT-pDNA nanoparticles. Zeta-potentials (A), and EMSA (B) of GFP-encoding pDNA loaded H3SSgT nanoparticles using different N/P-ratios ranging from 2 to 50.

EMSA of H3SSgT, bearing a polyhistidine as pDNA condensing sequence revealed complete binding at an N/P-ratio of 10 (Figure 42A). However, the investigated values for N/P-ratios from 2 to 50 do not allow conclusive statements and comparisons to the former constructs built from AcK6gA and K10gA. Zeta potentials of pDNA-loaded H3SSgT nanoparticles were positive above N/P-ratios of 10 (Figure 42B), but comparably moderate in respect of the polylysine peptide nanoparticles (AcK6gA and K10gA). A slightly positive surface charge is known to support cell uptake and can lead to better efficiency;[230,246,262] however, higher surface charge density can also lead to protein corona formation and clearance[231] and toxic effects.[243-245] Moreover, noncharged particles tend to aggregate while charged analogs reveal repulsive interactions avoiding aggregation behavior. Thus, for further studies the nanoparticles were assembled using the lowest N/P-ratio to still obtain slightly positive zeta potential values.

TEM was used to assess the morphology and size of the nanoparticles, revealing spherical shapes and diameters of 45 ± 10 nm for AcK6gA (N/P=5.5), 53 ± 13 nm for K10gA (N/P=10), and 60 ± 13 nm for H3SSgT (N/P=20) (Figure 43). The sizes are at the lower limit of the optimal range for drug/gene delivery carriers, which is generally regarded to be around 100–200 nm, also depending on shape, surface chemistry, and specific target cells.[263]

However, CALAA-01 for instance was reported to reveal the best efficacy at diameters of around 50 nm, therefore the obtained values lay in a promising range for being therapeutically active.[264]

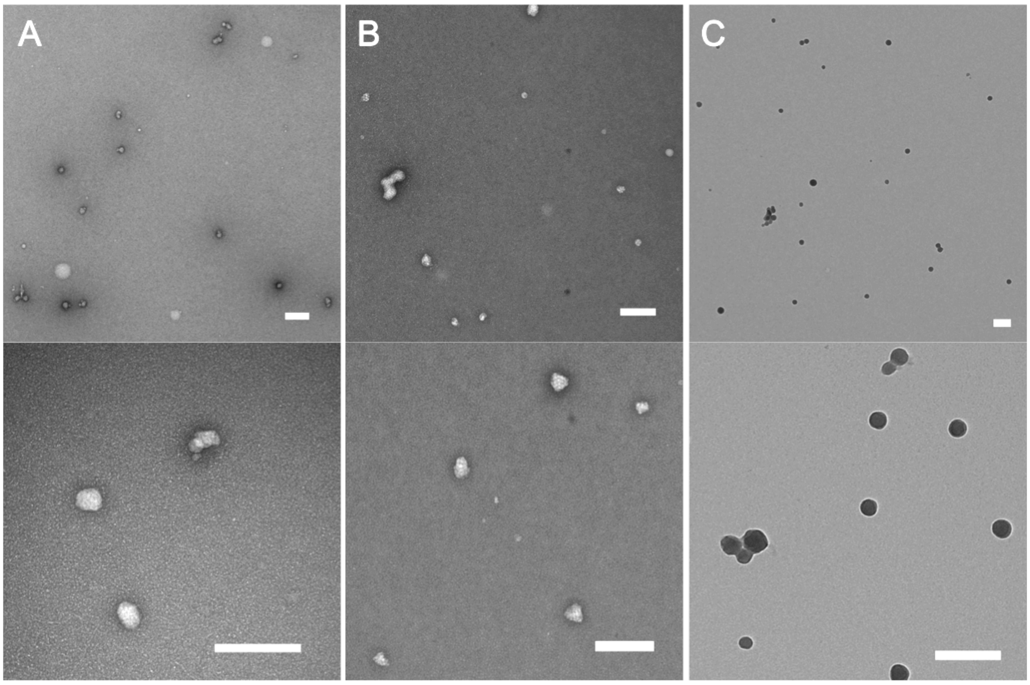

Figure 43. Representative TEM micrographs of pDNA-loaded peptide nanoparticles. pDNA-loaded AcK6gA (N/P=5.5) (A), K10gA (N/P=10) (B), and H3SSgT nanoparticles (N/P=20) (C). Scale bars: 200 nm.

4.3.3 Reduction Triggered Release of pDNA From H3SSgT Nanoparticles

Only H3SSgT among the other peptides in the present study carries a responsive linker as described in more detail in Chapter 3. The triggered release of pDNA *in vitro* was therefore only studied for this peptide. In contrast to codelivery of AON and small molecules, the peptide nanoparticles were assessed on their capability to carry and release larger nucleic acids (pDNA). pDNA was condensed within H3SSgT nanoparticles at N/P-ratios of 10 and 20 due to previously determined slightly positive surface charge, which is considered to promote cell uptake while preventing protein corona formation.[230,231] Reductive release of pDNA was subsequently assessed by EMSA after addition of reducing agent (DTT) (Figure 44A). Release of pDNA was observed for H3SSgT nanoparticles when incubated with DTT while nontreated nanoparticles revealed no band for noncondensed pDNA. However, a fair amount of pDNA is still condensed within the nanoparticles indicated by nonmigrated bands in the agarose gel (Figure 44B). pDNA release form H3SSgT nanoparticles with N/P-ratios of 10 and 20 was monitored for 6 h. Faster release was observed at lower N/P of 10 compared to self-assemblies with an N/P of 20. Qualitative analysis of the gels revealed considerably slow release in contrast to previously reported AON-release profiles (Figure 44C). It can be attributed to the significantly larger size of the pDNA in contrast to AON, which possibly results in more entanglement and less defined assembly architecture. This could additionally alter the accessibility of the reduction responsive linker units within the nanoparticles. However, the results confirm release of pDNA in a slow manner when treated with reducing agent, which is advantageous regarding the protective properties, potentially prolonging therapeutic effects *in vivo*. The slow release indicates preserved functionality of the nanoparticles when loaded with the significantly larger plasmid DNA compared to AONs (Chapter 3).

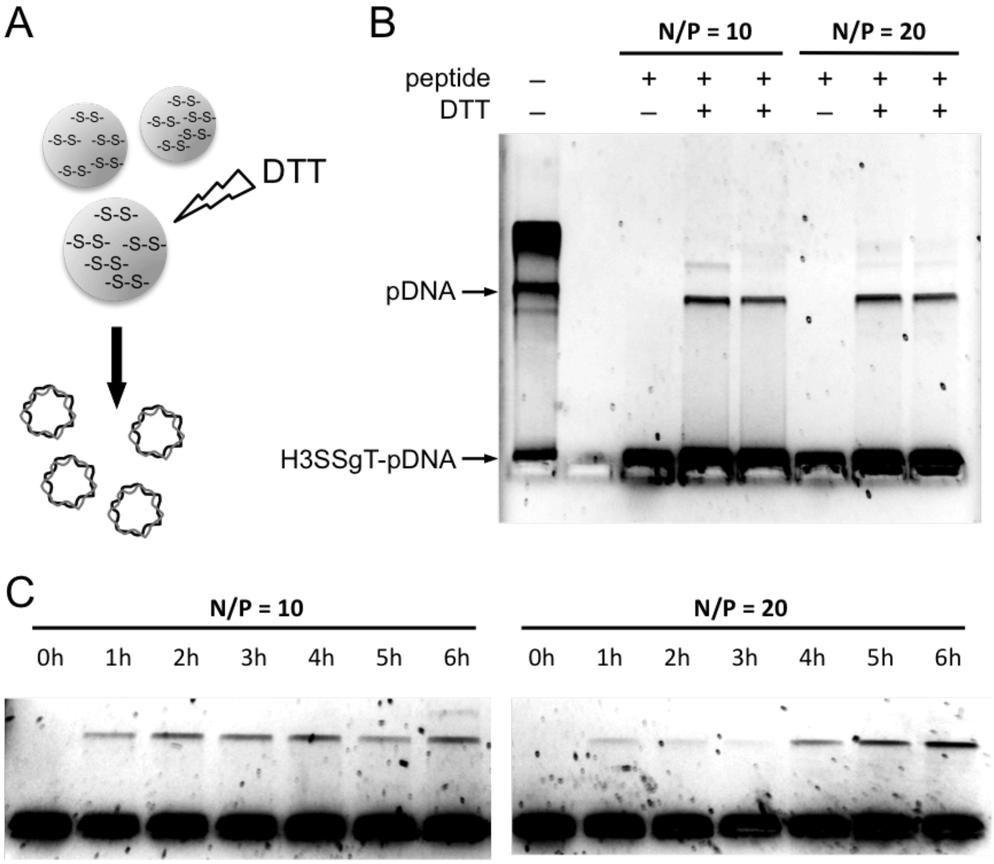

Figure 44. Reductive degradation and pDNA release from peptide nanoparticles (A); Agarose gels: release after 24 h incubation with 200 mM DTT (B); Release of pDNA monitored over 6 h (C).

4.3.4 Transfection Studies

For testing the *in vitro* transfection performance of AcK6gA, K10gA, and H3SSgT peptide nanoparticles, they were loaded with GFP-encoding pDNA as reporter gene and subsequently applied to U87 cells. The transfection efficiencies were quantified via fluorescence levels of the expressed GFP. pDNA-loaded AcK6gA particles were formed using N/P-ratios of 5.5 and 20 to obtain slightly positively charged nanoparticles. For pDNA-loaded K10gA nanoparticles N/P-ratios of 10 and 20 were used for transfection studies. The nanoparticles were incubated with U87 cells and GFP expression levels were assessed 24 and 48 h after application using flow cytometry. Simultaneously, the populations of the gated cells (forward- vs. sidescattering) were determined, relative to a nontreated control, reflecting the compatibility of the nanoparticles with mammalian cells and potential toxicity caused by the peptide–pDNA constructs. These provide information about the ratio of viable cells to apoptotic, necrotic, and dead cells. The values were compared to Lipofectamine, applied at 0.5 µg/well due to optimization experiments (0.1–1.0 µg/well) revealing no increase in transfection efficiency at amounts above 0.5 µg/well (Figure 45). pDNA-loaded AcK6gA nanoparticles at an N/P-ratio of 5.5 were incubated with U87 cells to obtain 1.0 µg and 1.7 µg pDNA/well, respectively (Figure 46). At an N/P-ratio of 20, 1 µg pDNA/well were applied. Flow cytometry analysis of AcK6gA nanoparticles incubated for 24 h revealed 6 % transfection and a relative population of around 65 % for both, 1.0 and 1.7 µg pDNA/well (N/P=5.5). At an N/P-ratio of 20 a transfection efficiency of 14 % was obtained with a drastically decreased population (18 %) relative to nontreated control cells. After 48 h incubation, the transfection reached 12 % and 24 % for 1.0 and 1.7 µg pDNA/well (N/P=5.5), respectively. The relative cell populations were calculated to 79 and 57 %. At N/P=20 transfection reached values of 41 % (relative population: 30 %). In comparison, the gold standard transfection agent Lipofectamine revealed transfection values of 25 and 45 % at 24 and 48 h incubation, respectively, revealing relative populations of around 48 % (Figure 46). The reverse proportionality of transfection efficiency and relative population with increasing pDNA amount and N/P-ratio can be attributed to the elevated levels of toxicity emerging from the positively charged particles interacting with the phospholipid bilayer of cell membranes.[246] This surface charge dilemma is well known for transfection agents and remains a major challenge in the development of effective and nontoxic gene delivery systems.

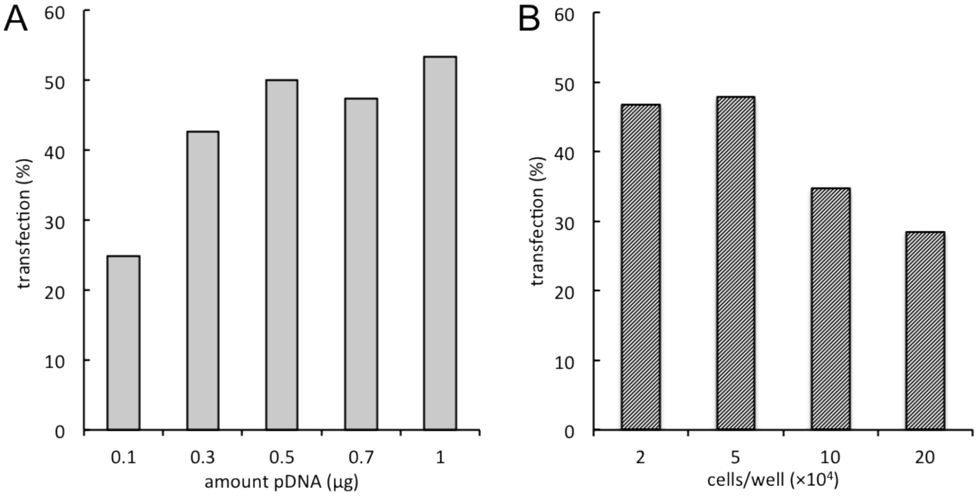

Figure 45. Flow cytometry optimization of pDNA amount (A) and number of cells (B) per well in 24-well cell culture plates for transfection experiments using Lipofectamine.

Similarly, pDNA-loaded K10gA nanoparticles were investigated on their transfection performance and toxicity using U87 cells (Figure 47). Incubation for 24 h led to comparable transfection efficiencies of 16 % and 11 % for 1.0 and 2.0 µg pDNA/well (N/P=10), respectively. For nanoparticles at an N/P-ratio of 20 (1.0 µg pDNA/well) a transfection efficiency of 14 % was obtained. Populations relative to nontreated control cells were found at 57 % (1.0 and 2.0 µg pDNA/well; N/P=10) and 40 % (1.0 µg pDNA/well; N/P=20). When incubated for 48 h, K10gA nanoparticles showed the same tendencies as observed for AcK6gA nanoparticles: delivery of 1.0 and 2.0 µg pDNA/well (N/P=10) revealed transfections of 37 and 47 %, respectively. Particles with N/P=20 showed 58 % transfection. In contrast to AcK6gA-NPs, K10gA-NPs were less toxic to U87 cells, indicated by relative populations of around 65 % (Figure 47), more than twice as high as for AcK6gA nanoparticles.

Transfection efficiency of pDNA-loaded H3SSgT nanoparticles was analyzed using previously determined N/P-ratio of 2, and compared to nanoparticles formed at an N/P-ratio of 50. The peptide nanoparticles were applied at 0.8 and 1.5 µg pDNA/well and analyzed using flow cytometry (Figure 48). At an N/P-ratio of 2, only marginal transfection of 3–4 % was obtained (0.8 and 1.5 µg pDNA/well) while cell populations were not altered by the nanoparticles and remained at around 80 % relative to nontreated cells. When using nanoparticles at N/P-ratio of 50, transfection efficiency up to 15 % was achieved, but the relative population of gated cells decreased to 50 and 30 % for 0.8 and 1.5 µg pDNA/well, respectively.

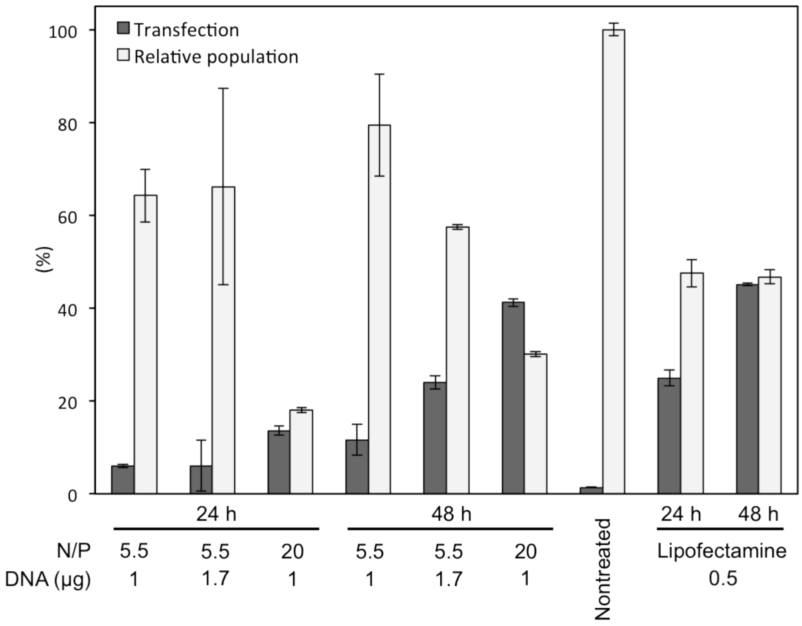

Figure 46. Flow cytometry transfection efficiencies and relative populations of GFP-transfected U87 cells using pDNA-loaded AcK6gA nanoparticles. Populations were gated according to a nontreated control. Each data point represents the average ±SD of two individual experiment comprising 10^4 cells.

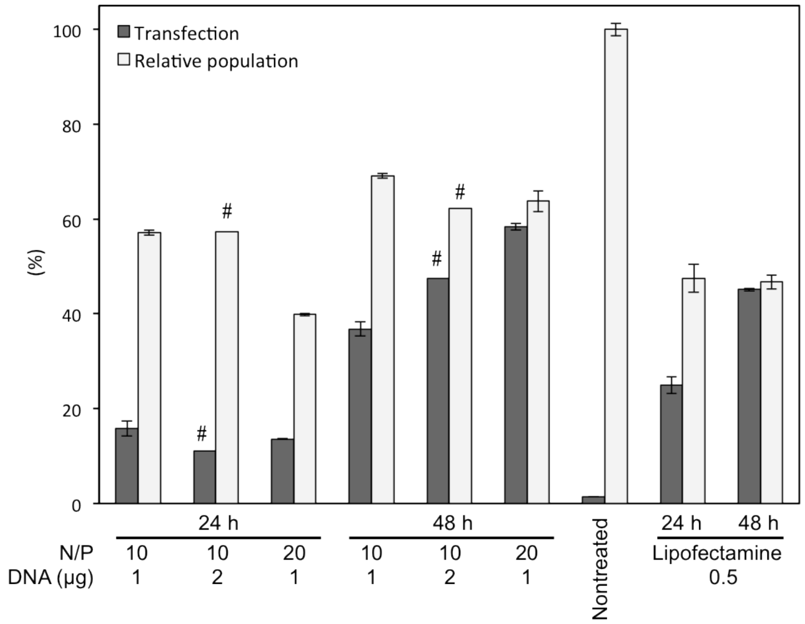

Figure 47. Flow cytometry transfection efficiencies and relative populations of GFP-transfected U87 cells using pDNA-loaded K10gA nanoparticles. Populations were gated according to a nontreated control. Each data point represents the average ±SD of two individual experiment comprising 10^4 cells. # 1×10^4 cells.

The transfection efficiencies are very promising for both, AcK6gA and K10gA nanoparticles; however, limited compatibility with cells, probably due to positive surface charges, demand for further improvement of the present system. pDNA-loaded H3SSgT nanoparticles revealed lower transfection efficiencies, but showed higher relative populations compared to the polylysine-based nanoparticles. These results are in agreement with reversed proportionality of transfection efficiency and toxicity/noncompatibility observed for AcK6gA and K10gA nanoparticles. The obtained transfection efficacies reflect not only the potential of such nanoparticles as gene delivery vectors, but also underline the importance of fine-tuning the molecular design to avoid toxic effects. Further investigations are needed to find optimal conditions for purely peptidic gene transfection based on amphiphilic peptides comprising polylysine or polyhistidine combined with a gramicidin A derived sequence.

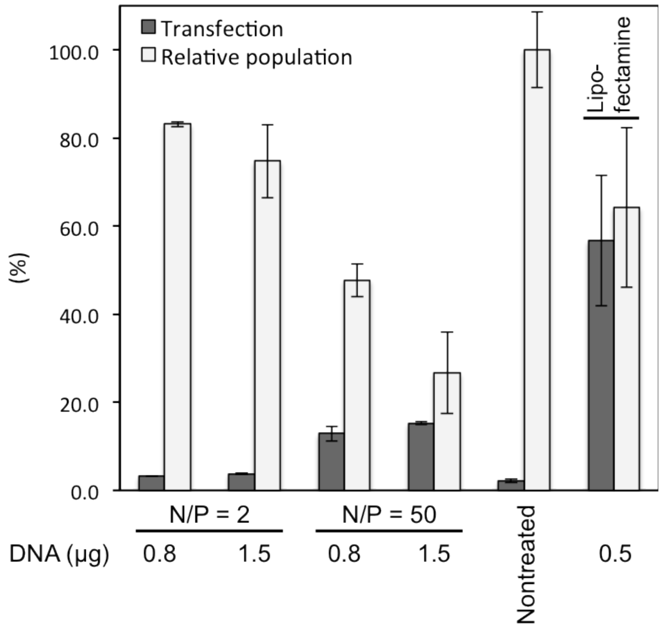

Figure 48. Flow cytometry transfection efficiencies and relative populations of GFP-transfected U87 cells using pDNA-loaded H3SSgT nanoparticles Populations were gated according to a nontreated control. Each data point represents the average ±SD of two individual experiment comprising 10^4 cells.

GFP fluorescence of transfected cells was visualized using CLSM. The intense fluorescence signal for both constructs, AcK6gA (Figure 49C) and K10gA (Figure 49D), comparable to the positive control (Lipofectamine; Figure 49B) confirm the functionality of the present system. However, for all samples, including the positive control, a corny round shape of the cells was observed (Figure 49). This can be assigned to apoptotic cells and is in agreement with the decreased relative populations obtained from flow cytometry analysis. Therefore, further investigations are required to fully understand the diverse influences of the N/P-ratio and the nature of the nanoparticles on cell viability and transfection capability.

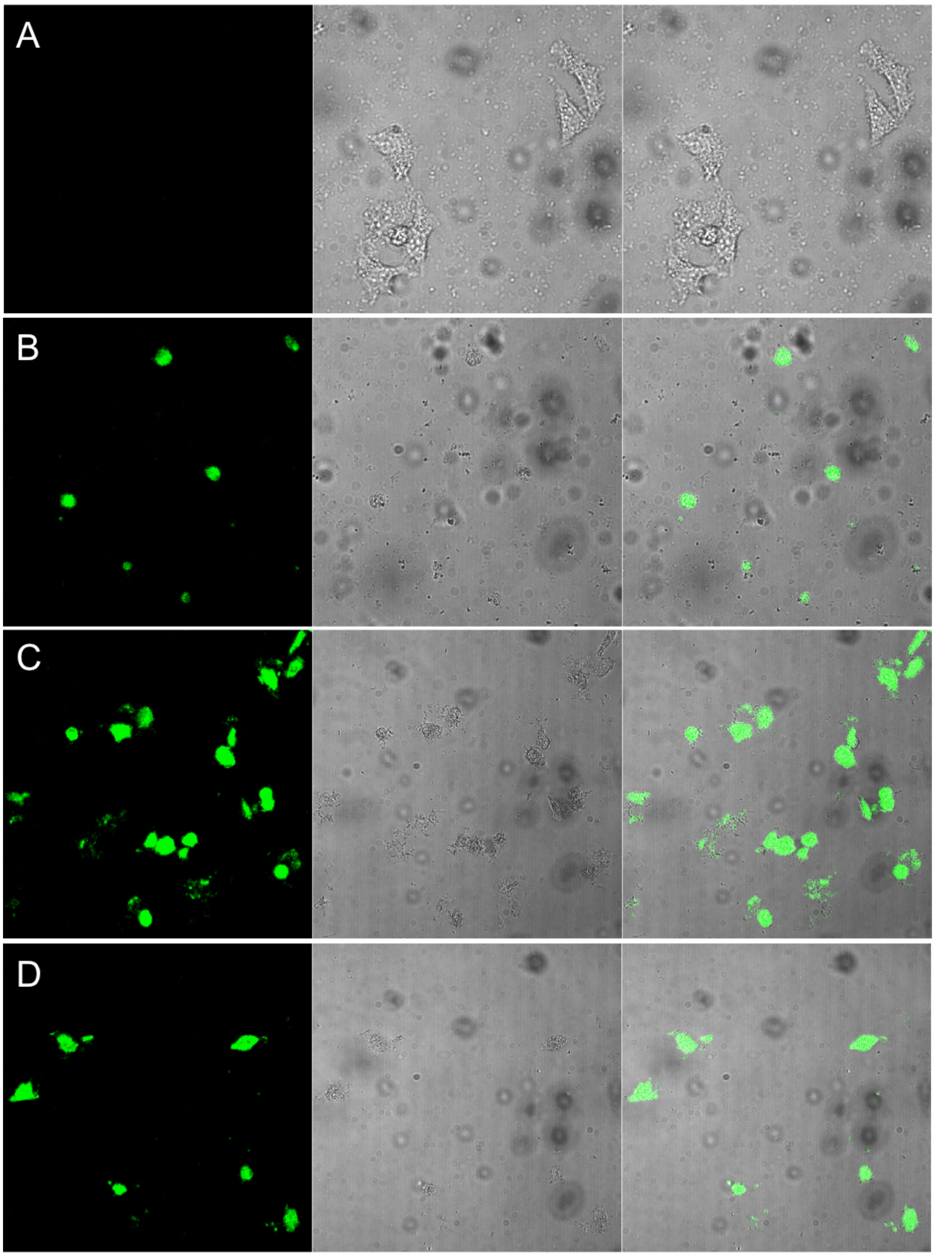

Figure 49. CLSM micrographs of GFP-transfected U87 cells. GFP emission (left), transmission (middle), and merge (right). Nontreated (negative control) (A), treated with Lipofectamine (positive control) (B), treated with pDNA-loaded AcK6gA nanoparticles (C), and treated with pDNA-loaded K10gA nanoparticles (D).

4.3.5 Toxicity Studies

To further investigate toxic effects of the created gene transfection agents MTS- and propidium iodide-assays were performed, in order to compare the results with relative populations obtained from transfection experiments (Transfection Section). MTS-assays of H3SSgT nanoparticles did not show any toxic effects even when applied alone (nonloaded nanoparticles; Figure 34, Chapter 3). Here, viabilities were evaluated for H3SSgT nanoparticles loaded with pDNA at N/P-ratios of 10 and 30. None of the tested concentrations in the range of 5–50 µg/mL showed toxic effects (Figure 50A). Furthermore, AcK6gA and K10gA nanoparticles were assessed at an N/P-ratio of 5. The cell viability was not altered in the tested range of 5–50 µg/mL (Figure 50B). In addition to MTS-assays, AcK6gA and K10gA were examined at three different N/P-ratios using a Hoechst 33342–propidium iodide assay, analyzed by flow cytometry to obtain the population of nonapoptotic cells. For both peptides lower N/P-ratios of 1 and 2 did not show apoptotic effects. In contrast, nanoparticles with an N/P-ratio of 10 revealed increased apoptosis for both, K10gA (62 % nonapoptotic cells) and AcK6gA (32 % nonapoptotic cells) (Figure 50C). These values match the results from flow cytometry analysis (Transfection Section) and qualitative observations using CLSM. Nontreated controls revealed a nonapoptotic population of 81 % and Lipofectamine showed 63 % nonapoptotic cells. The disagreement of the MTS-assays with other techniques used to determine compatibility with cells demonstrates that individual experimental setups can significantly influence the results. In addition, the method related quantification procedures possibly favor certain results by e.g. excluding apoptotic cells. As indicated in Figure 49 the cells were able to produce GFP but revealed a corny apoptotic shape. Similarly, the metabolic activity might be still intact to convert the tetrazolium componds of the MTS-assay to formazan products, thereby reporting viable cells. However, toxicity is a frequently appearing problem in the development of gene delivery agents due to the nucleic acid condensing mechanism, requiring multiply charged carriers for achieving acceptable loading efficiency. Optimizing the developed system by reducing surface charges and fine-tuning peptide sequences potentially eliminate toxic effects of these nanoparticles and lead to a gene delivery system with high efficacy.

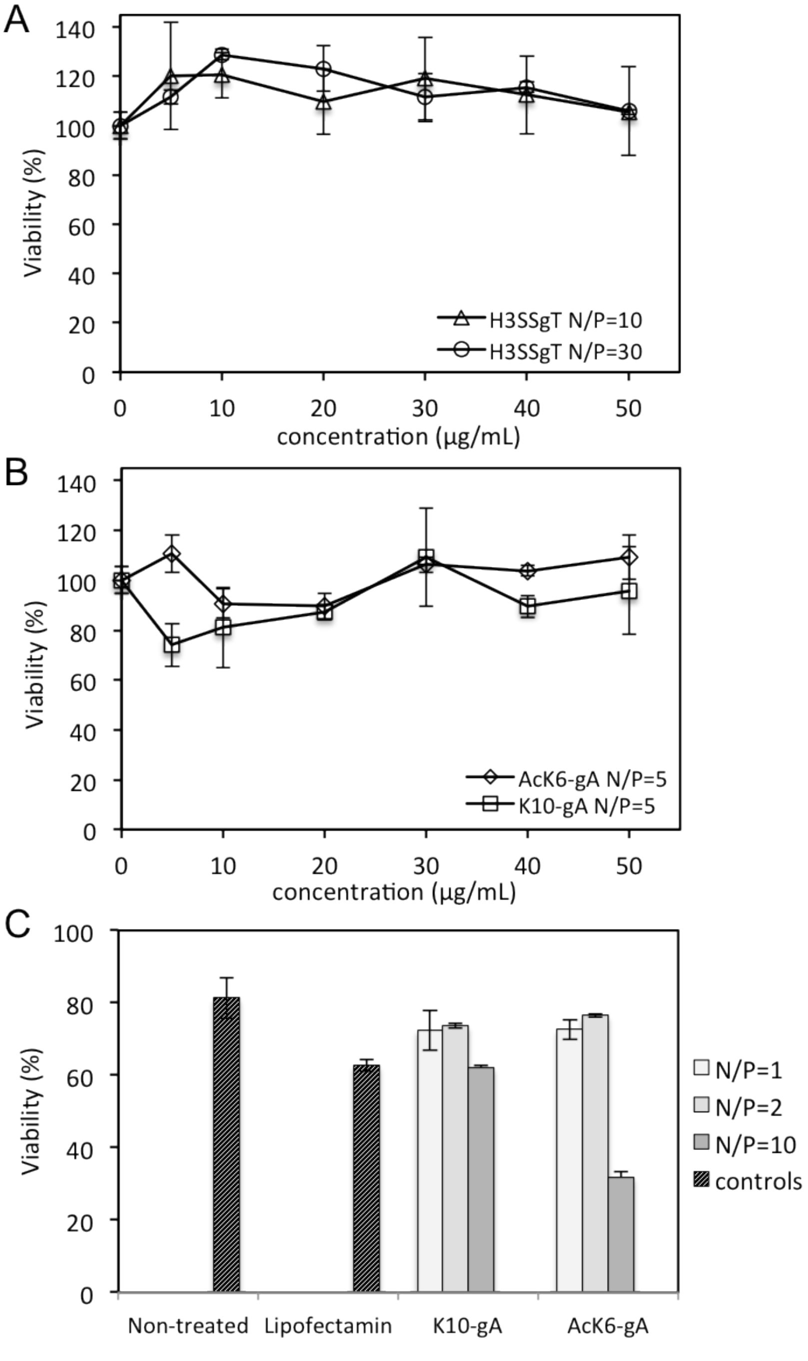

Figure 50. Viability of U87 cells treated with pDNA-loaded H3SSgT, AcK6gA, and K10gA nanoparticles. MTS assay of pDNA-loaded H3SSgT (N/P=10 and 30) (A) and AcK6gA and K10gA nanoparticles (N/P=5) (B). Hoechst 33342–propidium iodide assay of pDNA-loaded K10gA and AcK6gA nanoparticles at N/P-ratios of 1, 2, and 10 (C). Data represent average ± SD (n=3).

4.4 Conclusion

The growing demand for nonviral gene delivery carriers requires smart nanoengineering of polycations. In the present study, novel vectors for pDNA delivery were developed and assessed on transfection efficiency and toxicity using GFP-encoding pDNA as a reporter gene. The carriers are based on a rational design of amphiphilic peptides to form nanoparticles after condensation of pDNA via electrostatic interactions. Peptide sequences were constructed from hydrophobic sequences derived from gramicidin A and combined with polylysine or polyhistidine that served as the condensing moieties. Three sequences were investigated: AcK6gA, K10gA, and H3SSgT. All peptides were capable of completely condensing pDNA at N/P-ratios of 2–10 forming particles with diameters of 40–60 nm. The slightly positive surface charge promote cellular uptake, and in case of H3SSgT endosomal escape is potentially supported by the histidines, which can buffer the proton sponge effect. pDNA-loaded H3SSgT nanoparticles revealed partial release of pDNA upon addition of reducing agent in a slow manner, possibly hindered by the size of the plasmid and the resulting entangled nanoparticle architecture. Nanoparticles assembled from lysine-based peptides revealed promising transfection efficiencies up to about 60 %, slightly higher compared to Lipofectamine (~ 50 %). Using pDNA-loaded H3SSgT nanoparticles a transfection efficiency of 15 % was achieved while preserving high relative population of gated cells referenced to nontreated cells. However, increasing positive surface charge simultaneously induced cytotoxicity, resulting in a reversed proportionality of transfection efficiency and toxicity. This is a widely reported phenomenon, challenging the development of efficient transfection agents and requiring a very careful adjustment of each individual gene delivery system. Further optimization of the presented peptide nanoparticles is necessary to eliminate toxicity while preserving transfection ability.

Chapter 5

5 Nanoparticle-Based Highly Sensitive MRI Contrast Agents with Enhanced Relaxivity in Reductive Milieu

In this chapter, a highly sensitive, reduction-responsive MRI contrast agent is described. The contrast agent is coassembled from gadolinium-complexed heparin-PDMS and reduction-sensitive peptides, forming nanoparticles. Relaxivities are assessed by a human clinical MRI scanner and compared to a commercial contrast agent.

This chapter was submitted for publication:
Sigg, S. J.; Santini, F.; Najer, A.; Richard, P. U.; Meier, W.; Palivan, C. G. Nanoparticle-Based Highly Sensitive MRI Contrast Agents with Enhanced Relaxivity in Reductive Milieu. **2016**, submitted.

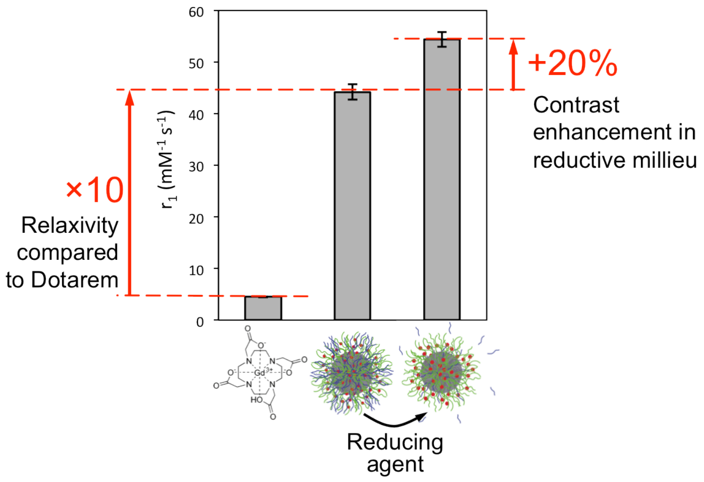

Figure 51. Coassemblies of gadolinium-complexed heparin-PDMS and a reduction-responsive peptide revealing high contrast in MRI. In reductive milieu the coassembled peptide is degraded that further increases contrast due to increased accessibility of water to the metal centers.

5.1 Abstract

Current magnetic resonance imaging (MRI) contrast agents often do not provide sufficient contrast for diagnosing early disease stages due to relatively low contrast efficacy. Additionally, sensing of biochemical environments by MRI probes is desirable to increase contrast even further. Here, we report a highly sensitive nanoparticle-based MRI probe with r_1 relaxivity up to 51.7 ± 1.2 $mM^{-1}s^{-1}$. The nanoparticles with diameters of about 45 nm were self-assembled from gadolinium-complexed heparin-poly(dimethylsiloxane) copolymer. Responsiveness to reductive environments was additionally introduced by incorporation of a reduction-sensitive amphiphilic peptide to the previous nanoparticle architecture. The loss of peptide components within a reductive milieu leads to an r_1 relaxivity increase, therefore creating a higher contrast in MRI. This nanoparticle-based MRI probe is further characterized by low cellular uptake (max. 5.4 %), no apparent cellular toxicity (tested up to 1 mM Gd^{3+}), absence of anticoagulation property (below detection limit), and high shelf stability (no increase in free Gd^{3+} over 7 months). In combination with the enhanced permeability and retention effect (EPR-effect), which is expected for nanoparticles with sizes around 50 nm, this highly sensitive MRI contrast agent serves as a promising probe for early diagnosis of cancer through possible accumulation and contrast enhancement within reductive extracellular tumor tissue.

5.2 Introduction

Magnetic resonance imaging (MRI) is a noninvasive technique widely used in diagnostics such as cardiovascular, neurological, and oncological imaging.[166] It relies on the manipulation of the nuclear spin of water protons by an external magnetic field to obtain an image. Contrast is generated by tissue-dependent variations in the longitudinal (T_1) and transverse (T_2) relaxation times of the proton nuclear spin. In order to induce additional contrast, chemical MRI contrast agents (CAs) are widely used. These are paramagnetic species that shorten T_1 and T_2 of the surrounding water protons. When the induced decrease in T_1 and T_2 is roughly the same, they are called positive CAs, in case T_2 is altered to much higher extend, they are called negative CAs.[265] Positive CAs are predominantly built from gadolinium ions (Gd^{3+}). Gadolinium increases the signal by decreasing the T_1 relaxation time of water in its close proximity. The capacity of a CA is usually described by its relaxivity (r), which is the change in relaxation rate ($\Delta(1/T_i)$) normalized to the molar gadolinium concentration ([Gd]) (Equation 1).[265]

$$r = \frac{\Delta(1/T)}{[Gd]} \tag{6}$$

However, the toxicity of free gadolinium requires it to be administered as a chelate, which in turns decreases the number of coordination sites available to water molecules, thus limiting the contrast enhancement. To date, nine gadolinium-based CAs are approved for clinical use,[152] typically revealing an r_1 of about 4–5 $mM^{-1}s^{-1}$.[151] Gadolinium-based CAs are small molecules, which passively distribute after their administration to patients.[158] The contrast enhancement achievable through the use of commercially available Gd-CAs is limited by their low efficiency, demanding for high doses.[151,266] To increase contrast enhancement of MRI CAs three main strategies are followed: modifying the chelator to increase free coordination sites at the metal center and thus exchange rates between bulk water and coordinated water; increasing concentration of gadolinium by accumulating multiple chelators within one molecule; and the formation of bulky assemblies to lower molecular tumbling (τ_R) as both, high water exchange rates and decreased molecular tumbling contribute to faster relaxation and higher contrast.[166] In this regard, nanosized macromolecular MRI probes of various architectures were reported, comprising micelles,[267,268] dendrimers,[269,270] vesicles,[271-273] and nanoparticles.[166,274,275] These exhibit higher relaxivities and allow for the introduction of stimuli responsiveness or combination with drug delivery for theragnostic approaches.[276]

Introducing specificity and responsiveness of the MRI CAs to distinct body environments, such as inflamed tissue or tumor microenvironments, allow for specific localization of pathogenic regions and diagnosis.[166,277] Therefore, individual gadolinium chelates were conjugated to build larger structures bearing high numbers of gadolinium-chelates, simultaneously decreasing τ_R due to their size and rigidity. Both characteristics, high water exchange rates at the metal center and decreased molecular tumbling are contributing to fast relaxation of coordinating water molecules, creating higher contrast in MRI.[166]

However, moderate contrast enhancement and/or lacking responsiveness to specific triggers were main drawbacks encountered with these novel designs.[166] CAs able to respond to environmental characteristics of tissue, such as pH and redox potential, were developed in the past decade.[278] Recent reports describe polymer shielded gadolinium oxide nanoparticles revealing an r_1 of around 6.5 $mM^{-1}s^{-1}$ after release of the polymer at acidic pH due to an increase in water exchange rate, compared to 0.7 $mM^{-1}s^{-1}$ at neutral pH.[279] Using the same principle, reducible cyclodextrin nanocapsules were constructed to entrap gadolinium-chelates. Reductive release of the chelates increased tumbling as the dominant factor, thus decreasing r_1 from 15.2 $mM^{-1}s^{-1}$ to 8.2 $mM^{-1}s^{-1}$.[280] Another approach describes the activation of gadolinium-chelate monomers to polymerize and self-assemble when adding reducing agent, what increased r_1 from 3.9 $mM^{-1}s^{-1}$ to 8.3 $mM^{-1}s^{-1}$.[281] These values are comparably small in regard of theoretically possible relaxivities[151] and are in the range of commercially available contrast agents (~ 4–5 $mM^{-1}s^{-1}$).[151] CAs combining high r_1 relaxivity and responsiveness to physiological parameters at pathologic sites remains a major challenge.

In this respect, our aim herein is to develop a highly active and reduction-sensitive MRI contrast agent. Trivalent lanthanides, including gadolinium, were reported to have high affinity toward the glycosaminoglycans (GAGs) heparin[282,283] and hyaluronan (HA).[284] In addition, transchelation of gadolinium from FDA-approved, linear contrast agents to heparin was observed, indicating strong complexing abilities of this particular GAG.[285] Furthermore, heparin is a possible candidate to be exposed on nanoparticles for prolonged circulation time within the blood stream.[286,287] This allows using reduced doses of MRI CAs and efficient vasculature imaging at longer time scales.[274,276] Long-circulating nanoparticles can readily accumulate in tumor tissue via the leaky vasculature surrounding tumors (EPR-effect),[288,289] which increases efficacy of cancer imaging.[290,291] The elevated GSH-levels in the extracellular environment of tumors, compared to nonmalignant cell, can be chosen as trigger to increase image contrast.[292,293]

Therefore, we designed and synthesized an amphiphilic heparin-poly(dimethylsiloxane) (hepPDMS) block copolymer being capable of self-assembling into nanoparticles and offering complexation sites for gadolinium. In order to implement responsiveness towards environments with increased reducing properties, a disulfide linked amphiphilic peptide was synthesized via SPPS on a Rink amide resin. This peptide was then coassembled with previously complexed hepPDMS-Gd copolymer to obtain a reduction-sensitive MRI CA. The peptide sequence bears a reducible linker connecting the hydrophobic L-tryptophan-D-leucine repeating unit and the oligohistidine (H3SSgT) as reported in Chapter 3. The amphiphilic peptide was designed to interact with hepPDMS-Gd via the polyhistidine sequence to coassemble into peptide-hepPDMS-Gd nanoparticles (p-hepPDMS-Gd-NPs). This novel approach using natural chelators for developing a highly sensitive nanoparticulate MRI CA and additionally implement sensitivity to reducing environments via coassembly with a peptidic component offers a promising direction for future optimization and application of these nanoparticles.

5.3 Results and Discussion

5.3.1 Gadolinium Complexation, Nanoparticle Formation, and Characterization

Inspired by the strong Gd^{3+} complexing ability of the natural GAG heparin[282,285] and the long blood circulation behavior of heparinized nanoparticles[286,287] we designed a heparin-based nanoparticle system intended for highly sensitive MRI contrast enhancement. We synthesized an amphiphilic heparin-poly(dimethylsiloxane) (hepPDMS) copolymer, which self-assembles into nanoparticles under aqueous conditions.[294] HepPDMS was obtained by coupling commercial heparin polysaccharide with commercial PDMS (5 kDa) via reductive amination, which typically yielded 25 heparin repeating units per PDMS chain (5 kDa), as previously reported.[294] HepPDMS nanoparticles (hepPDMS-NPs) were subsequently formed by the solvent exchange method, starting from 50% ethanol to water via dialysis. Similarly to previously reported self-assemblies formed by hepPDMS in PBS,[294,295] the obtained assemblies revealed a small spherical nanoparticle morphology (transmission electron microscopy (TEM), 19 ± 3 nm, and dynamic light scattering (DLS), 44 ± 16 nm) (Figure 61A,B (Supporting Information)). The observed size difference between TEM and DLS can be attributed to the drying effect in TEM. The accessibility of heparin on the surface of the NPs was quantified by the Farndale microassay giving a concentration of accessible heparin of 1170 ± 42 µg/mL for nanoparticles built from an initial hepPDMS concentration of 4.25 mg/mL.

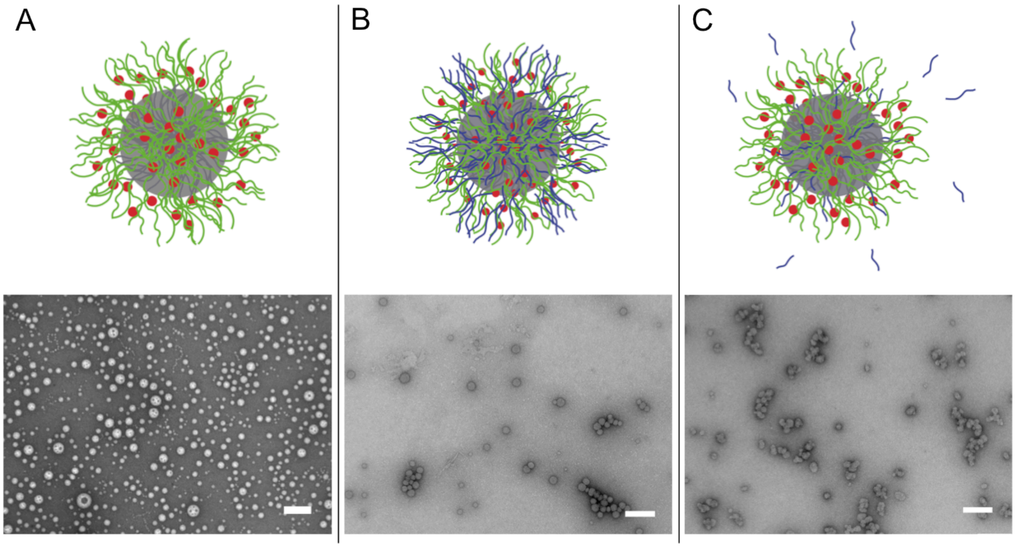

Figure 52. Schematic representation and TEM micrographs of hepPDMS-Gd-NPs (A), p-hepPDMS-Gd-NPs before (B), and after (C) addition of DTT. Scale bars: 200 nm.

To create a nanoparticle-based gadolinium MRI CA, hepPDMS was incubated with a solution of $GdCl_3$ (6.5 eq.) in 50% ethanol at pH 7.0 in order to complex Gd to the heparin block of the copolymer, which comprises highly negative charged trisulfated disaccharide repeating units, reported to possess high affinity to lanthanides.[282,283] Nanoparticles were obtained as described above, whereas non-complexed gadolinium was simultaneously removed during the dialysis step, yielding hepPDMS-Gd nanoparticles (hepPDMS-Gd-NPs). DLS and TEM measurements showed particles sizes of 51 ± 22 nm and 45 ± 16 nm (Figure 60 (Supporting Information) and Figure 52A), respectively. The shift in size compared to hepPDMS-NPs (Figure 61A,B (Supporting Information)) can be attributed to decreased surface charges lowering the repulsive force between molecules, thus allowing a more dense structure. Successful complexation of gadolinium to the heparin-block of hepPDMS-NPs was shown by Fourier transform infrared spectroscopy (FTIR). A frequency shift to lower values as well as peak line shape broadening is expected in FTIR when metals have bound to the heparin block.[296]

FTIR showed the O-H stretching at 3440 cm^{-1}, C=O stretching vibrations at 1626 cm^{-1}, N–H bending at 1410 cm^{-1}, and symmetrical (1240 cm^{-1}) and asymmetrical (1043 cm^{-1}) stretching of the S=O bond ($NH–SO_3–$ and $CH_2–SO_3–$)[297] of heparin for hepPDMS-NPs (Figure 53A). The slightly decreased frequencies for these functional groups, when complexed with gadolinium (hepPDMS-Gd), as well as broadening of the peaks indicated interaction of gadolinium to the heparin of hepPDMS. The absorption at 1100 cm^{-1} is the asymmetric and symmetric stretching of two siloxane bonds of the PDMS block, which remained the same after complexation with gadolinium. The signal at 800 cm^{-1} is the out-of-plane and at 1259 cm^{-1} the in-plane bending or scissoring vibrations of $Si–CH_3$ of the PDMS block (Figure 53A).[298] This confirms that no interaction occurred between the hydrophobic block of the copolymer and gadolinium, as expected.

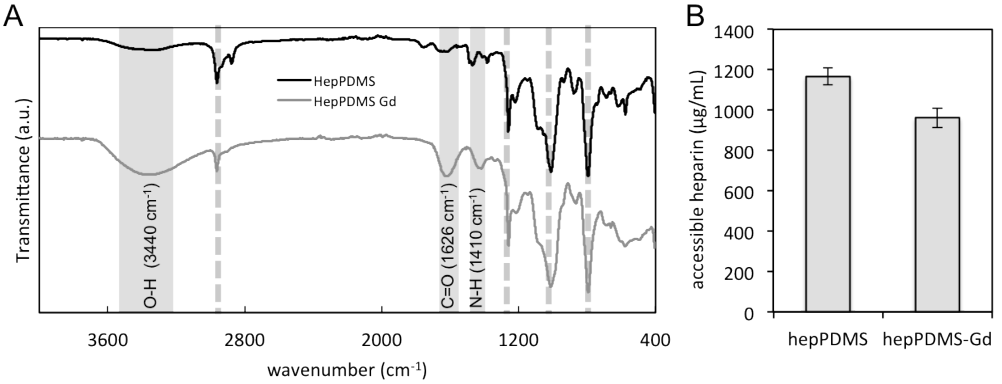

Figure 53. FTIR spectra of hepPDMS-NPs and hepPDMS-Gd-NPs (A). Grey dashed lines are the PDMS absorptions; grey regions indicate the gadolinium interaction to the heparin block. Surface accessible heparin as measured by Farndale microassay (B). Data represent average ± SD (n=3).

Complexation of gadolinium to the heparin block of hepPDMS was further confirmed by a Farndale microassay that showed significant decrease of accessible heparin chains on nanoparticles from 1170 ± 42 µg/mL (hepPDMS-NPs) to 960 ± 49 µg/mL (hepPDMS-Gd-NPs) due to partial occupation of the dye-binding sites on heparin by Gd^{3+} (Figure 53B). The concentration of gadolinium complexed within the hepPDMS-NPs was determined to be 0.93 mM by inductively coupled plasma optical emission spectroscopy (ICP-OES), which is 77 % of the initial gadolinium concentration. It demonstrates the high complexing abilities of hepPDMS and allows for creation of a high gadolinium-density within the nanoparticles, necessary for contrast enhancement in MRI.

In order to introduce additional reduction-sensitivity to our nanoparticle-based MRI CA the reduction-responsive amphiphilic peptide H3SSgT (0.5 mg/mL) was coassembled with previously complexed hepPDMS-Gd to yield p-hepPDMS-Gd-NPs. The formed nanoparticles were similar in size (TEM: 43 ± 10 nm; DLS: 57 ± 38 nm) and shape compared to hepPDMS-Gd-NPs (Figure 60 (Supporting Information) and Figure 52B). They are around four fold smaller compared to particles assembled from peptide (H3SSgT) alone (190 nm; Chapter 3), indicating that the obtained nanoparticles were coassembled from both hepPDMS-Gd and H3SSgT. A negligible population of larger intensity weighted diameters (>300 nm) was also observed and can be attributed to purely peptidic nanoparticles. Using higher concentrations of peptide (2 mg/mL) induced formation of large aggregates coexisting beside the coassemblies (Figure 61C,D). Therefore, further characterization of coassemblies was conducted using the lower peptide concentration (0.5 mg/mL).

Energy dispersive X-ray spectroscopy (EDX) analysis showed colocalization of gadolinium and sulfur (from the disulfide in the peptide and from hepPDMS) within the particles (Figure 54). The expected interaction of histidine residues of the peptide with the heparin block of hepPDMS when coassembled was analyzed using Farndale microassays. The coassembled peptide decreased the accessibility of heparin from 1020 ± 82 μg/mL to 760 ± 85 μg/mL heparin. Since the assay monitors the accessible heparin, the cationic dyes used in the assay need to align on heparin to produce a signal, the values represent the situation on the surface of the nanoparticles rather than in their core. Thus, it also demonstrates the steric hindrance originating from the coassembled peptides. Zeta potential measurements revealed slightly different values of −55.0 ± 0.5 mV for p-hepPDMS-Gd-NPs compared to NPs assembled without peptide −58.0 ± 0.3 mV (hepPDMS-Gd-NPs). However, the changes in zeta potential are rather small emerging from the fact that heparin is the most negatively charged biological macromolecule.[299] At H3SSgT/hepPDMS-Gd ratios suitable for coassembly the amount of histidines is not sufficient to neutralize the charge of heparin, resulting highly negatively charged NPs. The preservation of heparin-characteristic on the nanoparticle surfaces after Gd-complexation and self-assembly provides the desired properties for potential prolonged blood circulation time,[286,287] required for accumulation in tumor regions via the EPR-effect and subsequent contrast enhancement for MRI diagnostics.[290,291]

To characterize size and morphology changes of p-hepPDMS-Gd-NPs upon reductive stimuli, they were treated with 10 mM dithiothreitol (DTT) in HEPES buffer at pH 7.2 resulting in slightly decreased diameters of 41 nm ± 8 nm by TEM and 44 ± 19 nm by DLS, as compared to hepPDMS-Gd-NPs (Figure 60 (Supporting Information) and Figure 52C).

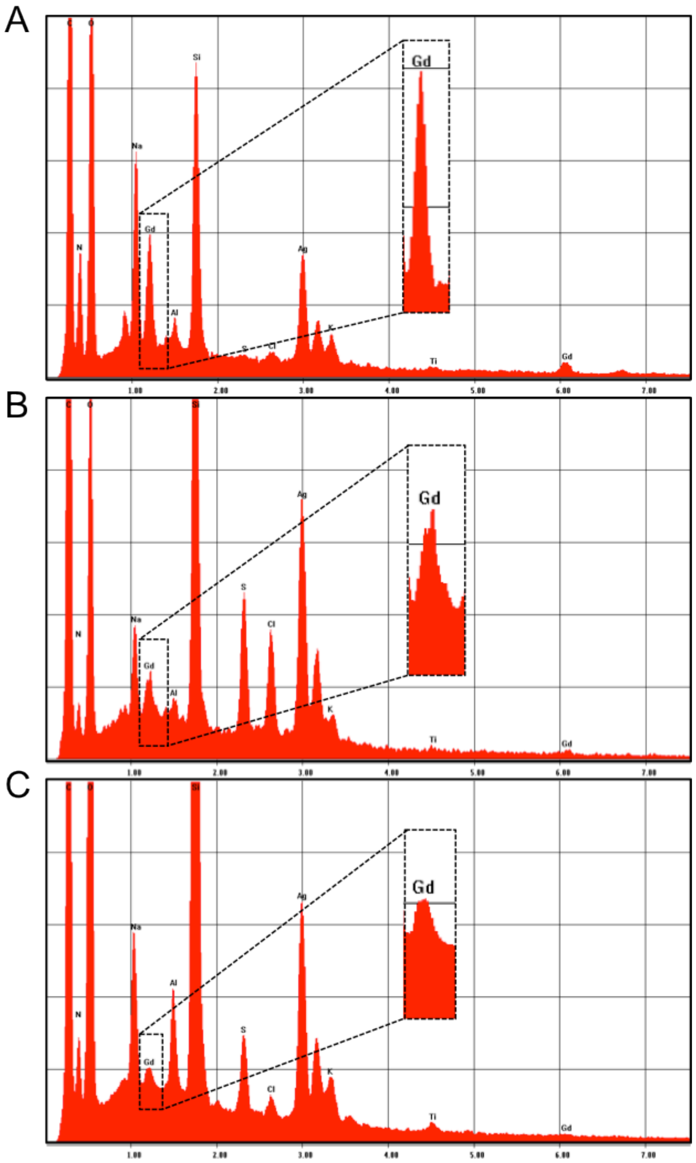

Figure 54. EDX-spectra of Gd-DOTA (A), hepPDMS-Gd-NPs (B), and p-hepPDMS-Gd-NPs (C).

5.3.2 MRI-Analysis

The suitability of these Gd^{3+}-complexed nanoparticles for decreasing the T_1 relaxation time of surrounding water, thus increasing r_1 for better MRI contrast, was investigated on a 3 T human clinical MRI scanner. As a reference we tested commercial gadolinium–1,4,7,10-tetraazacyclododecane-1,4,7,10-tetraacetic acid (Gd-DOTA), which is one of the most frequently applied clinical MRI CA. Gd-DOTA revealed T_1 relaxation times in a range of 1360 ms at 0.10 mM gadolinium and 213 ms at 0.99 mM gadolinium (Figure 55, Table 6

(Supporting Information)), resulting in an r_1 of 4.5 ± 0.1 $mM^{-1}s^{-1}$ (Figure 56), which is in agreement with literature values.[150] When gadolinium was complexed within hepPDMS nanoparticles the water relaxation time was tremendously decreased ranging from 164 ms at 0.093 mM to 20.2 ms at 0.93 mM. This resulted in an r_1 value of 51.7 ± 1.2 $mM^{-1}s^{-1}$, which is more than an order of magnitude higher than for clinically used Gd-DOTA. This can be attributed to the different binding mode of gadolinium to heparin compared to the cyclic DOTA, creating faster exchange rates at the metal centers and decreased tumbling due to the size of the nanoparticles.

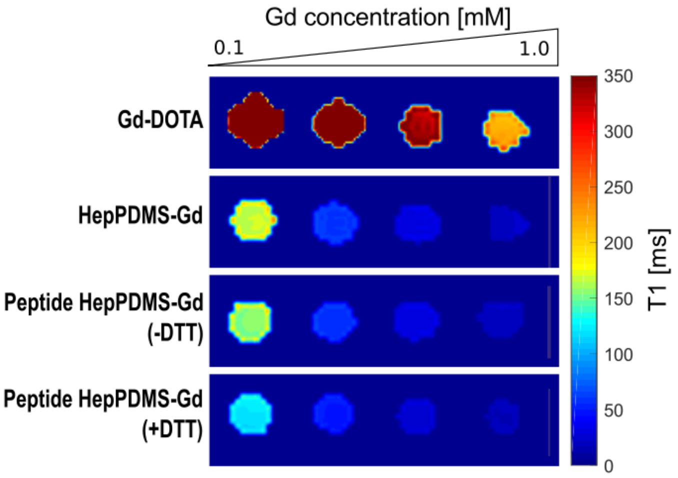

Figure 55. T_1 weighted MR image of Gd.DOTA, hepPDMS-Gd-NPs, p-hepPDMS-Gd-NPs (–DTT), and p-hepPDMS-Gd-NPs (+DTT), recorded on a 3 T human MRI scanner. Detailed gadolinium concentrations of the different nanoparticles are summarized in Table 6 (Supporting Information).

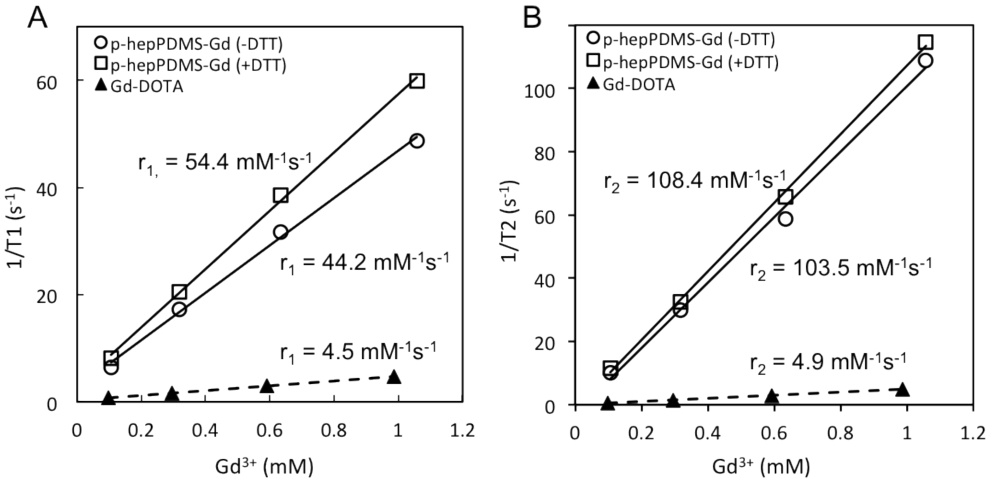

Figure 56. $1/T_1$ curves (A) and $1/T_2$ curves (B) of p-hepPDMS-Gd (–DTT), p-hepPDMS-Gd (+DTT), and Gd-DOTA. Slopes provided the r_1 and r_2 as indicated.

When coassembled with the reduction-responsive H3SSgT, p-hepPDMS-Gd-NPs revealed higher T_1 values ranging from 154 ms at 0.11 mM gadolinium to 20.8 ms at 1.10 mM gadolinium (Figure 55, Table 6 (Supporting Information)), resulting in a decreased r_1 of $44.2 \pm 1.5\ mM^{-1}s^{-1}$ compared to purely hepPDMS-Gd-based nanoparticles. This can be associated with increased density within the coassembled particles due to close arrangement of the peptidic histidines to the heparin block of the copolymer, thereby sterically hindering water to access and coordinate to the metal centers, which decreases relaxivitiy. After treatment with reducing agent (DTT) the T_1 relaxation times significantly changed back towards lower values ranging from 124 ms at 0.11 mM gadolinium to 16.7 ms at 1.06 mM gadolinium (Figure 55, Table 6 (Supporting Information)). Releasing the coassembled peptide by reduction revealed an increase in r_1 of about 20% to $54.4 \pm 1.5\ mM^{-1}s^{-1}$ (Figure 56), which is again close to the value of NPs assembled from hepPDMS-Gd alone. This increase in relaxivity observed in reductive environment can be used to obtain increased contrast for cancerous tissue based on the elevated GSH-levels in extracellular space of tumors.[292,293] The slight difference compared to hepPDMS-Gd-NPs can be explained by the lack of a highly ordered assembly due to the degradation and dissociation of one assembly partner. Analysis of T_2 relaxation rates revealed similar tendencies, when compared to Gd-DOTA. For hepPDMS-Gd-NPs a transverse relaxation rate, r_2, of $162.6 \pm 17.8\ mM^{-1}s^{-1}$ was obtained. For particles coassembled with H3SSgT, r_2 was determined to be $103.5 \pm 5.0\ mM^{-1}s^{-1}$ and $108.4 \pm 2.5\ mM^{-1}s^{-1}$ after DTT-treatment. These values are, similar to the increase in r_1, more than one order of magnitude higher, compared to Gd-DOTA ($4.90 \pm 0.03\ mM^{-1}s^{-1}$).

5.3.3 EPR-Analysis

In order to further characterize the ability of the created contrast agent to decrease T_1 and T_2 as demonstrated by MRI analysis, we performed EPR measurements to obtain the transverse electronic relaxation time (T_{2e}), which is expected to reveal lower values for gadolinium-complexed nanoparticles compared to Gd-DOTA. Gadolinium has an $^8S_{7/2}$ single ion ground state and a nuclear spin value of 1/2. The spin Hamiltonian of the Gd^{3+} ion is based on the Zeeman electronic interaction and the zero-field interaction:

$$\mathcal{H} = g\beta BS + D\left[S_Z^2 - \frac{1}{3}S(S+1) + E(S_X^2 - S_Y^2)\right] \tag{7}$$

where g is the gyromagnetic factor of the S-state, D and E are the zero-field splitting (ZFS) parameters.[300] If the system is characterized by a strong Zeeman interaction, significantly higher than the crystal field, the EPR spectrum appears as a single very broad line with a g-factor of around 2.00. In the opposite situation in which the crystal field is strong, the EPR spectrum is complex with additional lines appearing both with g-values significantly higher than 2 and lower than 2. In the case of Gd-complexed nanoparticles (hepPDMS-Gd-NPs and p-hepPDMS-Gd-NPs) and Gd-DOTA the EPR spectra at 298 K have gyromagnetic factors of around 2.00 within experimental errors (Table 7 (Supporting Information)), with no additional lines at higher or lower g-values (Figure 57). Compared with Gd-DOTA spectrum, the EPR spectra of coassemblies consist of very broad lines. They differ from Lorenzian lines, and might be described as a superposition of two lines with different intensity and peak-to-peak widths, as already reported for Gd-complexes in aqueous solution (Figure 57).[301] EPR line widths (ΔH_{pp}) allow the calculation of the transverse electronic relaxation rates, $1/T_{2e}$ using Equation 8:[302]

$$\frac{1}{T_{2e}} = \frac{g\mu_B \pi\sqrt{3}}{h}\Delta H_{pp} \tag{8}$$

Where μ_B is the Bohr magneton, and h the Plank constant. The more intense paramagnetic component has been taken into account when ΔH_{pp} have been calculated. The relaxation rate at a field of 0.34 T for Gd-DOTA was calculated as $1.31\times10^9\ s^{-1}$,[303] whilst the relaxation rates for hepPDMS-Gd-NPs, and p-hepPDMS-Gd-NPs were $6.56\times10^9\ s^{-1}$, and $5.98\times10^9\ s^{-1}$, respectively.

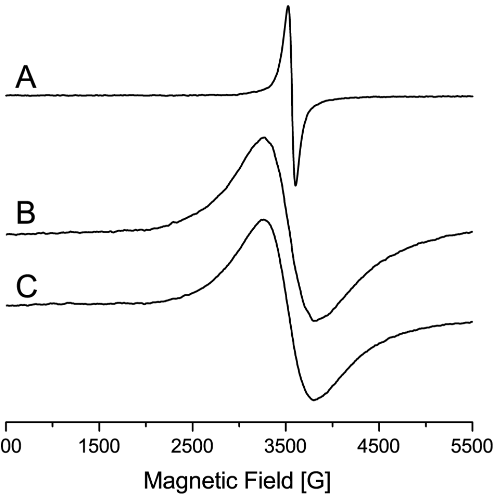

Figure 57. EPR spectra of Gd-DOTA (A), hep-PDMS-Gd-NP (B), and p-hep-PDMS-Gd-NP (C).

The significant difference between the transverse electron spin relaxation rate corresponding to Gd-DOTA and those of Gd-complexed NPs indicate that intramolecular dipole-dipole interactions between close Gd(III) ions in the case of Gd-complexed NPs induce the decrease of T_{2e},[304] in addition to a slower rotational correlation time due to the difference in their size. Our results are in agreement with previous reports indicating that the increased proton relaxivity was associated with the formation of rigid micelle-like structures in aqueous solution.[302] The slight difference in the transverse electron spin relaxation rate between hepPDMS-Gd-NPs and p-hepPDMS-Gd-NPs indicate an effect of the coassembled peptide, as it has been intended in order to decrease Gd accessibility. Given the lack of a reliable theory of electron spin relaxation for macromolecular Gd-systems, especially in a complex system as the Gd-complexed NPs we point out only in a qualitative manner that intramolecular dipole-dipole mechanism contributes to the electronic relaxation. D-values were estimated based on the ΔB values between the central line and the edge line of lower magnetic field in the EPR spectrum (the supposed position of this line to induce the significant broadening of the overall line), and using a formula valid in the first order of the perturbation theory: $D=\Delta B/6$. Electronic relaxation in Gd^{3+} complexes is generally explained in terms of a zero-field splitting interaction. However, due to the broad EPR overall shape, the ZFS tensors contribute only to enlargement of the EPR linewidth and therefore, a precise estimation was not possible (we restrict only to the estimation of ΔH_{pp}).

5.3.4 In Vitro Evaluation

The promising increase in relaxivity r_1 of hepPDMS-Gd-NPs, p-hepPDMS-Gd-NPs, and DTT-treated p-hepPDMS-Gd-NPs indicate their potential for high contrast in MRI. A first obstacle to address is nonspecific cellular toxicity. This was tested in cell viability studies using HeLa cells and various concentrations of p-hepPDMS-Gd-NPs, hepPDMS-Gd-NPs, and commercial Gd-DOTA. None of the particles revealed any cellular toxicity at the tested concentration range up to about 1.0 mM gadolinium (Figure 58A). The absence of cellular toxicity could be attributed to low cellular uptake based on the highly negative surface charge on our nanoparticles. This was tested by incubation of hepPDMS-Gd and p-hepPDMS-Gd nanoparticles with HeLa cells, subsequent washing, digestion and quantification of Gd content using ICP-OES. We found only marginal uptake of 2.8 and 5.4 %, respectively (Figure 58B). This is advantageous due to desired long-circulation time within the blood stream, for which low cellular uptake is needed, and subsequent fast removal from the body.

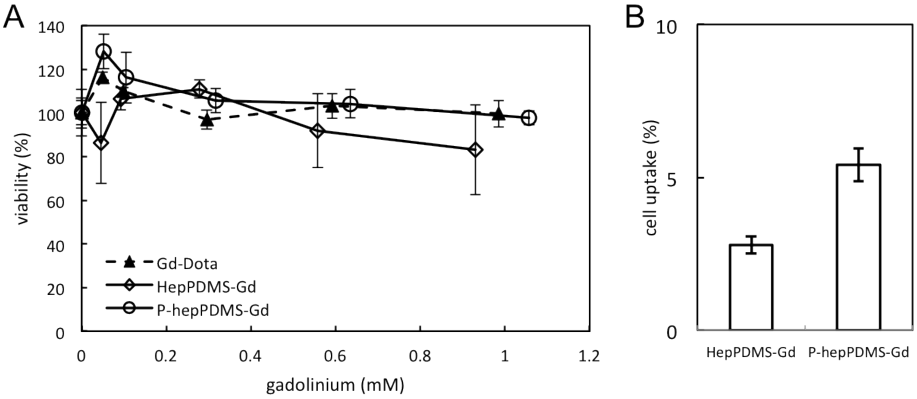

Figure 58. MTS viability assay of HepPDMS-Gd-NPs and p-hepPDMS-Gd-NPs compared to commercial contrast agent Gd-DOTA (A). Cell uptake of hepPDMS-Gd-NPs and p-HepPDMS-Gd-NPs (B). Data represent average ± SD (n=3) (A); average ± 10% deviation by ICP-OES (B).

Leakage of free gadolinium ions from the nanoparticles is associated with toxicity concerns and represents another hurdle for translation towards an *in vivo* applicable MRI CA. Free gadolinium ions in solution were quantified using a xylenol orange colorimetric assay. HepPDMS-Gd-NPs showed 8.5% free gadolinium relative to the total amount, whereas p-hepPDMS-Gd-NPs revealed 5.9% free gadolinium. After incubation for seven months at room temperature the level of free gadolinium was not elevated (8.3% and 5.6%, respectively); however, the nanoparticles partly rearranged to larger sizes, particularly for peptide coassemblies (Figure 59). This can be explained by slow sedimentation and subsequent aggregation of the nanoparticles. Stability of the nanoparticles was also investigated by incubation in cell growth media. The sensitivity of the assay was limited due to cross interaction of the colorimetric assay with the culture media. Nevertheless, the measured gadolinium levels remained below the detection limit of about 1 μM. This level can be seen as noncritical regarding the normally applied concentrations of 0.1–0.3 mmol/kg[305] for commercial MRI CAs with an r_1 of 4–5 $mM^{-1}s^{-1}$ and LD50 values for gadolinium of 0.5 mmol/kg in rats.[306]

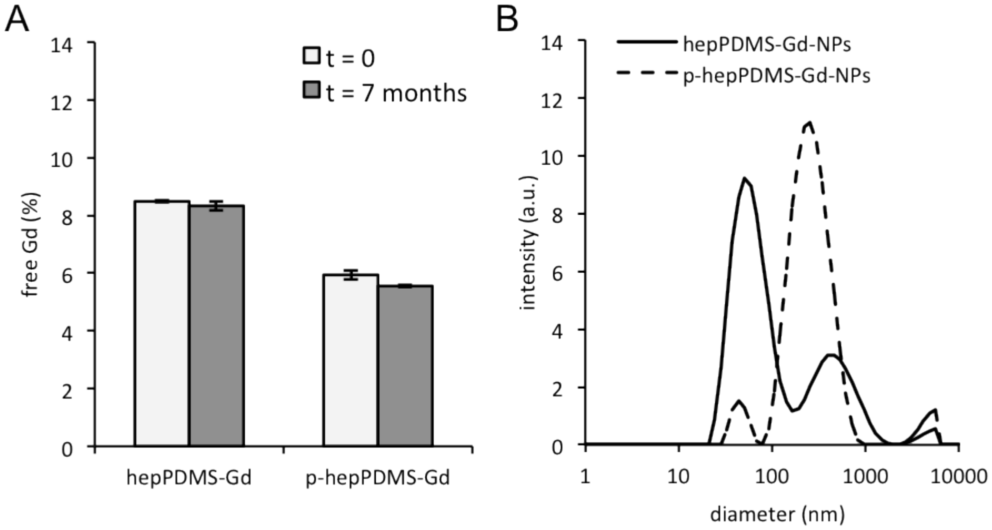

Figure 59. Free Gadolinium before and after incubation for 7 months at room temperature (A). Size distribution after incubation for 7 months (B).

The third obstacle for our nanoparticle system is the known anticoagulation property of heparin, which we want to avoid for MRI imaging applications. The anticoagulation activity was evaluated using standard anti-Xa assays. Anticoagulation activity was below the limit of detection of the assay (<0.1 U/mL) for hepPDMS-Gd-NPs and p-hepPDMS-Gd-NPs at concentrations of 700 and 580 μg/ml accessible heparin (=135 and 110 U/ml), respectively. This indicates that the anticoagulation ability of heparin was greatly reduced by conjugation to PDMS and subsequent nanoparticle formation. The specific pentasequence of heparin needed for anticoagulation activity might be mainly hidden within the self-assembled nanostructures. The developed reduction-sensitive constructs serve as a very promising candidate toward functional high-relaxivity MRI CAs.

5.4 Conclusion

Responsive high-relaxivity MRI contrast agents are highly demanded for clinical diagnostics. P-hepPDMS-Gd-NPs fulfill numerous key criteria for being used as responsive high-relaxivity CAs. The developed CAs coassembled from gadolinium-complexed hepPDMS and reduction-sensitive peptide H3SSgT, forming spherical nanoparticles with diameters of about 45 nm. These nanoparticles revealed an r_1 relaxivity of 44.2 $mM^{-1}s^{-1}$, that is tenfold higher compared to the gold standard Gd-DOTA (4.5 $mM^{-1}s^{-1}$). Treatment of the particles with reducing agent increased r_1 by about 20% to 54.4 $mM^{-1}s^{-1}$. The high levels of r_1 allow use of significantly lower doses while preserving enough contrast for diagnostics. In addition, the triggered enhancement of r_1 enables localization of regions with increased reduction potential, such as cancerous tissue. *In vitro* cell assays demonstrated low cellular uptake and absence of cellular toxicity of the assembled nanoparticles. Furthermore, they did not show any anticoagulation activity *in vitro* and the stability at room temperature is provided for at least seven months, as demonstrated by constant levels of free gadolinium. All these characteristics make our reduction-sensitive coassemblies a promising candidate to be used as functional high-relaxivity MRI CAs.

5.5 Supporting Information

5.5.1 Nanoparticle Characterization

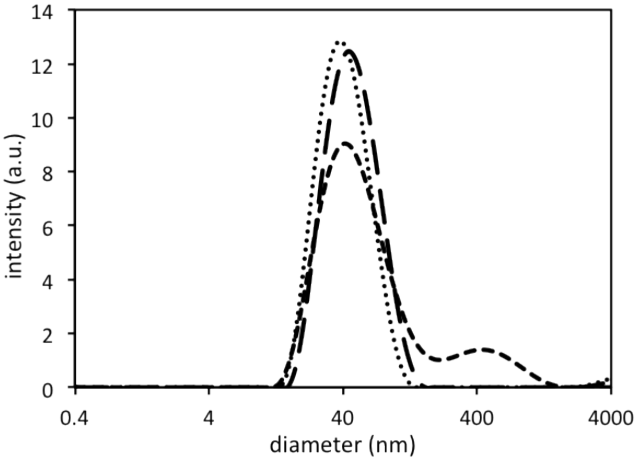

Figure 60. DLS of gadolinium-complexed nanoparticles. HepPDMS-Gd-NPs (broken line), p-hepPDMS-Gd-NPs before (dashed line), and after (dotted line) treatment with DTT.

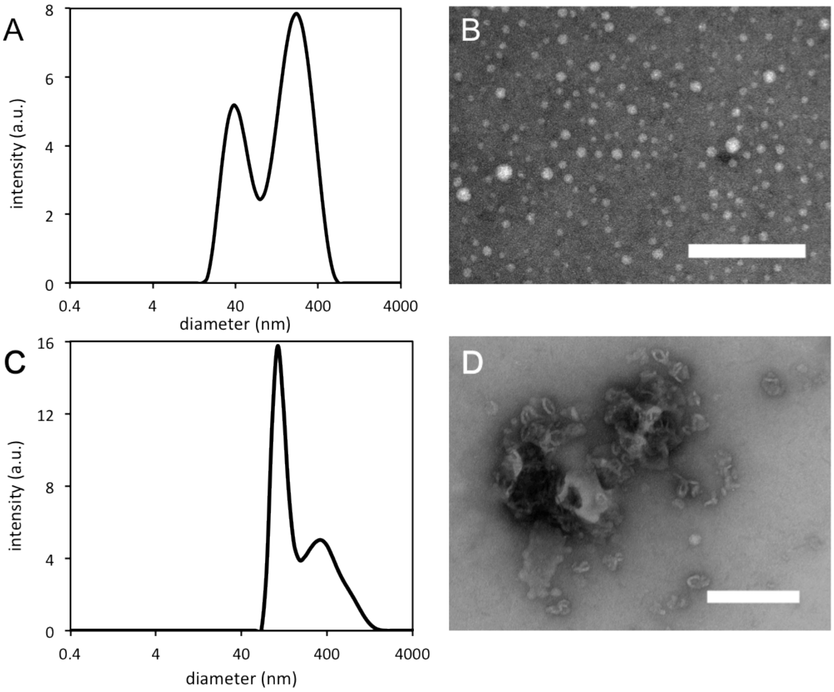

Figure 61. DLS (A) and TEM (B) of hepPDMS-nanoparticles. DLS (C) and TEM (D) of coassemblies formed by using 2 mg/mL H3SSgT peptide. Scale bars: 200 nm.

5.5.2 MRI data

Table 6. Concentrations, longitudinal (T_1) and transversal (T_2) relaxation times of Gd-DOTA, hepPDMS-Gd-NPs, p-hepPDMS-Gd-NPs (–DTT), and p-hepPDMS-Gd-NPs (+DTT).

	Gd-concentration (mM)	T_1 (ms)	T_2 (ms)
Gd-DOTA	0.986	213	204
	0.591	334	341
	0.296	632	680
	0.099	1360	1870
hepPDMS-Gd-NPs	0.930	20.2	6.8
	0.558	31.9	14.9
	0.279	59.8	30.5
	0.093	164	94.9
p-hepPDMS-Gd-NPs (–DTT)	1.057	20.5	9.2
	0.634	31.6	17.0
	0.317	57.9	33.6
	0.106	154	98.5
p-hepPDMS-Gd-NPs (+DTT)	1.057	16.7	8.7
	0.634	25.9	15.2
	0.317	48.6	30.7
	0.106	124	86.8

5.5.3 EPR data

Table 7. EPR parameters and transverse electronic relaxation rates (T_{2e}) of Gd-DOTA and Gd-complexed NPs.

Complex	g	ΔH_{pp} (G)	T_{2e} (ns)
Gd-DOTA	1.980	96	0.77
hepPDMS-Gd-NPs	2.003	430	0.15
p-hepPDMS-Gd-NPs	2.013	390	0.17

Chapter 6

6 General Conclusion and Outlook

In this thesis, short amphiphilic peptides were designed for various biomedical applications. Peptides are particularly interesting due to their intrinsic biocompatibility and biodegradability, which are essential for *in vivo* applicability. The peptide sequences were constructed utilizing gramicidin A inspired hydrophobic regions combined with hydrophilic regions featuring desired and tailor-made properties and functionalities for intended application. Two different hydrophobic regions were used: gA and gT. The sequence of gA is similar to gramicidin A, whereas the gT sequence is based on a truncated version bearing the essential L-tryptophan-D-leucine repeating unit, exhibiting a β-turn secondary structure in aqueous solution. This specific spatial arrangement generates a highly hydrophobic character by hiding the peptidic backbone in the inner core and presenting the side chains (tryptophan and leucine) to the outer environment. In this thesis four projects were conducted, each with different requirements of peptide properties and features.

The first project aimed for the production of peptide nanoparticles for theragnostic purposes, i.e. condensing diagnostic and therapeutic requirements down into one nanoparticle design. An elegant way is the incorporation of gold nanoparticles, due to their high optical density and thermoplasmonic properties. The former allows detection in diagnostic imaging, the latter enables triggered release of entrapped payload upon external stimuli, such as near infrared light. Nanoparticle-forming amphiphilic peptides were C-terminally modified with cysteine for binding to gold nanoparticles, thereby allowing them to subsequently assemble to composite peptide–gold nanoparticle superstructures. The obtained densely packed gold nanoparticle superstructures contain individual gold nanoparticles separated by a peptide bilayer. We proved that these amphiphilic peptides are capable of serving as scaffolds for gold nanoparticles, highlighting the strong driving forces to self-assemble in aqueous solution. These nanoparticles mighty find application in diagnostics, being used for probing cellular uptake pathways, or for real-time drug delivery imaging.

The second project focused on creating a codelivery carrier for antisense oligonucleotides and small molecule drugs. Such systems are crucial for combined treatments to combat multidrug resistance or to exploit synergistic effects of drug–gene or drug–drug combinations. Therefore, amphiphilic peptides were engineered bearing moieties to condense nucleic acid payloads and/or hydrophilic payloads and a hydrophobic region able to entrap small drugs upon self-assembly. The peptides were further equipped with a reduction-sensitive linker for triggered decomposition and cargo release in physiologic conditions at diseases sites. Straightforward rational design combining desired features within one peptide sequence led to noncytotoxic peptide nanoparticles with sizes optimal for biomedical applications (100–150 nm). The created nanoassemblies were able to carry hydrophilic, nucleic acid, and hydrophobic payloads. Further, they revealed high coloading efficiency and were highly sensitive to reductive trigger releasing both payloads in a fast manner. This novel codelivery system is further characterized by effective cell uptake (with and without serum) and high therapeutic efficacy delivering the hydrophilic model drug DoxHCl. Further investigations towards application and therapeutic effects *in vivo* will prove the functionality of the developed system and support the versatile applicability.

The third project addressed the development of amphiphilic peptides bearing polylysine hydrophilic regions to achieve gene transfection *in vitro*. Two peptides were assessed, carrying different lengths of polylysine coupled to a gA sequence and compared to the peptide designed in the second project (H3SSgT). All peptides showed good plasmid DNA condensing abilities and formed nanoparticles in appropriate sizes for biomedical applications. Subsequent transfection experiments revealed high efficiencies. However, due to high positive charge excess cytotoxicity emerged when applied to cells. The cytotoxicity increased proportionally to the transfection efficiency, which might be explained by permeabilization of cell membranes by the lysines, allowing nanoparticles to pass and induce production of mRNA while the survival rate decreased significantly. Apart from the negative effects on cells under these particular conditions, the presented purely peptidic nanoparticle architectures show very promising potential towards highly potent gene transfection agents. However, further optimization and fine-tuning is necessary to obtain nontoxic gene delivery carriers with high efficacy. Promising strategies include the combination of lysines and histidines in the hydrophilic sequence featuring strong DNA condensation abilities, cell uptake and endosomal escape while excessive surface charge is prevented. Moreover, introduction of nuclear localization sequences could possibly lead to more effective transport through the nuclear pores, thereby enhancing efficiency.

The fourth project aimed at the development of a highly sensitive MRI contrast agent. Therefore, we used an amphiphilic block copolymer bearing a hydrophilic block of heparin, known to possess high affinity to trivalent lanthanides such as gadolinium. Gadolinium is widely used as a positive contrast agent to increase contrast in MRI due to its high paramagnetism. The heparin was combined with a hydrophobic block of poly(dimethylsiloxane) to obtain an amphiphilic block copolymer that self-assembles into nanoparticles. The constructed contrast agent revealed relaxivities of more than one order of magnitude higher ($44\,mM^{-1}s^{-1}$) compared to commercially available contrast agents ($\sim 4\,mM^{-1}s^{-1}$). For achieving triggered contrast enhancement, the copolymer was coassembled with a reduction responsive amphiphilic peptide. Physiologic amounts of reducing agent resulted in a relaxivity increase from 44 to 54 $mM^{-1}s^{-1}$, which is about 20%. Important properties such as its nontoxicity, lack of anticoagulation activity, and stability over seven months regarding gadolinium release suggest this reduction-responsive highly sensitive MRI contrast agent as very promising candidate for selective contrast enhancement at disease sites.

In summary, the present dissertation demonstrates, that rational design of amphiphilic peptides can lead to multifunctional, biocompatible, and biodegradable nanoarchitectures self-assembled in a well-defined manner. Functionality is introduced by point mutations in the peptide sequence; however, caution must be taken because small changes in the primary sequence can strongly influence the subsequent secondary structure and self-assembly behavior. The projects presented here provide an array of tailor-made amphiphilic peptides, tuned to distinct properties required for their intended applications. The presented results strongly suggest further studies exploring biologic and pharmacologic parameters such as biocompatibility, biodistribution, and circulation times to advance these systems to *in vivo* applications with high therapeutic and diagnostic efficacy. Furthermore, the diverse functionalities could be extended and/or combined toward theragnostic systems by e.g. combining MRI contrast enhancement capability with triggered codelivery performance. Also, using payloads, which are known to exhibit synergistic effects when applied in combination would allow to thoroughly evaluating the benefits of these nanoparticles regarding the therapeutic efficacy. Future research activities must also focus on the modification of these nanoparticles with specific targeting moieties to further advance their multifunctionality and specificity. Targeting moieties can be introduced as part of the peptide sequence or linked to the peptide post-synthesis. Furthermore, functionalization of the nanoparticles with nuclear localization sequences might enhance the efficiency of gene delivery to cell nuclei due to better transport across the nuclear envelope.

Chapter 7

7 Experimental

7.1 Materials

All reagents and materials were of the highest commercially available grade and were used without further purification, unless mentioned differently. Rink Amide AM resin (0.71 mmol/g), 2-(6-chloro-1*H*-benzotriazole-1-yl)-1,1,3,3-tetramethyluronium hexafluorophosphate (HCTU) and Fmoc-Trp(Boc)-OH were obtained from IRIS Biotech GmbH. Boc-Cystamine-Suc-OH was purchased from IRIS Biotech GmbH and converted into Fmoc-Cystamine-Suc-OH amino acid as described previously.[307] Other amino acids were purchased from Novabiochem. Dimethylformamide (DMF) was obtained from J.T. Baker, ethanol (96 %) F15 and dichloromethane from Brenntag Schweizerhall AG, *N,N*-diisopropylethylamine (DIPEA) from VWR, and acetonitrile (ACN) from Fisher Scientific. BODIPY 630/650 was purchased from Invitrogen. Atto550-labeled, 22-mer oligonucleotide (5' TAA CAG GAT TAG CAG AGC GAG G3') was obtained from Microsynth. Doxorubicin hydrochloride (DoxHCl) (98%) was purchased from Beijing Zhongshuo Pharmaceutical Technology Development Co., Ltd. (China). DMEM, fetal bovine serum, Opti-MEM, and penn/strep were obtained from Gibco. CellTiter 96 AQueous One Solution Cell Proliferation Assay (MTS) was purchased from Promega. FCCS standard double-labeled DNA was obtained from IBA (Göttingen, Germany). Heparin sodium salt from porcine intestinal mucosa (15 kDa, 193 U/mg) was purchased from Merck KGaA (Darmstadt, Germany), Aminopropyl-terminated poly(dimethylsiloxane) was obtained from ABCR GmbH (Karlsruhe, Germany). All other chemicals and reagents were ordered from Sigma-Aldrich. Free amines in DMF were eliminated by aluminum oxide prior to usage. Solvent exchange was performed in dialysis tubes from Spectrum Laboratories (Spectrum Laboratories, cellulose ester, molecular weight cut-off (MWCO) 500–1000 Da or 3500–5000 Da, 3.2 cm/mL, wet in 0.05% sodium azide) or in 24-well crystallization plates (HR3-158, Hampton Research) using water from a Milli-Q Direct 8 water purification system (Merck Millipore).

7.2 Methods

7.2.1 Peptide Synthesis, Purification and Characterization

All peptides were synthesized by solid phase peptide synthesis using a Syro I peptide synthesizer (MultiSyn Tech GmbH, Witten, Germany). The syntheses of all peptides were performed at a 0.17 mmol scale on a Rink amide resin (0.71 mmol/g reactive group concentrations) using standard fluorenylmethoxycarbonyl (Fmoc) chemistry and HCTU coupling protocols. After each coupling cycle the unreacted peptide chains were acetylated using acetic acid anhydride (capping). At the end of the synthesis, the peptidyl resin was isolated and washed alternating with DMF, methanol, and dichloromethane. Acetylation of the N-terminus to obtain AcK6gA was performed using acetic acid anhydride prior to deprotection. Cleavage from the resin and removal of protective groups was performed for 2 h in 10 mL containing 85% trifluoroacetic acid (TFA), 2.5% triisopropylsilane (TIS), 2.5% ethanedithiol (EDT), 5% thioanisole and 5% H_2O for H3SSgT, a mixture of 95% TFA, 2.5% tetraethylsilane (TES), and 2.5% water for H3gT, K3gT, K10gA, and AcK6gA, and a mixture of 95% TFA, 2.5% EDT, and 2.5% water for CK3gT and K3gTC. The cleavage cocktail was filtered and the resin was washed additionally with 1 mL fresh cleavage cocktail. The filtrate was then precipitated in 40 mL cold diethyl ether (H3SSgT) or diisopropyl ether (all other peptides) and then pelleted by centrifugation. The precipitated crude peptides were washed with cold diethyl ether or diisopropyl ether and dried. The peptides were solubilized with ACN and aqueous TFA (0.05 %, v/v) and lyophilized. Purification was carried out by HPLC (Shimadzu Prominence 20A, Japan) on a C18 reverse phase (RP) column (Merck Chromolith, RP-18e, 100 mm × 10 mm and 100 mm × 4.6 mm) with mobile phases of water and acetonitrile containing 0.1% TFA while monitoring at 280 nm (gradient: 20–65% ACN). To obtain AcX3gT, AcCX3gT, and AcX3gTC, the peptides were solubilized in DMF (cysteine peptides were purged with O_2) and acetylated using acetic acid anhydride. Products were purified using HPLC as described above. The molecular mass was determined by liquid chromatography electron spray ionization mass spectrometry (LC-ESI-MS) or matrix assisted laser desorption/ionization time-of-flight mass spectrometry (MALDI-ToF-MS). LC-ESI-MS was performed using an LS instrument from Shimadzu, and an amaZon X MS from Bruker (Germany) with a water–acetonitrile gradient of 5% to 95% ACN over 10 min (detection at 280 nm). The mass was obtained in positive mode and referenced to parabene. MALDI-ToF-MS samples were prepared by mixing 1 μL aliquots of a saturated α-cyano-4-hydroxycinnamic acid stock solution in 50% ACN/0.1% TFA with 1 μL solubilized peptide on a BigAnchorChip MALDI plate. Spectra were acquired on a microflex instrument from Bruker (Germany) using the reflector mode. The acceleration voltage was adjusted to 19 kV and the reflector voltage to 20 kV. Data was collected for a mass range of 500–5000 Da using a detector gain voltage of 1400 V. Lyophilized peptides were stored in the freezer at -20°C.

7.2.2 Film Preparation and Characterization

Using a Hamilton syringe, aliquots of peptide solutions ranging from 50 to 120 mL in $CHCl_3$:EtOH (90:10 v/v), were randomly dropped onto double-distilled H_2O, held in a Langmuir-Blodgett (LB) trough (total area 420 cm^2) from KSV, placed on an anti-vibration table in a dust-free room or, for LB film transfer, on a mini deposition trough (total area 242 cm^2) equipped with a dipper. After spreading, the solvent was allowed to evaporate for 10 minutes, followed by compression of the film at 8 mm min^{-1}. The surface pressure (p) of the monolayers was measured to ± 0.1 mN m^{-1} with a Wilhelmy plate (chromatography paper, ashless Whatman Chr 1) connected to an electro balance. Monolayers were compressed at 20 °C. LB-films were deposited on Si-wafers (previously cleaned in piranha solution (H_2O_2:H_2SO_4 = 3:7) for 10 min and rinsed in double-distilled H_2O), freshly cleaved mica or template-stripped gold (TSG, prepared as described earlier[196]) by pulling the substrate out of the subphase through the interface at a constant rate of 0.5 mm min^{-1} while keeping p at 28 or 35 mN m^{-1}. Immersion took place overnight (12 h) with freshly cleaved TSG in the corresponding solutions, followed by generous washing with ethanol. Samples were either dried in vacuum or were covered with buffer solution. For quartz crystal microbalance (QCM) measurements, frequency and dissipation shifts were monitored using the QSense D300 Quartz Crystal Microbalance (QSense, Gothenburg, Sweden). The QCM sensors consist of a disc-shaped, AT-cut piezoelectric quartz crystal coated with metallic electrodes on both sides. The QCM sensor crystal (1.4 cm diameter crystal, 1.2 cm diameter gold area, 0.2 cm^2 active area, approximately 0.3 mm thickness, roughness of the electrode < 3 nm (rms)) operates at a resonance frequency of 4.95 MHz (50 kHz). The flow cell had an 80 µL working volume. Polarization-modulation infrared reflection-absorption spectra (PM-IRRAS) were recorded on a Bruker IFS equipped with a PMA 37 polarization-modulation accessory. The maximum in polarization retardation was set at 2000 cm^{-1}. Spectra were acquired with a 2 mm aperture and a resolution of 8 cm^{-1} using 1024 scans. The data was processed with OPUS software (Bruker Optics, Germany).

7.2.3 Formation of Gold Nanoparticles

Gold nanoparticles were prepared diluting 2.5 mL of a 10^{-2} M $HAuCl_4$-solution with 47.63 mL of water. After adjusting the pH to 8.0, 250 µL of a 0.1 M $NaBH_4$ solution was added drop-wise, after which the color changed immediately to a dark reddish-brown.[308]

7.2.4 Formation of Composite Peptide–Gold Nanoparticle Superstructures

The cysteine functionalized peptide AcX3gTC was dissolved in ethanol (0.5 mg/mL) containing one equivalent DTT to ensure the availability of the thiol functional groups on the peptides. After mild shaking for three days the gold nanoparticles were added to the peptide solution, in a ratio of 1:1, which corresponds to a 160-fold excess of peptide under the assumption of a hexagonal close packing of the peptide on the gold nanoparticle surface. After a reaction time of three days the mixture was purified from unreacted peptide by dialyzing against 50% ethanol (MWCO = 8–10 kDa) for 3–4 h with three times exchange of solvent. Self-assembly occurred by solvent exchange as described above.

7.2.5 Characterization of Composite Peptide–Gold Nanoparticle Superstructures

Atomic force microscopy (AFM) measurements were carried out using a 5100 Agilent system (formerly PicoLE Molecular Imaging) equipped with a multi-purpose scanner. Images were acquired using a silicon cantilever (type-NCHR PointProbe Plus, force constant 42 N/m) for acoustic mode images. Data were prepared using the open-source software Gwyddion. SEM measurements were carried out using a Hitachi S-4800 operating at 5 keV. Aqueous peptide nanoparticle samples were transferred directly on the sample holder and were allowed to dry overnight. They were sputtered with platinum (5 nm). TEM micrographs were recorded on a FEI Morgani 268D operated at 80 keV. Samples were deposited on carbon-coated, parlodion- (2% in n-butyl acetate) covered copper grids and dried in air. When necessary, staining was performed with uranyl acetate (2% in H_2O) for 10 s. DLS measurements were performed with an ALV/CGS-8F platform-based goniometer system equipped with a HeNe laser at a wavelength of 633 nm (35 mW) and an ALV/-5000/E correlator. Measurements were made at 20 °C and at a scattering angle between 30°–150° in steps of 10°. Correlation functions were fitted by the 2nd cumulant function and extrapolated to zero wave vectors. Data analysis software ALV Stat 4.31 (ALV, Langen, Germany) was used.

7.2.6 Peptide Nanoparticle Formation and Characterization

To prepare peptide nanoparticles, peptides were dissolved in 50% ethanol to obtain 1 mg/mL stock solutions and filtered through 0.2 μm hydrophilic syringe filters. Stock solutions were diluted to a concentration of 0.2 mg/mL using 50% ethanol and subsequently dialyzed for approximately 16 h against water in prewashed 500–1000 Da MWCO dialysis tubes, renewing the exchange solvent twice. After removal of the samples from dialysis tubing, the size distribution was measured from diluted samples in water (1:10 v:v) by dynamic light scattering (DLS). DLS and zeta potential data were carried out using a Zeta Sizer Nano ZSP (Malvern Instruments Ltd., UK) at a fixed angle of $\theta = 173°$ with a laser beam wavelength of 633 nm at room temperature. Transmission electron microscope (TEM) imaging was performed on a Philips CM100 TEM operating at an acceleration voltage of 80 kV. Samples were incubated for 2 min on hydrophilized, carbon coated, parlodion-(2% in n-butyl acetate) copper grids, and when necessary were negatively stained with a 2% uranyl acetate solution (10 s incubation). SEM micrographs were taken on a Philips XL 30 ESEM operating at 5 kV. Samples were prepared on glass coverslips or mica and sputter-coated with silver or platinum. For energy dispersive X-ray spectroscopy (EDX) analysis an FEI Nova NanoSEM was used operating at 10 kV. AFM profiles were obtained from a NanoWizard III instrument from JPK Instruments AG using a PPP-NHCR cantilever (resonance frequency 204–497 kHz) and tapping mode in air. Confocal laser scanning micrographs (CLSM), fluorescence correlation spectroscopy (FCS), and fluorescence cross-correlation spectroscopy (FCCS) data were recorded on a commercial Confocor2 (Carl Zeiss, Jena, Germany), equipped with a laser diode (405 nm), an Ar+ laser (514 nm), and two HeNe lasers for 543 and 633 nm, using a 40× C-Apochromat water immersion objective with a numeric aperture of 1.2.

7.2.7 Payload Embedding and Characterization

BODIPY 630/650 was diluted in dimethyl sulfoxide (DMSO) to 1.5 mM, aliquoted and stored in the freezer at –20°C. 1 µL of 1.5 mM of BODIPY was mixed with 100 µL peptide stock solutions (1 mg/mL), diluted to 500 µL with 50% ethanol and then dialyzed as described above. AON-loaded peptide nanoparticles were prepared by addition of 4 µL of 100 µM AON solution to 100 µL peptide stock solutions (1 mg/mL) and diluted to 500 µL with 35% ethanol. For loading particles with plasmid DNA the plasmid DNA was incubated for 15 min with peptides at different N/P-ratios in 30% ethanol, followed by dialysis to water, renewing exchange solvent twice. Coloading was performed by mixing 4 µL of 100 µM AON with 1 µL of 1.5 mM BODIPY and 100 µL of 1 mg/mL peptide, further diluted to 500 µL with 35% ethanol and dialyzed. DoxHCl-peptide nanoparticles were prepared by adding 40 µL of a 10 mM DoxHCl solution in DMSO to 400 µL peptide stock solution, then diluted to 2 mL with 50% ethanol, mixed and dialyzed as described above. DoxHCl-peptide nanoparticles were separated from nonembedded payload via three centrifugation–decantation cycles (29700 RCF at 5°C). DoxHCl-loading was quantified by fluorescence (PerkinElmer LS55 Luminescence Spectrometer, excitation wavelength: 490 nm, emission wavelength: 555 nm) using a standard dilution curve of DoxHCl. Loading of peptide nanoparticles with BODIPY and AON was measured by FCS. For BODIPY a HFT 633 / LP 650 filter set was used with a pinhole size of 90 µm and a 633 nm laser with a laser power of

5%, while AON was measured using a HFT 543 / LP 560 filter set with a pinhole size of 78 μm and a 543 nm laser at 5% laser power. Loading was confirmed by CLSM for all three payloads: BODIPY, AON, and DoxHCl. For BODIPY a 633 nm laser at 10% transmission was used with NFT 545 and LP 650 filters with a pinhole of 92 μm, AON fluorescence was acquired using a 543 nm laser at 20% transmission and HFT 488/543 and LP 560 filters with a pinhole of 78 μm. DoxHCl was detected using a 488 nm laser at 9.9% transmission with HFT 488, NFT 545, and LP 560 filters and a pinhole of 78 μm. pDNA-loaded particles were prepared by addition 6 μL of a stock solution of 960 μg/mL pDNA to appropriate amounts of ethanolic (30 %) peptide solutions to obtain the desired N/P-ratios. Nanoparticles were formed by dialysis as described above.

7.2.8 Release Experiments From BODIPY/AON-Loaded Nanoparticles

Release experiments were performed by mixing 45 μL of BODIPY- or AON-loaded peptide nanoparticles (0.2 mg/mL) with 5 μL of 100 mM dithiothreitol (DTT) dissolved in 100 mM HEPES buffer at pH 7.2 to obtain a 10 mM DTT solution. As control experiments, loaded peptide nanoparticles were diluted with 100 mM HEPES pH 7.2 to obtain 10 mM buffer concentration. Samples were stirred at room temperature and at indicated time points (2–120 min) 5 μL aliquots were withdrawn and measured subsequently 15 x 5 s by FCS (see payload embedding section for instrument settings). FCS data was fitted with a two-component model, where component 1 was fixed to a free payload diffusion (about 61 μs for BODIPY and about 102 μs for AON) (without triplet state), the structural parameter was fixed to 5. All release experiments were performed in triplicate with error bars representing the standard error. TEM micrographs after DTT treatment were obtained using the conditions described above.

7.2.9 Characterization of BODIPY/AON-Coloaded Nanoparticles

Peptide nanoparticles were prepared as mentioned above. 5 μL aliquots of nanoparticles were placed on a glass slide and micrographs were acquired right above the surface. CLSM micrographs were obtained using a HFT UV/488/543/633, NFT 545, LP 650, and BP 530–600 filter set with 9.9% laser power and a pinhole of 82 μm for the 633 nm laser and 16% laser power and a pinhole of 76 μm for the 543 nm laser. Images were processed and brightness profiles were obtained from the LSM image browser (Zeiss). FCCS data was recorded using HFT 514, LP 650, and BP 530–600 filters; a 514 nm laser at 20% transmission with a pinhole of 70 μm and a 633 nm laser at 5% transmission with a 70 μm pinhole. All data was fitted using a one-component model without triplet state and a structural parameter of 5 using ConfoCor3 software to obtain autocorrelation and the cross-correlation functions:

$$\mathrm{G}(\tau)_{\mathrm{fit}} = 1 + \frac{1}{N}\left[\frac{1}{1+\frac{\tau}{\tau_{\mathrm{D}}}} \frac{1}{\sqrt{1+R^2\frac{\tau}{\tau_{\mathrm{D}}}}}\right] \tag{9}$$

τ_D is the diffusion time, N the number of particles, and R the structural parameter (was fixed to 5). Relative cross-correlation amplitudes (RCA) were calculated using the cross-correlation amplitude $G_x(0)$ and the autocorrelation amplitudes of the AON and BODIPY channels $G_{AON,BODIPY}(0)$, respectively:

$$RCA = \frac{G_x(0)-1}{G_{AON,BODIPY}(0)-1} \tag{10}$$

The coloading degree (CLD) was calculated by normalizing the data where the minimal cross-correlation of a mixture of both payloads in solution was set to 0% and the maximal cross-correlation from a double-labeled DNA standard (IBA standard) was set to 100%.

7.2.10 Electrophoretic Mobility Shift Assay

Electrophoretic Mobility Shift Assays (EMSA) were performed on 1.2% agarose gels using TEA buffer. A constant voltage of 100 V was applied and gels were run for 40–50 min. Sample volumes were kept at 10 µl. 2 µl loading dye (6× Mass Ruler DNA loading dye from Thermo Scientific) was added prior to electrophoresis. Agarose gels were stained with GelRed dye (Biotinum, USA). On each gel the first lane represents the pDNA control. For release experiments samples were incubated for indicated time periods in 200 mM DTT solutions in HEPES pH 7.2 at room temperature prior to analysis.

7.2.11 Cell Culture

HeLa and U87 cells were grown in Dulbecco's modified eagle medium (DMEM) with 10% fetal bovine serum (FBS), 100 units/mL penicillin and 100 µg/mL streptomycin and maintained at 37 °C in 5% CO_2.

7.2.12 Cell Viability Assay (MTS)

Cytotoxicity analysis was performed using the Promega CellTiter 96 AQueous Non-Radioactive Cell Proliferation (MTS) assay to determine the number of viable cells in culture. Triplicate or quintuplicate wells containing 2000–5000 HeLa or U87 cells were seeded in a 96-well plate 24 h prior to the experiment in order to achieve confluency at the time of analysis. 10 μL aliquots of peptide nanoparticle solution were added to the cells to give final concentrations between 50–300 μg/mL or 25–1000 μg/mL and incubated for 24 or 48 h at 37°C with 5% CO_2. MTS solution (20 μL/well) was added to the cells and then incubated for 2h. Cell viability in each well was calculated by measuring the absorbance of the cell solution (cells and media containing the nanoparticles) mixed with MTS solution at 490 nm using a SpectraMax M5^e (Molecular Device) spectrometer with a plate reader, and data was normalized against cells incubated with water or HEPES buffer (100% viability) and background subtracted with the absorbance from the MTS alone. To obtain IC50 values the experimental viability was fitted using exponential curves.

7.2.13 Cell Uptake of BODIPY- and/or AON-Loaded Nanoparticles

HeLa (2×10^4 or 5×10^4 cells per well) were seeded into an 8-well chamber 24 h prior to the experiment. After 24 hours, the cell culture media was replaced with Opti-MEM (130 μL) followed by addition of 20 μL 0.2 mg/mL peptide nanoparticles. After 4 h incubation, the cell culture medium was replaced with serum-containing media (300 μL). The cells were then incubated for another 20 h. For cell uptake with serum the medium supplemented with 10% FBS was renewed prior to sample application. Prior to live cell imaging, the media was replaced by phosphate buffered saline (PBS) and the cell nuclei were stained for 10 min with 1.6 μL of a 50 μg/mL Hoechst 33342 solution in PBS. Cell imaging was performed by CLSM. The samples were excited at 405 nm (Hoechst 33342), 543 nm (for AON), and 633 nm (for BODIPY) while collecting the emission after a BP 420–480 filter (Hoechst 33342), a BP 530–600 filter (AON), and a LP 650 filter (BODIPY), respectively. Images were taken with the same acquisition settings for comparison purposes.

7.2.14 Imaging of GFP-Transfected Cells

U87 cells (5×10^4 cells per well) were seeded into an 8-well chamber 24 h prior to the experiment. The cell culture medium was replaced by Opti-MEM (130 μL) followed by addition of samples to obtain 1 μg pDNA/well. After 4 h, the cell culture media was replaced by serum-containing media (300 μL). Prior to imaging, the media was replaced by PBS. Imaging was performed by CLSM using 488 nm laser at 5.0% transmission collecting the emission after an LP 505 filter.

7.2.15 Flow Cytometry Analysis

HeLa or U87 cells (7×10^4 or 5×10^4 cells/well) were plated into 24-well tissue culture plates 24 h prior to the experiment. The cell culture media was replaced with serum-free media (460 µL) and 40 µl 0.2 mg/mL peptide nanoparticles were added. After 4 h incubation, the serum-free medium was carefully removed and replaced with 1 ml of medium containing 10% FBS. The cells were then incubated another 20 or 44 h. Cells were trypsinized with 200 µl of trypsin for 10 min at 37 °C and 5% CO_2. Following trypsinization, 800 µl PBS were added to the cells, gently mixed by pipetting and transferred into 1.5 mL microcentrifuge tubes. Cells were then pelleted by centrifugation at 200 RCF for 5 min. Subsequently, the media was aspirated and the pellet was resuspended in 250 µl PBS (for cell uptake studies) or 400 µL (transfection and toxicity studies) and put on ice. 6 µL aliquots of 50 µg/mL stock solution of Hoechst 33342 were added to each sample. For propidium iodide (PI)–Hoechst assays 1 µL aliquots of 1 mg/mL stock solutions of PI and 0.5 µL aliquots of 5 mg/mL stock solutions of Hoechst 33342 were added to each sample. Immediately prior to fluorescence assisted cell sorting (FACS) analysis, the cells were vortexed gently. FACS measurements of AON-loaded nanoparticles were performed by measuring at least 3×10^4 cells with a BD LSR Fortessa, the cells were excited with lasers at 405 and 561 nm, the emitted light passed through band-pass 450/50 and 586/15 filters, respectively. The data were processed with FlowJo Vx (Tree Star, USA) and a fluorescence histogram of viable cells only was plotted or the mean fluorescence intensity was extracted. Flow cytometry analysis of GFP-transfected cells were performed by measuring at least 2×10^4 cells. The cells were excited using 405 and 488 nm lasers, and 450/50 and 529/24 band-pass filters. For Hoechst 33342–propidium iodine staining 405 and 488 nm lasers and 450/50 and 585/40 band-pass filters were applied. Transfection efficacies and relative populations were obtained by gating forward- versus side-scattering plots and GFP-histograms relative to nontreated control cells. Toxicities were calculated by gating the cell counts using a propidium iodide (PI) versus Hoechst 33342-plot according to nontreated control cells.

7.2.16 Heparin-PDMS Synthesis

Heparin-PDMS block copolymer was synthesized as reported previously.[294] Briefly, heparin sodium salt was converted to tetrabutylammonium salt using a Dowex Marathon MSC column (Sigma-Aldrich, 428787) neutralizing to pH 7 with tetrabutylammonium hydroxide solution (Sigma-Aldrich, 86863). The product was purified via dialysis against water for at least 48 h (Spectrum Laboratories Inc., CA, USA, MWCO 3.5–5 kDa) and dried. Heparin tetrabutylammonium salt was reacted with $PDMS(NH_2)_2$ for 7 days, then precipitated in diethyl ether, washed, purified and dried.

7.2.17 Gadolinium-Complex and Nanoparticle Formation and Characterization

HepPDMS was dissolved in 50% ethanol and filtered (0.45 μm) to obtain a 17 mg/mL clear solution. After dilution to 4.25 mg/mL and pH adjustment to pH 7 using diluted NaOH, the solution was dialyzed against water for 16 h, renewing exchange solvent twice, using prewashed 500–1000 Da MWCO dialysis tubes. HepPDMS-Gd nanoparticles were formed by adding gadolinium chloride hexahydrate stock solution (27 mM) dropwise under stirring to above described hepPDMS stock solution (17 mg/mL). The pH was readjusted to 7 when necessary, diluted to 4.25 mg/mL HepPDMS and to a final gadolinium concentration of 2.4 mM, then dialyzed to water as described above. For production of coassemblies the peptides were first dissolved in 50% ethanol to obtain 1 mg/mL stock solutions and then filtered through 0.2 μm hydrophilic syringe filters. HepPDMS-Gd stock solutions (8.5 mg/mL) were mixed 1:1 with peptide stock solution and subsequently dialyzed as described above.

7.2.18 Cell Uptake of Gadolinium Constructs

Hela cells (5×10^4 cells per well) were seeded in triplicates into a 24-well chamber 24 h prior to the experiment. The cell culture media was replaced with Opti-MEM (150 μL) followed by addition of 20 μL peptide HepPDMS-Gd nanoparticles. After 4 h incubation, the cell culture medium was removed and replaced with serum-containing medium (500 μL). The cells were then incubated for another 20 h. Cells were washed with opti-MEM, trypsinized, transferred to Falcon tubes and digested in 65% HNO_3 over night. Subsequently, the gadolinium-content was determined using inductively coupled plasma optical emission spectroscopy (ICP-OES).

7.2.19 Inductively Coupled Plasma-Optical Emission Spectroscopy

All gadolinium contents were determined by inductively coupled plasma-optical emission spectroscopy (ICP-OES). Quantification of gadolinium was carried out on a Ciros Vision ICP-OES from Spektro (Kleve, Germany) in axial mode. Gadolinium stock solutions of known metal content were measured prior to sample measurements to plot calibration curves. All samples were digested by 65% HNO_3 over night and diluted to 2% HNO_3 prior to analysis.

7.2.20 Anticoagulation Activity

The anticoagulation activity was determined by a Biophen Heparin (LRT) kit determining the absorption of cleaved pNA, indirectly based on the inhibition of factor Xa in the coagulation cascade. The absorbance was measured at 405 nm using a STA-R analyzer from Stago.

7.2.21 Farndale Microassay

Accessible heparin was determined by Farndale microassay as described previously.[294,309] Briefly, 250 µl 1,9-dimethylmethylene blue (DMMB) stock solution was mixed with 50 µl heparin standards (2.5–20 µg/mL). Samples were diluted to the range of the calibration curve using PBS. Absorption was measured at 525 nm and the heparin levels of samples were calculated using a standard dilution curve.

7.2.22 Xylenol Orange Assay

Free gadolinium levels were analyzed by xylenol orange assay according to a published procedure.[310] Briefly, xylenol orange tetrasodium salt was diluted in 10 mM HEPES buffer pH 6 to obtain a 12 µg/mL stock solution. Samples were diluted to the linear range and 10 µL aliquots were mixed with 100 µL xylenol orange stock solution. For stability tests samples where maintained in opti-MEM with FBS, after 7 days 10 µL sample was added to 100 µL stock solution in triplicates and absorption was measured at 433 and 473 nm. Gadolinium-ion concentration was calculated using a calibration curve of the ratio of absorption at 573 and 433 nm plotted against gadolinium-concentration.

7.2.23 Electron Paramagnetic Resonance Spectroscopy

Electron paramagnetic resonance (EPR) spectra were recorded with a CW Bruker ElexSys500 X-band CW spectrometer, to which the superQ wave-guide resonance cavity (ER4122 SHQE-W1) was attached. Microwave power was adjusted at levels below the saturation condition with values 2.0–6.0 mW. The modulation frequency was 100 kHz and the modulation amplitude was 0.9 mT; other spectral parameters were adjusted for each spectrum individually. 80 spectra were acquired to optimize the signal-to-noise ratio, and 3rd-order polynomial averaging was used for subsequent noise reduction. Gd samples were measured at room temperature. Lorentzian line shapes were considered with the line-width adjusted for each spectrum. The peak-to-peak line width was measured from the spectrum using the WINEPR software. The pH of the samples was adjusted to 7 with NaOH.

7.2.24 Magnetic Resonance Imaging

Samples were measured in 1.5 mL centrifuge vials in denoted concentrations. For imaging a 3T clinical human MRI scanner was used from Siemens was used. The T_1 relaxation times were measured using an inversion recovery prepared spin echo sequence with the following acquisition parameters: voxel size 1.2×1.2×5 mm^3, TR/TE 6000/12 ms. The scan was repeated at various inversion times (TI): 50 ms, 100 ms, 200 ms, 500 ms, 750 ms, 1000 ms, and 2000 ms. The T_2 relaxation times of the samples were measured using a multi-echo spin echo sequence with the following acquisition parameters: voxel size 1.2×1.2×5 mm^3, TR 3000 ms. 32 echoes were acquired with a 13.2 ms echo spacing (first echo: 13.2 ms, last echo: 422.4 ms).

Chapter 8

8 References

(1) Gunkel-Grabole, G.; Sigg, S.; Lomora, M.; Lörcher, S.; Palivan, C. G.; Meier, W. P. Polymeric 3D nano-architectures for transport and delivery of therapeutically relevant biomacromolecules. *Biomater. Sci.* **2015**, 3, (1), 25-40.

(2) de Bruyn Ouboter, D.; Schuster, T. B.; Sigg, S. J.; Meier, W. P. Self-assembled peptide beads used as a template for ordered gold nanoparticle superstructures. *Colloids Surf., B* **2013**, 112, 542-547.

(3) Whitesides, G. M.; Grzybowski, B. Self-Assembly at All Scales. *Science* **2002**, 295, (5564), 2418-2421.

(4) Han, D.; Pal, S.; Nangreave, J.; Deng, Z.; Liu, Y.; Yan, H. DNA Origami with Complex Curvatures in Three-Dimensional Space. *Science* **2011**, 332, (6027), 342-346.

(5) Torchilin, V. P. Recent advances with liposomes as pharmaceutical carriers. *Nat. Rev. Drug Discovery* **2005**, 4, (2), 145-160.

(6) Pattni, B. S.; Chupin, V. V.; Torchilin, V. P. New Developments in Liposomal Drug Delivery. *Chem. Rev. (Washington, DC, U. S.)* **2015**, 115, (19), 10938-10966.

(7) Kita-Tokarczyk, K.; Grumelard, J.; Haefele, T.; Meier, W. Block copolymer vesicles—using concepts from polymer chemistry to mimic biomembranes. *Polymer* **2005**, 46, (11), 3540-3563.

(8) Hotz, J.; Meier, W. Vesicle-Templated Polymer Hollow Spheres. *Langmuir* **1998**, 14, (5), 1031-1036.

(9) Meier, W. Polymer nanocapsules. *Chem. Soc. Rev.* **2000**, 29, (5), 295-303.

(10) Palivan, C. G.; Goers, R.; Najer, A.; Zhang, X.; Car, A.; Meier, W. Bioinspired polymer vesicles and membranes for biological and medical applications. *Chem. Soc. Rev.* **2016**, 45, (2), 377-411.

(11) van Hell, A. J.; Costa, C. I. C. A.; Flesch, F. M.; Sutter, M.; Jiskoot, W.; Crommelin, D. J. A.; Hennink, W. E.; Mastrobattista, E. Self-Assembly of Recombinant Amphiphilic Oligopeptides into Vesicles. *Biomacromolecules* **2007**, 8, (9), 2753-2761.

(12) Bellomo, E. G.; Wyrsta, M. D.; Pakstis, L.; Pochan, D. J.; Deming, T. J. Stimuli-responsive polypeptide vesicles by conformation-specific assembly. *Nat. Mater.* **2004**, 3, (4), 244-248.

(13) Holowka, E. P.; Pochan, D. J.; Deming, T. J. Charged Polypeptide Vesicles with Controllable Diameter. *J. Am. Chem. Soc.* **2005**, 127, (35), 12423-12428.

(14) Najer, A.; Wu, D.; Vasquez, D.; Palivan, C. G.; Meier, W. Polymer nanocompartments in broad-spectrum medical applications. *Nanomedicine* **2013**, 8, (3), 425-447.

(15) Renggli, K.; Baumann, P.; Langowska, K.; Onaca, O.; Bruns, N.; Meier, W. Selective and Responsive Nanoreactors. *Adv. Funct. Mater.* **2011**, 21, (7), 1241-1259.

(16) Palivan, C. G.; Fischer-Onaca, O.; Delcea, M.; Itel, F.; Meier, W. Protein-polymer nanoreactors for medical applications. *Chem. Soc. Rev.* **2012**, 41, (7), 2800-2823.

(17) Langowska, K.; Palivan, C. G.; Meier, W. Polymer nanoreactors shown to produce and release antibiotics locally. *Chem. Commun. (Cambridge, U. K.)* **2013**, 49, (2), 128-130.

(18) Zhang, X.; Tanner, P.; Graff, A.; Palivan, C. G.; Meier, W. Mimicking the cell membrane with block copolymer membranes. *J. Polym. Sci., Part A: Polym. Chem.* **2012**, 50, (12), 2293-2318.

(19) Cui, H.; Webber, M. J.; Stupp, S. I. Self-assembly of peptide amphiphiles: from molecules to nanostructures to biomaterials. *Biopolymers* **2010**, 94, (1), 1-18.

(20) Shu, J. Y.; Panganiban, B.; Xu, T. Peptide-polymer conjugates: from fundamental science to application. *Annu. Rev. Phys. Chem.* **2013**, 64, 631-657.

(21) Cavalli, S.; Albericio, F.; Kros, A. Amphiphilic peptides and their cross-disciplinary role as building blocks for nanoscience. *Chem. Soc. Rev.* **2010**, 39, (1), 241-263.

(22) Hamley, I. W. Self-assembly of amphiphilic peptides. *Soft Matter* **2011**, 7, (9), 4122.

(23) Khoe, U.; Yang, Y.; Zhang, S. Self-Assembly of Nanodonut Structure from a Cone-Shaped Designer Lipid-like Peptide Surfactant. *Langmuir* **2009**, 25, (7), 4111-4114.

(24) Seow, W. Y.; Yang, Y.-Y. A Class of Cationic Triblock Amphiphilic Oligopeptides as Efficient Gene-Delivery Vectors. *Adv. Mater. (Weinheim, Ger.)* **2009**, 21, (1), 86-90.

(25) Tang, Q.; Cao, B.; Wu, H.; Cheng, G. Selective gene delivery to cancer cells using an integrated cationic amphiphilic peptide. *Langmuir* **2012**, 28, (46), 16126-16132.

(26) Breedveld, V.; Nowak, A. P.; Sato, J.; Deming, T. J.; Pine, D. J. Rheology of Block Copolypeptide Solutions: Hydrogels with Tunable Properties. *Macromolecules* **2004**, 37, (10), 3943-3953.

(27) Schuster, T. B.; de Bruyn Ouboter, D.; Palivan, C. G.; Meier, W. From fibers to micelles using point-mutated amphiphilic peptides. *Langmuir* **2011**, 27, (8), 4578-4584.

(28) Schuster, T. B.; de Bruyn Ouboter, D.; Bruns, N.; Meier, W. Exploiting Dimerization of Purely Peptidic Amphiphiles to Form Vesicles. *Small* **2011**, 7, (15), 2158-2162.

(29) de Bruyn Ouboter, D.; Schuster, T. B.; Mantion, A.; Meier, W. Hierarchical Organization of Purely Peptidic Amphiphiles into Peptide Beads. *J. Phys. Chem. C* **2011**, 115, (30), 14583-14590.

(30) Schuster, T. B.; de Bruyn Ouboter, D.; Bordignon, E.; Jeschke, G.; Meier, W. Reversible peptide particle formation using a mini amino acid sequence. *Soft Matter* **2010**, 6, (21), 5596-5604.

(31) Dittrich, C.; Meier, W. Solid Peptide Nanoparticles - Structural Characterization and Quantification of Cargo Encapsulation. *Macromol. Biosci.* **2010**, 10, (12), 1406-1415.

(32) Chen, C.; Pan, F.; Zhang, S.; Hu, J.; Cao, M.; Wang, J.; Xu, H.; Zhao, X.; Lu, J. R. Antibacterial Activities of Short Designer Peptides: a Link between Propensity for Nanostructuring and Capacity for Membrane Destabilization. *Biomacromolecules* **2010**, 11, (2), 402-411.

(33) Santoso, S.; Hwang, W.; Hartman, H.; Zhang, S. Self-assembly of surfactant-like peptides with variable glycine tails to form nanotubes and nanovesicles. *Nano Lett.* **2002**, 2, (7), 687-691.

(34) Vauthey, S.; Santoso, S.; Gong, H.; Watson, N.; Zhang, S. Molecular self-assembly of surfactant-like peptides to form nanotubes and nanovesicles. *Proc. Natl. Acad. Sci. U. S. A.* **2002**, 99, (8), 5355-5360.

(35) Branco, M. C.; Pochan, D. J.; Wagner, N. J.; Schneider, J. P. Macromolecular diffusion and release from self-assembled β-hairpin peptide hydrogels. *Biomaterials* **2009**, 30, (7), 1339-1347.

(36) Aggeli, A.; Nyrkova, I. A.; Bell, M.; Harding, R.; Carrick, L.; McLeish, T. C.; Semenov, A. N.; Boden, N. Hierarchical self-assembly of chiral rod-like molecules as a model for peptide beta - sheet tapes, ribbons, fibrils, and fibers. *Proc. Natl. Acad. Sci. U. S. A.* **2001**, 98, (21), 11857-11862.

(37) Bucak, S.; Cenker, C.; Nasir, I.; Olsson, U.; Zackrisson, M. Peptide nanotube nematic phase. *Langmuir* **2009**, 25, (8), 4262-4265.

(38) Adams, D. J.; Holtzmann, K.; Schneider, C.; Butler, M. F. Self-Assembly of Surfactant-like Peptides. *Langmuir* **2007**, 23, (25), 12729-12736.

(39) Baumann, M. K.; Textor, M.; Reimhult, E. Understanding Self-Assembled Amphiphilic Peptide Supramolecular Structures from Primary Structure Helix Propensity. *Langmuir* **2008**, 24, (15), 7645-7647.

(40) Huang, Z.; Guan, S.; Wang, Y.; Shi, G.; Cao, L.; Gao, Y.; Dong, Z.; Xu, J.; Luo, Q.; Liu, J. Self-assembly of amphiphilic peptides into bio-functionalized nanotubes: a novel hydrolase model. *J. Mater. Chem. B* **2013**, 1, (17), 2297-2304.

(41) Morris, M. C.; Gros, E.; Aldrian-Herrada, G.; Choob, M.; Archdeacon, J.; Heitz, F.; Divita, G. A non-covalent peptide-based carrier for in vivo delivery of DNA mimics. *Nucleic Acids Res.* **2007**, 35, (7), e49.

(42) Orbach, R.; Adler-Abramovich, L.; Zigerson, S.; Mironi-Harpaz, I.; Seliktar, D.; Gazit, E. Self-Assembled Fmoc-Peptides as a Platform for the Formation of Nanostructures and Hydrogels. *Biomacromolecules* **2009**, 10, 2646-2651.

(43) Sarges, R.; Witkop, B. Gramicidin A. VII. The structure of valine- and isoleucine-gramicidin B. *J. Am. Chem. Soc.* **1965**, 2027-2030.

(44) Bruyn Ouboter, D. D.; Schuster, T.; Shanker, V.; Heim, M.; Meier, W. Multicompartment micelle-structured peptide nanoparticles: A new biocompatible gene- and drug-delivery tool. *J. Biomed. Mater. Res., Part A* **2013**.

(45) Sigg, S. J.; Schuster, T. B.; Meier, W. Self-assembled Structures from Amphiphilic Peptides. *Chimia* **2013**, 67, (12), 881-884.

(46) Lee, O.-S.; Stupp, S. I.; Schatz, G. C. Atomistic Molecular Dynamics Simulations of Peptide Amphiphile Self-Assembly into Cylindrical Nanofibers. *J. Am. Chem. Soc.* **2011**, 133, (10), 3677-3683.

(47) Kwon, G. S.; Kataoka, K. Block copolymer micelles as long-circulating drug vehicles. *Adv. Drug Delivery Rev.* **2012**, 64, 237-245.

(48) Talelli, M.; Rijcken, C. J.; van Nostrum, C. F.; Storm, G.; Hennink, W. E. Micelles based on HPMA copolymers. *Adv. Drug Delivery Rev.* **2010**, 62, (2), 231-239.

(49) Ponta, A.; Bae, Y. PEG-poly(amino acid) Block Copolymer Micelles for Tunable Drug Release. *Pharm. Res.* **2010**, 27, (11), 2330-2342.

(50) Braun, J.; Bruns, N.; Pfohl, T.; Meier, W. Phase Behavior of Vesicle-Forming Block Copolymers in Aqueous Solutions. *Macromol. Chem. Phys.* **2011**, 212, (12), 1245-1254.

(51) Matter, Y.; Enea, R.; Casse, O.; Lee, C. C.; Baryza, J.; Meier, W. Amphiphilic PEG-b-PMCL-b-PDMAEMA Triblock Copolymers: From Synthesis to Physico-Chemistry of Self-Assembled Structures. *Macromol. Chem. Phys.* **2011**, 212, 937-949.

(52) Belegrinou, S.; Dorn, J.; Kreiter, M.; Kita-Tokarczyk, K.; Sinner, E.-K.; Meier, W. Biomimetic supported membranes from amphiphilic block copolymers. *Soft Matter* **2009**, 6, (1), 179-186.

(53) Makovec, T. Poly-L-glutamic acid and poly-L-lysine: model substances for studying secondary structures of proteins. *Biochem. Mol. Biol. Educ.* **2000**, 28, (5), 244-247.

(54) Spek, E. J.; Gong, Y.; Kallenbach, N. R. Intermolecular Interactions in α Helical Oligo- and Poly(L-glutamic acid) at Acidic pH. *J. Am. Chem. Soc.* **1995**, 117, (43), 10773-10774.

(55) de Raad, M.; Teunissen, E. A.; Lelieveld, D.; Egan, D. A.; Mastrobattista, E. High-content screening of peptide-based non-viral gene delivery systems. *J. Controlled Release* **2012**, 158, (3), 433-442.

(56) Randal, M.; Kossiakoff, A. A. Crystallization and preliminary x-ray analysis of a 1:1 complex between a designed monomeric interferon-gamma and its soluble receptor. *Protein Sci.* **1998**, 7, (4), 1057-1060.

(57) Ringsdorf, H. Structure and properties of pharmacologically active polymers. *J. Polym. Sci., Polym. Symp.* **1975**, 51, (1), 135-153.

(58) Jahnke, E.; Lieberwirth, I.; Severin, N.; Rabe, J. P.; Frauenrath, H. Topochemical polymerization in supramolecular polymers of oligopeptide-functionalized diacetylenes. *Angew. Chem., Int. Ed.* **2006**, 45, (32), 5383-5386.

(59) Vandermeulen, G. W. M.; Klok, H.-A. Peptide/protein hybrid materials: Enhanced control of structure and improved performance through conjugation of biological and synthetic polymers. *Macromol. Biosci.* **2004**, 4, (4), 383-398.

(60) von Berlepsch, H.; Boettcher, C.; Skrabania, K.; Laschewsky, A. Complex domain architecture of multicompartment micelles from a linear ABC triblock copolymer revealed by cryogenic electron tomography. *Chem. Commun. (Cambridge, U. K.)* **2009**, (17), 2290-2292.

(61) Lutz, J.-F.; Laschewsky, A. Multicompartment micelles: Has the long-standing dream become a reality? *Macromol. Chem. Phys.* **2005**, 206, (8), 813-817.

(62) Kubowicz, S.; Baussard, J.-F.; Lutz, J.-F.; Thuenemann, A. F.; von Berlepsch, H.; Laschewsky, A. Multicompartment micelles formed by self-assembly of linear ABC triblock copolymers in aqueous medium. *Angew. Chem., Int. Ed.* **2005**, 44, (33), 5262-5265.

(63) Margus, H.; Padari, K.; Pooga, M. Cell-penetrating peptides as versatile vehicles for oligonucleotide delivery. *Mol. Ther.* **2012**, 20, (3), 525-533.

(64) Aliabadi, H. M.; Landry, B.; Sun, C.; Tang, T.; Uludag, H. Supramolecular assemblies in functional siRNA delivery: where do we stand? *Biomaterials* **2012**, 33, (8), 2546-2569.

(65) Tibbitt, M. W.; Dahlman, J. E.; Langer, R. Emerging Frontiers in Drug Delivery. *J. Am. Chem. Soc.* **2016**, 138, (3), 704-717.

(66) Yang, F. H.; Zhang, Q.; Liang, Q. Y.; Wang, S. Q.; Zhao, B. X.; Wang, Y. T.; Cai, Y.; Li, G. F. Bioavailability enhancement of paclitaxel via a novel oral drug delivery system: paclitaxel-loaded glycyrrhizic acid micelles. *Molecules* **2015**, 20, (3), 4337-4356.

(67) Hoyer, J.; Neundorf, I. Peptide Vectors for the Nonviral Delivery of Nucleic Acids. *Acc. Chem. Res.* **2012**, 45, (7), 1048-1056.

(68) Hillaireau, H.; Couvreur, P. Nanocarriers' entry into the cell: relevance to drug delivery. *Cell. Mol. Life Sci.* **2009**, 66, (17), 2873-2896.

(69) Alexis, F.; Pridgen, E.; Molnar, L. K.; Farokhzad, O. C. Factors Affecting the Clearance and Biodistribution of Polymeric Nanoparticles. *Mol. Pharm.* **2008**, 5, (4), 505-515.

(70) He, C.; Hu, Y.; Yin, L.; Tang, C.; Yin, C. Effects of particle size and surface charge on cellular uptake and biodistribution of polymeric nanoparticles. *Biomaterials* **2010**, 31, (13), 3657-3666.

(71) Choi, H. S.; Liu, W.; Misra, P.; Tanaka, E.; Zimmer, J. P.; Itty Ipe, B.; Bawendi, M. G.; Frangioni, J. V. Renal clearance of quantum dots. *Nat. Biotechnol.* **2007**, 25, (10), 1165-1170.

(72) Quan, C. Y.; Chen, J. X.; Wang, H. Y.; Li, C.; Chang, C.; Zhang, X. Z.; Zhuo, R. X. Core-shell nanosized assemblies mediated by the alpha-beta cyclodextrin dimer with a tumor-triggered targeting property. *ACS Nano* **2010**, 4, (7), 4211-4219.

(73) Yuan, Y. Y.; Mao, C. Q.; Du, X. J.; Du, J. Z.; Wang, F.; Wang, J. Surface charge switchable nanoparticles based on zwitterionic polymer for enhanced drug delivery to tumor. *Adv. Mater. (Weinheim, Ger.)* **2012**, 24, (40), 5476-5480.

(74) Yang, X. Z.; Du, J. Z.; Dou, S.; Mao, C. Q.; Long, H. Y.; Wang, J. Sheddable ternary nanoparticles for tumor acidity-targeted siRNA delivery. *ACS Nano* **2012**, 6, (1), 771-781.

(75) Helmlinger, G.; Sckell, A.; Dellian, M.; Forbes, N. S.; Jain, R. K. Acid Production in Glycolysis-impaired Tumors Provides New Insights into Tumor Metabolism. *Clin. Cancer Res.* **2002**, 8, (4), 1284-1291.

(76) Danhier, F.; Feron, O.; Preat, V. To exploit the tumor microenvironment: Passive and active tumor targeting of nanocarriers for anti-cancer drug delivery. *J. Controlled Release* **2010**, 148, (2), 135-146.

(77) Torchilin, V. P. Multifunctional, stimuli-sensitive nanoparticulate systems for drug delivery. *Nat. Rev. Drug Discovery* **2014**, 13, (11), 813-827.

(78) Li, Y.; Xiao, K.; Zhu, W.; Deng, W.; Lam, K. S. Stimuli-responsive cross-linked micelles for on-demand drug delivery against cancers. *Adv. Drug Delivery Rev.* **2014**, 66, 58-73.

(79) Mukherjee, S. P.; Lyng, F. M.; Garcia, A.; Davoren, M.; Byrne, H. J. Mechanistic studies of in vitro cytotoxicity of poly(amidoamine) dendrimers in mammalian cells. *Toxicol. Appl. Pharmacol.* **2010**, 248, (3), 259-268.

(80) Naha, P. C.; Davoren, M.; Lyng, F. M.; Byrne, H. J. Reactive oxygen species (ROS) induced cytokine production and cytotoxicity of PAMAM dendrimers in J774A.1 cells. *Toxicol. Appl. Pharmacol.* **2010**, 246, (1-2), 91-99.

(81) Yokoyama, M. Polymeric micelles as a new drug carrier system and their required considerations for clinical trials. *Expert Opin. Drug Deliv.* **2010**, 7, (2), 145-158.

(82) Tian, B.; Tao, X.; Ren, T.; Weng, Y.; Lin, X.; Zhang, Y.; Tang, X. Polypeptide-based vesicles: formation, properties and application for drug delivery. *J. Mater. Chem.* **2012**, 22, (34), 17404.

(83) Nitta, S. K.; Numata, K. Biopolymer-based nanoparticles for drug/gene delivery and tissue engineering. *Int. J. Mol. Sci.* **2013**, 14, (1), 1629-1654.

(84) Couvreur, P. Nanoparticles in drug delivery: past, present and future. *Adv. Drug Delivery Rev.* **2013**, 65, (1), 21-23.

(85) Deshayes, S.; Morris, M.; Heitz, F.; Divita, G. Delivery of proteins and nucleic acids using a non-covalent peptide-based strategy. *Adv. Drug Delivery Rev.* **2008**, 60, (4-5), 537-547.

(86) Panyam, J.; Labhasetwar, V. Biodegradable nanoparticles for drug and gene delivery to cells and tissue. *Adv. Drug Delivery Rev.* **2012**, 64, 61-71.

(87) Brigger, I.; Dubernet, C.; Couvreur, P. Nanoparticles in cancer therapy and diagnosis. *Adv. Drug Delivery Rev.* **2012**, 64, 24-36.

(88) Mura, S.; Nicolas, J.; Couvreur, P. Stimuli-responsive nanocarriers for drug delivery. *Nat. Mater.* **2013**, 12, (11), 991-1003.

(89) Min, K. H.; Kim, J. H.; Bae, S. M.; Shin, H.; Kim, M. S.; Park, S.; Lee, H.; Park, R. W.; Kim, I. S.; Kim, K.; Kwon, I. C.; Jeong, S. Y.; Lee, D. S. Tumoral acidic pH-responsive MPEG-poly(beta-amino ester) polymeric micelles for cancer targeting therapy. *J. Controlled Release* **2010**, 144, (2), 259-266.

(90) Mindell, J. A. Lysosomal acidification mechanisms. *Annu. Rev. Physiol.* **2012**, 74, 69-86.

(91) Saisyo, A.; Nakamura, H.; Fang, J.; Tsukigawa, K.; Greish, K.; Furukawa, H.; Maeda, H. pH-sensitive polymeric cisplatin-ion complex with styrene-maleic acid copolymer exhibits tumor-

selective drug delivery and antitumor activity as a result of the enhanced permeability and retention effect. *Colloids Surf., B* **2016**, 138, 128-137.

(92) Fernando, I. R.; Ferris, D. P.; Frasconi, M.; Malin, D.; Strekalova, E.; Yilmaz, M. D.; Ambrogio, M. W.; Algaradah, M. M.; Hong, M. P.; Chen, X.; Nassar, M. S.; Botros, Y. Y.; Cryns, V. L.; Stoddart, J. F. Esterase- and pH-responsive poly(beta-amino ester)-capped mesoporous silica nanoparticles for drug delivery. *Nanoscale* **2015**, 7, (16), 7178-7183.

(93) Hu, J.; He, J.; Cao, D.; Zhang, M.; Ni, P. Core cross-linked polyphosphoester micelles with folate-targeted and acid-cleavable features for pH-triggered drug delivery. *Polym. Chem.* **2015**, 6, (17), 3205-3216.

(94) Deng, Z.; Zhen, Z.; Hu, X.; Wu, S.; Xu, Z.; Chu, P. K. Hollow chitosan-silica nanospheres as pH-sensitive targeted delivery carriers in breast cancer therapy. *Biomaterials* **2011**, 32, (21), 4976-4986.

(95) Yadavalli, T.; Ramasamy, S.; Chandrasekaran, G.; Michael, I.; Therese, H. A.; Chennakesavulu, R. Dual responsive PNIPAM–chitosan targeted magnetic nanopolymers for targeted drug delivery. *J. Magn. Magn. Mater.* **2015**, 380, 315-320.

(96) Shen, Z. Y.; Ma, G. H.; Dobashi, T.; Maki, Y.; Su, Z. G. Preparation and characterization of thermo-responsive albumin nanospheres. *Int. J. Pharm.* **2008**, 346, (1-2), 133-142.

(97) Han, H. D.; Choi, M. S.; Hwang, T.; Song, C. K.; Seong, H.; Kim, T. W.; Choi, H. S.; Shin, B. C. Hyperthermia-induced antitumor activity of thermosensitive polymer modified temperature-sensitive liposomes. *J. Pharm. Sci.* **2006**, 95, (9), 1909-1917.

(98) Zintchenko, A.; Ogris, M.; Wagner, E. Temperature Dependent Gene Expression Induced by PNIPAM-Based Copolymers: Potential of Hyperthermia in Gene Transfer. *Bioconjugate Chem.* **2006**, 17, (3), 766-772.

(99) Kakwere, H.; Leal, M. P.; Materia, M. E.; Curcio, A.; Guardia, P.; Niculaes, D.; Marotta, R.; Falqui, A.; Pellegrino, T. Functionalization of strongly interacting magnetic nanocubes with (thermo)responsive coating and their application in hyperthermia and heat-triggered drug delivery. *ACS Appl. Mater. Interfaces* **2015**, 7, (19), 10132-10145.

(100) Cheng, X.; Jin, Y.; Sun, T.; Qi, R.; Fan, B.; Li, H. Oxidation- and thermo-responsive poly(N-isopropylacrylamide-co-2-hydroxyethyl acrylate) hydrogels cross-linked via diselenides for controlled drug delivery. *RSC Adv.* **2015**, 5, (6), 4162-4170.

(101) Liu, N.; Li, B.; Gong, C.; Liu, Y.; Wang, Y.; Wu, G. A pH- and thermo-responsive poly(amino acid)-based drug delivery system. *Colloids Surf., B* **2015**, 136, 562-569.

(102) Hervault, A.; Dunn, A. E.; Lim, M.; Boyer, C.; Mott, D.; Maenosono, S.; Thanh, N. T. Doxorubicin loaded dual pH- and thermo-responsive magnetic nanocarrier for combined magnetic hyperthermia and targeted controlled drug delivery applications. *Nanoscale* **2016**.

(103) Grull, H.; Langereis, S. Hyperthermia-triggered drug delivery from temperature-sensitive liposomes using MRI-guided high intensity focused ultrasound. *J. Controlled Release* **2012**, 161, (2), 317-327.

(104) Wang, Y. C.; Li, Y.; Sun, T. M.; Xiong, M. H.; Wu, J.; Yang, Y. Y.; Wang, J. Core-shell-corona micelle stabilized by reversible cross-linkage for intracellular drug delivery. *Macromol. Rapid Commun.* **2010**, 31, (13), 1201-1206.

(105) Li, Y.; Xiao, K.; Luo, J.; Xiao, W.; Lee, J. S.; Gonik, A. M.; Kato, J.; Dong, T. A.; Lam, K. S. Well-defined, reversible disulfide cross-linked micelles for on-demand paclitaxel delivery. *Biomaterials* **2011**, 32, (27), 6633-6645.

(106) Koo, A. N.; Lee, H. J.; Kim, S. E.; Chang, J. H.; Park, C.; Kim, C.; Park, J. H.; Lee, S. C. Disulfide-cross-linked PEG-poly(amino acid)s copolymer micelles for glutathione-mediated intracellular drug delivery. *Chem. Commun. (Cambridge, U. K.)* **2008**, (48), 6570-6572.

(107) Kato, J.; Li, Y.; Xiao, K.; Lee, J. S.; Luo, J.; Tuscano, J. M.; O'Donnell, R. T.; Lam, K. S. Disulfide cross-linked micelles for the targeted delivery of vincristine to B-cell lymphoma. *Mol. Pharm.* **2012**, 9, (6), 1727-1735.

(108) Gosselin, M. A.; Guo, W.; Lee, R. J. Efficient Gene Transfer Using Reversibly Cross-Linked Low Molecular Weight Polyethylenimine. *Bioconjugate Chem.* **2001**, 12, (6), 989-994.

(109) Wu, W.; Yao, W.; Wang, X.; Xie, C.; Zhang, J.; Jiang, X. Bioreducible heparin-based nanogel drug delivery system. *Biomaterials* **2015**, 39, 260-268.

(110) Xiao, D.; Jia, H. Z.; Ma, N.; Zhuo, R. X.; Zhang, X. Z. A redox-responsive mesoporous silica nanoparticle capped with amphiphilic peptides by self-assembly for cancer targeting drug delivery. *Nanoscale* **2015**, 7, (22), 10071-10077.

(111) Fomina, N.; Sankaranarayanan, J.; Almutairi, A. Photochemical mechanisms of light-triggered release from nanocarriers. *Adv. Drug Delivery Rev.* **2012**, 64, (11), 1005-1020.

(112) Lu, J.; Choi, E.; Tamanoi, F.; Zink, J. I. Light-activated nanoimpeller-controlled drug release in cancer cells. *Small* **2008**, 4, (4), 421-426.

(113) Yuan, Q.; Zhang, Y.; Chen, T.; Lu, D.; Zhao, Z.; Zhang, X.; Li, Z.; Yan, C.-H.; Tan, W. Photon-Manipulated Drug Release from a Mesoporous Nanocontainer Controlled by Azobenzene-Modified Nucleic Acid. *ACS Nano* **2012**, 6, (7), 6337-6344.

(114) Mei, X.; Yang, S.; Chen, D.; Li, N.; Li, H.; Xu, Q.; Ge, J.; Lu, J. Light-triggered reversible assemblies of azobenzene-containing amphiphilic copolymer with beta-cyclodextrin-modified hollow mesoporous silica nanoparticles for controlled drug release. *Chem. Commun. (Cambridge, U. K.)* **2012**, 48, (80), 10010-10012.

(115) Ipe, B. I.; Mahima, S.; Thomas, K. G. Light-Induced Modulation of Self-Assembly on Spiropyran-Capped Gold Nanoparticles: A Potential System for the Controlled Release of Amino Acid Derivatives. *J. Am. Chem. Soc.* **2003**, 125, (24), 7174-7175.

(116) He, D.; He, X.; Wang, K.; Cao, J.; Zhao, Y. A light-responsive reversible molecule-gated system using thymine-modified mesoporous silica nanoparticles. *Langmuir* **2012**, 28, (8), 4003-4008.

(117) Liu, J.; Detrembleur, C.; De Pauw-Gillet, M. C.; Mornet, S.; Jerome, C.; Duguet, E. Gold nanorods coated with mesoporous silica shell as drug delivery system for remote near infrared light-activated release and potential phototherapy. *Small* **2015**, 11, (19), 2323-2332.

(118) Li, H.; Tan, L.-L.; Jia, P.; Li, Q.-L.; Sun, Y.-L.; Zhang, J.; Ning, Y.-Q.; Yu, J.; Yang, Y.-W. Near-infrared light-responsive supramolecular nanovalve based on mesoporous silica-coated gold nanorods. *Chem. Sci.* **2014**, 5, (7), 2804.

(119) Barhoumi, A.; Huschka, R.; Bardhan, R.; Knight, M. W.; Halas, N. J. Light-induced release of DNA from plasmon-resonant nanoparticles: Towards light-controlled gene therapy. *Chem. Phys. Lett.* **2009**, 482, (4-6), 171-179.

(120) Huang, J.; Jackson, K. S.; Murphy, C. J. Polyelectrolyte wrapping layers control rates of photothermal molecular release from gold nanorods. *Nano Lett.* **2012**, 12, (6), 2982-2987.

(121) Rajpal; Mann, A.; Khanduri, R.; Naik, R. J.; Ganguli, M. Structural rearrangements and chemical modifications in known cell penetrating peptide strongly enhance DNA delivery efficiency. *J. Controlled Release* **2012**, 157, (2), 260-271.

(122) Guo, X. D.; Wiradharma, N.; Liu, S. Q.; Zhang, L. J.; Khan, M.; Qian, Y.; Yang, Y. Y. Oligomerized alpha-helical KALA peptides with pendant arms bearing cell-adhesion, DNA-binding and endosome-buffering domains as efficient gene transfection vectors. *Biomaterials* **2012**, 33, (26), 6284-6291.

(123) Chen, J. X.; Xu, X. D.; Yang, S.; Yang, J.; Zhuo, R. X.; Zhang, X. Z. Self-assembled BolA-like amphiphilic peptides as viral-mimetic gene vectors for cancer cell targeted gene delivery. *Macromol. Biosci.* **2013**, 13, (1), 84-92.

(124) Föst, C.; Duwe, F.; Hellriegel, M.; Schweyer, S.; Emons, G.; Gründker, C. Targeted chemotherapy for triple-negative breast cancers via LHRH receptor. *Oncol. Rep.* **2011**, 25, 1481-1487.

(125) Gu, J.; Wang, X.; Jiang, X.; Chen, Y.; Chen, L.; Fang, X.; Sha, X. Self-assembled carboxymethyl poly (L-histidine) coated poly (β-amino ester)/DNA complexes for gene transfection. *Biomaterials* **2012**, 33, (2), 644-658.

(126) Zeng, H.; Little, H. C.; Tiambeng, T. N.; Williams, G. A.; Guan, Z. Multifunctional Dendronized Peptide Polymer Platform for Safe and Effective siRNA Delivery. *J. Am. Chem. Soc.* **2013**.

(127) Deshayes, S.; Morris, M. C.; Divita, G.; Heitz, F. Cell-penetrating peptides: tools for intracellular delivery of therapeutics. *Cell. Mol. Life Sci.* **2005**, 62, (16), 1839-1849.

(128) Lee, Y.; Kataoka, K. Delivery of Nucleic Acid Drugs. *Adv. Polym. Sci.* **2012**, 249, 95-134.

(129) Gao, Y.; Chen, L.; Zhang, Z.; Chen, Y.; Li, Y. Reversal of multidrug resistance by reduction-sensitive linear cationic click polymer/iMDR1-pDNA complex nanoparticles. *Biomaterials* **2011**, 32, (6), 1738-1747.

(130) Benoit, D. S.; Boutin, M. E. Controlling mesenchymal stem cell gene expression using polymer-mediated delivery of siRNA. *Biomacromolecules* **2012**, 13, (11), 3841-3849.

(131) Zou, L.; Song, X.; Yi, T.; Li, S.; Deng, H.; Chen, X.; Li, Z.; Bai, Y.; Zhong, Q.; Wei, Y.; Zhao, X. Administration of PLGA nanoparticles carrying shRNA against focal adhesion kinase and CD44 results in enhanced antitumor effects against ovarian cancer. *Cancer Gene Ther.* **2013**, 20, (4), 242-250.

(132) Zhang, J.; Lei, Y.; Dhaliwal, A.; Ng, Q. K.; Du, J.; Yan, M.; Lu, Y.; Segura, T. Protein-polymer nanoparticles for nonviral gene delivery. *Biomacromolecules* **2011**, 12, (4), 1006-1014.

(133) Kang, S. W.; Lim, H. W.; Seo, S. W.; Jeon, O.; Lee, M.; Kim, B. S. Nanosphere-mediated delivery of vascular endothelial growth factor gene for therapeutic angiogenesis in mouse ischemic limbs. *Biomaterials* **2008**, 29, (8), 1109-1117.

(134) Wilson, D. S.; Dalmasso, G.; Wang, L.; Sitaraman, S. V.; Merlin, D.; Murthy, N. Orally delivered thioketal nanoparticles loaded with TNF-alpha-siRNA target inflammation and inhibit gene expression in the intestines. *Nat. Mater.* **2010**, 9, (11), 923-928.

(135) Kole, R.; Krainer, A. R.; Altman, S. RNA therapeutics: beyond RNA interference and antisense oligonucleotides. *Nat. Rev. Drug Discovery* **2012**, 11, (2), 125-140.

(136) Ming, X.; Laing, B. Bioconjugates for targeted delivery of therapeutic oligonucleotides. *Adv. Drug Delivery Rev.* **2015**, 87, 81-89.

(137) Järver, P.; Coursindel, T.; Andaloussi, S. E.; Godfrey, C.; Wood, M. J.; Gait, M. J. Peptide-mediated Cell and In Vivo Delivery of Antisense Oligonucleotides and siRNA. *Mol. Ther. Nucleic Acids* **2012**, 1, e27.

(138) Wu, G.-S.; Lu, J.-J.; Guo, J.-J.; Huang, M.-Q.; Gan, L.; Chen, X.-P.; Wang, Y.-T. Synergistic anti-cancer activity of the combination of dihydroartemisinin and doxorubicin in breast cancer cells. *Pharmacol. Rep.* **2013**, 65, (2), 453-459.

(139) Nagaprashantha, L. D.; Vatsyayan, R.; Singhal, J.; Fast, S.; Roby, R.; Awasthi, S.; Singhal, S. S. Anti-cancer effects of novel flavonoid vicenin-2 as a single agent and in synergistic combination with docetaxel in prostate cancer. *Biochem. Pharmacol.* **2011**, 82, (9), 1100-1109.

(140) Hossain, M.; Banik, N. L.; Ray, S. K. Synergistic anti-cancer mechanisms of curcumin and paclitaxel for growth inhibition of human brain tumor stem cells and LN18 and U138MG cells. *Neurochem. Int.* **2012**, 61, (7), 1102-1113.

(141) Dai, X.; Tan, C. Combination of microRNA therapeutics with small-molecule anticancer drugs: mechanism of action and co-delivery nanocarriers. *Adv. Drug Delivery Rev.* **2015**, 81, 184-197.

(142) Takahashi, R.; Sato, T.; Klinman, D. M.; Shimosato, T.; Kaneko, T.; Ishigatsubo, Y. Suppressive oligodeoxynucleotides synergistically enhance antiproliferative effects of anticancer drugs in A549 human lung cancer cells. *Int. J. Oncol.* **2013**, 42, (2), 429-436.

(143) Yang, Z.; Gao, D.; Cao, Z.; Zhang, C.; Cheng, D.; Liu, J.; Shuai, X. Drug and gene co-delivery systems for cancer treatment. *Biomater. Sci.* **2015**, 3, (7), 1035-1049.

(144) Wiradharma, N.; Tong, Y. W.; Yang, Y.-Y. Self-assembled oligopeptide nanostructures for co-delivery of drug and gene with synergistic therapeutic effect. *Biomaterials* **2009**, 30, (17), 3100-3109.

(145) Liang, J.; Wu, W. L.; Xu, X. D.; Zhuo, R. X.; Zhang, X. Z. pH Responsive micelle self-assembled from a new amphiphilic peptide as anti-tumor drug carrier. *Colloids Surf., B* **2014**, 114, 398-403.

(146) Rad-Malekshahi, M.; Visscher, K. M.; Rodrigues, J. P.; de Vries, R.; Hennink, W. E.; Baldus, M.; Bonvin, A. M.; Mastrobattista, E.; Weingarth, M. The Supramolecular Organization of a Peptide-Based Nanocarrier at High Molecular Detail. *J. Am. Chem. Soc.* **2015**, 137, (24), 7775-7784.

(147) van Hell, A. J.; Klymchenko, A.; Burgers, P. P.; Moret, E. E.; Jiskoot, W.; Hennink, W. E.; Crommelin, D. J. A.; Mastrobattista, E. Conformation and Intermolecular Interactions of SA2 Peptides Self-Assembled into Vesicles. *J. Phys. Chem. B* **2010**, 114, (34), 11046-11052.

(148) Schuster, T. B.; de Bruyn Ouboter, D.; Palivan, C. G.; Meier, W. From fibers to micelles using point-mutated amphiphilic peptides. *Langmuir* **2011**, 27, (8), 4578-4584.

(149) Korevaar, P. A.; Newcomb, C. J.; Meijer, E. W.; Stupp, S. I. Pathway selection in peptide amphiphile assembly. *J. Am. Chem. Soc.* **2014**, 136, (24), 8540-8543.

(150) L. Villaraza, A. J.; Bumb, A.; Brechbiel, M. W. Macromolecules, Dendrimers, and Nanomaterials in Magnetic Resonance Imaging: The Interplay between Size, Function, and Pharmacokinetics. *Chem. Rev. (Washington, DC, U. S.)* **2010**, 110, (5), 2921-2959.

(151) Werner, E. J.; Datta, A.; Jocher, C. J.; Raymond, K. N. High-relaxivity MRI contrast agents: where coordination chemistry meets medical imaging. *Angew. Chem., Int. Ed.* **2008**, 47, (45), 8568-8580.

(152) Pierre, V. C.; Allen, M. J.; Caravan, P. Contrast agents for MRI: 30+ years and where are we going? *J. Biol. Inorg. Chem.* **2014**, 19, (2), 127-131.

(153) Solomon, I.; Bloembergen, N. Nuclear Magnetic Interactions in the HF Molecule. *J. Chem. Phys.* **1956**, 25, (2), 261-266.

(154) Solomon, I. Relaxation Processes in a System of Two Spins. *Phys. Rev.* **1955**, 99, (2), 559-565.

(155) Bloembergen, N.; Morgan, L. O. Proton Relaxation Times in Paramagnetic Solutions. Effects of Electron Spin Relaxation. *J. Chem. Phys.* **1961**, 34, (3), 842-850.

(156) Bloembergen, N. Spin Relaxation Processes in a Two-Proton System. *Phys. Rev.* **1956**, 104, (6), 1542-1547.

(157) Bloembergen, N. Proton Relaxation Times in Paramagnetic Solutions. *J. Chem. Phys.* **1957**, 27, (2), 572-573.

(158) Caravan, P.; Ellison, J. J.; McMurry, T. J.; Lauffer, R. B. Gadolinium (III) chelates as MRI contrast agents: structure, dynamics, and applications. *Chem. Rev. (Washington, DC, U. S.)* **1999**, 99, (9), 2293-2352.

(159) Lauffer, R. B.; Brady, T. J. Preparation and water relaxation properties of proteins labeled with paramagnetic metal chelates. *Magn. Reson. Imaging* **1985**, 3, (1), 11-16.

(160) Lauffer, R. B.; Brady, T. J.; Brown, R. D.; Baglin, C.; Koenig, S. H. 1/T1 NMRD Profiles of Solutions of Mn2+ and Gd3+ Protein–Chelate Conjugates. *Magn. Reson. Med.* **1986**, 3, (4), 541-548.

(161) Wiener, E.; Brechbiel, M. W.; Brothers, H.; Magin, R. L.; Gansow, O. A.; Tomalia, D. A.; Lauterbur, P. C. Dendrimer-based metal chelates: A new class of magnetic resonance imaging contrast agents. *Magn. Reson. Med.* **1994**, 31, (1), 1-8.

(162) Armitage, F. E.; Richardson, D. E.; Li, K. C. P. Polymeric contrast agents for magnetic resonance imaging: synthesis and characterization of gadolinium diethylenetriaminepentaacetic acid conjugated to polysaccharides. *Bioconjugate Chem.* **1990**, 1, (6), 365-374.

(163) Kobayashi, H.; Brechbiel, M. W. Nano-sized MRI contrast agents with dendrimer cores. *Adv. Drug Delivery Rev.* **2005**, 57, (15), 2271-2286.

(164) Langereis, S.; de Lussanet, Q. G.; van Genderen, M. H. P.; Backes, W. H.; Meijer, E. W. Multivalent Contrast Agents Based on Gadolinium-Diethylenetriaminepentaacetic Acid-Terminated Poly(propylene imine) Dendrimers for Magnetic Resonance Imaging. *Macromolecules* **2004**, 37, (9), 3084-3091.

(165) Doble, D. M. J.; Botta, M.; Wang, J.; Aime, S.; Barge, A.; Raymond, K. N. Optimization of the Relaxivity of MRI Contrast Agents: Effect of Poly(ethylene glycol) Chains on the Water-Exchange Rates of Gd(III) Complexes. *J. Am. Chem. Soc.* **2001**, 123, (43), 10758-10759.

(166) Tang, J.; Sheng, Y.; Hu, H.; Shen, Y. Macromolecular MRI contrast agents: Structures, properties and applications. *Prog. Polym. Sci.* **2013**, 38, (3-4), 462-502.

(167) Zhelev, Z.; Gadjeva, V.; Aoki, I.; Bakalova, R.; Saga, T. Cell-penetrating nitroxides as molecular sensors for imaging of cancer in vivo, based on tissue redox activity. *Mol. BioSyst.* **2012**, 8, (10), 2733-2740.

(168) Loving, G. S.; Mukherjee, S.; Caravan, P. Redox-activated manganese-based MR contrast agent. *J. Am. Chem. Soc.* **2013**, 135, (12), 4620-4623.

(169) Iwaki, S.; Hanaoka, K.; Piao, W.; Komatsu, T.; Ueno, T.; Terai, T.; Nagano, T. Development of hypoxia-sensitive Gd3+-based MRI contrast agents. *Bioorg. Med. Chem. Lett.* **2012**, 22, (8), 2798-2802.

(170) Raghunand, N.; Jagadish, B.; Trouard, T. P.; Galons, J. P.; Gillies, R. J.; Mash, E. A. Redox-sensitive contrast agents for MRI based on reversible binding of thiols to serum albumin. *Magn. Reson. Med.* **2006**, 55, (6), 1272-1280.

(171) Torres, E.; Mainini, F.; Napolitano, R.; Fedeli, F.; Cavalli, R.; Aime, S.; Terreno, E. Improved paramagnetic liposomes for MRI visualization of pH triggered release. *J. Controlled Release* **2011**, 154, (2), 196-202.

(172) Kim, K. S.; Park, W.; Hu, J.; Bae, Y. H.; Na, K. A cancer-recognizable MRI contrast agents using pH-responsive polymeric micelle. *Biomaterials* **2014**, 35, (1), 337-343.

(173) Merrifield, R. B. Solid Phase Peptide Synthesis. I. The Synthesis of a Tetrapeptide. *J. Am. Chem. Soc.* **1963**, 85, (14), 2149-2154.

(174) Mergler, M.; Durieux, J. P., *The Bachem Practice of SPPS*. 2nd edition ed.; Bachem AG: Bubendorf, 2005.

(175) Shelton, P.; Jensen, K., Linkers, Resins, and General Procedures for Solid-Phase Peptide Synthesis. In *Peptide Synthesis and Applications*, Jensen, K. J.; Tofteng Shelton, P.; Pedersen, S. L., Eds. Humana Press: 2013; Vol. 1047, pp 23-41.

(176) Chantell, C. A.; Onaiyekan, M. A.; Menakuru, M. Fast conventional Fmoc solid-phase peptide synthesis: a comparative study of different activators. *J. Pept. Sci.* **2012**, 18, (2), 88-91.

(177) Daniel, M.-C.; Astruc, D. Gold Nanoparticles: Assembly, Supramolecular Chemistry, Quantum-Size-Related Properties, and Applications toward Biology, Catalysis, and Nanotechnology. *Chem. Rev. (Washington, DC, U. S.)* **2004**, 104, (1), 293-346.

(178) Giljohann, D. A.; Seferos, D. S.; Daniel, W. L.; Massich, M. D.; Patel, P. C.; Mirkin, C. A. Gold Nanoparticles for Biology and Medicine. *Angew. Chem., Int. Ed.* **2010**, 49, (19), 3280-3294.

(179) Lecommandoux, S.; Sandre, O.; Chécot, F.; Rodriguez-Hernandez, J.; Perzynski, R. Magnetic Nanocomposite Micelles and Vesicles. *Adv. Mater. (Weinheim, Ger.)* **2005**, 17, (6), 712-718.

(180) Willner, I.; Basnar, B.; Willner, B. Nanoparticle-enzyme hybrid systems for nanobiotechnology. *FEBS J.* **2007**, 274, (2), 302-309.

(181) Sperling, R. A.; Parak, W. J. Surface modification, functionalization and bioconjugation of colloidal inorganic nanoparticles. *Philos. Trans. R. Soc., A* **2010**, 368, (1915), 1333-1383.

(182) Sotiriou, G. A.; Schneider, M.; Pratsinis, S. E. Color-Tunable Nanophosphors by Codoping Flame-Made Y2O3 with Tb and Eu. *J. Phys. Chem. C* **2011**, 115, (4), 1084-1089.

(183) Uchida, M.; Terashima, M.; Cunningham, C. H.; Suzuki, Y.; Willits, D. A.; Willis, A. F.; Yang, P. C.; Tsao, P. S.; McConnell, M. V.; Young, M. J.; Douglas, T. A human ferritin iron oxide nano-composite magnetic resonance contrast agent. *Magn. Reson. Med.* **2008**, 60, (5), 1073-1081.

(184) Masotti, A.; Pitta, A.; Ortaggi, G.; Corti, M.; Innocenti, C.; Lascialfari, A.; Marinone, M.; Marzola, P.; Daducci, A.; Sbarbati, A.; Micotti, E.; Orsini, F.; Poletti, G.; Sangregorio, C. Synthesis and characterization of polyethylenimine-based iron oxide composites as novel contrast agents for MRI. *Magn. Reson. Mater. Phys., Biol. Med.* **2009**, 22, (2), 77-87.

(185) Lutz, J.-F.; Boerner, H. G. Modern trends in polymer bio-conjugates design. *Prog. Polym. Sci.* **2008**, 33, (1), 1-39.

(186) Stupp, S. I. Self-Assembly and Biomaterials. *Nano Lett.* **2010**, 10, (12), 4783-4786.

(187) Webber, M. J.; Tongers, J. r.; Newcomb, C. J.; Marquardt, K.-T.; Bauersachs, J.; Losordo, D. W.; Stupp, S. I. Supramolecular nanostructures that mimic VEGF as a strategy for ischemic tissue repair. *Proc. Natl. Acad. Sci. U. S. A.* **2011**, 108, (33), 13438-13443.

(188) Holowka, E. P.; Sun, V. Z.; Kamei, D. T.; Deming, T. J. Polyarginine segments in block copolypeptides drive both vesicular assembly and intracellular delivery. *Nat. Mater.* **2007**, 6, (1), 52-57.

(189) Hegarty, M. Toxic amino acids in foods of animals and man. *Proc. Nutr. Soc. Aust.* **1986**, 11.

(190) Zhou, Z. Y.; Shi, G. Q.; Fontaine, R.; Wei, K.; Feng, T.; Wang, F.; Wang, G. Q.; Qu, Y.; Li, Z. H.; Dong, Z. J.; Zhu, H. J.; Yang, Z. L.; Zeng, G.; Liu, J. K. Evidence for the natural toxins from the mushroom Trogia venenata as a cause of sudden unexpected death in Yunnan Province, China. *Angew. Chem., Int. Ed.* **2012**, 51, (10), 2368-2370.

(191) Lévy, R. Peptide-capped gold nanoparticles: towards artificial proteins. *ChemBioChem* **2006**, 7, (8), 1141-1145.

(192) Aili, D.; Enander, K.; Baltzer, L.; Liedberg, B. Assembly of Polypeptide-Functionalized Gold Nanoparticles through a Heteroassociation- and Folding-Dependent Bridging. *Nano Lett.* **2008**, 8, (8), 2473-2478.

(193) Kim, J.; Sadowsky, M. J.; Hur, H. G. Simultaneous synthesis of temperature-tunable peptide and gold nanoparticle hybrid spheres. *Biomacromolecules* **2011**, 12, (7), 2518-2523.

(194) Song, C.; Zhao, G.; Zhang, P.; Rosi, N. L. Expeditious Synthesis and Assembly of Sub-100 nm Hollow Spherical Gold Nanoparticle Superstructures. *J. Am. Chem. Soc.* **2010**, 132, (40), 14033-14035.

(195) Wallace, B. A. Recent advances in the high resolution structures of bacterial channels: gramicidin A. *J. Struct. Biol.* **1998**, 121, (2), 123-141.

(196) Weiss Emily, A.; Kaufman George, K.; Kriebel Jennah, K.; Li, Z.; Schalek, R.; Whitesides George, M. Si/SiO2-templated formation of ultraflat metal surfaces on glass, polymer, and solder supports: their use as substrates for self-assembled monolayers. *Langmuir* **2007**, 23, (19), 9686-9694.

(197) Lavoie, H.; Blaudez, D.; Vaknin, D.; Desbat, B.; Ocko, B. M.; Salesse, C. eSpectroscopic and structural properties of valine gramicidin A in monolayers at the air-water interface. *Biophys. J.* **2002**, 83, (6), 3558-3569.

(198) Miura, Y.; Kimura, S.; Imanishi, Y.; Umemura, J. Formation of Oriented Helical Peptide Layers on a Gold Surface Due to the Self-Assembling Properties of Peptides. *Langmuir* **1998**, 14, (24), 6935-6940.

(199) Love, J. C.; Estroff, L. A.; Kriebel, J. K.; Nuzzo, R. G.; Whitesides, G. M. Self-Assembled Monolayers of Thiolates on Metals as a Form of Nanotechnology. *Chem. Rev. (Washington, DC, U. S.)* **2005**, 105, (4), 1103-1169.

(200) Jackson, M.; Mantsch, H. H. The use and misuse of FTIR spectroscopy in the determination of protein structure. *Crit. Rev. Biochem. Mol. Biol.* **1995**, 30, (2), 95-120.

(201) Wallace, B. A. Structure of gramicidin A. *Biophys. J.* **1986**, 49, (1), 295-306.

(202) Ulrich, W. P.; Vogel, H. Polarization-modulated FTIR spectroscopy of lipid/gramicidin monolayers at the air/water interface. *Biophys. J.* **1999**, 76, (3), 1639-1647.

(203) Kopple, K. D.; Go, A.; Schamper, T. J. Conformation of cyclic peptides. 10. Conformational averaging in peptides with the sequence cyclo-(Gly-D-Xxx-L-Yyy)2. *J. Am. Chem. Soc.* **1978**, 100, (13), 4289-4295.

(204) Gowda, R.; Jones, N. R.; Banerjee, S.; Robertson, G. P. Use of Nanotechnology to Develop Multi-Drug Inhibitors For Cancer Therapy. *J. Nanomed. Nanotechnol.* **2013**, 4, (6), 184.

(205) Allen, T. M.; Cullis, P. R. Drug delivery systems: entering the mainstream. *Science* **2004**, 303, (5665), 1818-1822.

(206) Krishna, R.; Mayer, L. D. Multidrug resistance (MDR) in cancer: Mechanisms, reversal using modulators of MDR and the role of MDR modulators in influencing the pharmacokinetics of anticancer drugs. *Eur. J. Pharm. Sci.* **2000**, 11, (4), 265-283.

(207) Abbasi, M.; Lavasanifar, A.; Uludag, H. Recent attempts at RNAi-mediated P-glycoprotein downregulation for reversal of multidrug resistance in cancer. *Med. Res. Rev.* **2013**, 33, (1), 33-53.

(208) Doane, T.; Burda, C. Nanoparticle mediated non-covalent drug delivery. *Adv. Drug Delivery Rev.* **2013**, 65, (5), 607-621.

(209) Yu, Y. H.; Kim, E.; Park, D. E.; Shim, G.; Lee, S.; Kim, Y. B.; Kim, C. W.; Oh, Y. K. Cationic solid lipid nanoparticles for co-delivery of paclitaxel and siRNA. *Eur. J. Pharm. Biopharm.* **2012**, 80, (2), 268-273.

(210) Sun, X.; Pang, Z.; Ye, H.; Qiu, B.; Guo, L.; Li, J.; Ren, J.; Qian, Y.; Zhang, Q.; Chen, J.; Jiang, X. Co-delivery of pEGFP-hTRAIL and paclitaxel to brain glioma mediated by an angiopep-conjugated liposome. *Biomaterials* **2012**, 33, (3), 916-924.

(211) Cheng, D.; Cao, N.; Chen, J.; Yu, X.; Shuai, X. Multifunctional nanocarrier mediated co-delivery of doxorubicin and siRNA for synergistic enhancement of glioma apoptosis in rat. *Biomaterials* **2012**, 33, (4), 1170-1179.

(212) Zhu, C.; Jung, S.; Luo, S.; Meng, F.; Zhu, X.; Park, T. G.; Zhong, Z. Co-delivery of siRNA and paclitaxel into cancer cells by biodegradable cationic micelles based on PDMAEMA–PCL–PDMAEMA triblock copolymers. *Biomaterials* **2010**, 31, (8), 2408-2416.

(213) Zhao, X.; Li, F.; Li, Y.; Wang, H.; Ren, H.; Chen, J.; Nie, G.; Hao, J. Co-delivery of HIF1alpha siRNA and gemcitabine via biocompatible lipid-polymer hybrid nanoparticles for effective treatment of pancreatic cancer. *Biomaterials* **2015**, 46, 13-25.

(214) Chu, D.; Xu, W.; Pan, R.; Chen, P. Co-delivery of drug nanoparticles and siRNA mediated by a modified cell penetrating peptide for inhibiting cancer cell proliferation. *RSC Adv.* **2015**, 5, (26), 20554-20556.

(215) Jia, H. Z.; Zhang, W.; Zhu, J. Y.; Yang, B.; Chen, S.; Chen, G.; Zhao, Y. F.; Feng, J.; Zhang, X. Z. Hyperbranched-hyperbranched polymeric nanoassembly to mediate controllable co-delivery of siRNA and drug for synergistic tumor therapy. *J. Controlled Release* **2015**, 216, 9-17.

(216) Xiong, X.-B.; Lavasanifar, A. Traceable Multifunctional Micellar Nanocarriers for Cancer-Targeted Co-delivery of MDR-1 siRNA and Doxorubicin. *ACS Nano* **2011**, 5, (6), 5202-5213.

(217) Liu, S.; Guo, Y.; Huang, R.; Li, J.; Huang, S.; Kuang, Y.; Han, L.; Jiang, C. Gene and doxorubicin co-delivery system for targeting therapy of glioma. *Biomaterials* **2012**, 33, (19), 4907-4916.

(218) Liu, C.; Liu, F.; Feng, L.; Li, M.; Zhang, J.; Zhang, N. The targeted co-delivery of DNA and doxorubicin to tumor cells via multifunctional PEI-PEG based nanoparticles. *Biomaterials* **2013**, 34, (10), 2547-2564.

(219) Yin, T.; Wang, L.; Yin, L.; Zhou, J.; Huo, M. Co-delivery of hydrophobic paclitaxel and hydrophilic AURKA specific siRNA by redox-sensitive micelles for effective treatment of breast cancer. *Biomaterials* **2015**, 61, 10-25.

(220) Gaspar, V. M.; Baril, P.; Costa, E. C.; de Melo-Diogo, D.; Foucher, F.; Queiroz, J. A.; Sousa, F.; Pichon, C.; Correia, I. J. Bioreducible poly(2-ethyl-2-oxazoline)-PLA-PEI-SS triblock copolymer micelles for co-delivery of DNA minicircles and Doxorubicin. *J. Controlled Release* **2015**, 213, 175-191.

(221) Wang, K.; Hu, Q.; Zhu, W.; Zhao, M.; Ping, Y.; Tang, G. Structure-Invertible Nanoparticles for Triggered Co-Delivery of Nucleic Acids and Hydrophobic Drugs for Combination Cancer Therapy. *Adv. Funct. Mater.* **2015**, 25, (22), 3380-3392.

(222) Han, L.; Tang, C.; Yin, C. Dual-targeting and pH/redox-responsive multi-layered nanocomplexes for smart co-delivery of doxorubicin and siRNA. *Biomaterials* **2015**, 60, 42-52.

(223) Shera, J. N.; Sun, X. S. Effect of Peptide Sequence on Surface Properties and Self-Assembly of an Amphiphilic pH-Responsive Peptide. *Biomacromolecules* **2009**, 10, (9), 2446-2450.

(224) Han, K.; Chen, S.; Chen, W. H.; Lei, Q.; Liu, Y.; Zhuo, R. X.; Zhang, X. Z. Synergistic gene and drug tumor therapy using a chimeric peptide. *Biomaterials* **2013**, 34, (19), 4680-4689.

(225) Mao, L.; Wang, H.; Tan, M.; Ou, L.; Kong, D.; Yang, Z. Conjugation of two complementary anti-cancer drugs confers molecular hydrogels as a co-delivery system. *Chem. Commun. (Cambridge, U. K.)* **2012**, 48, (3), 395-397.

(226) Wiradharma, N.; Tong, Y. W.; Yang, Y.-Y. Design and Evaluation of Peptide Amphiphiles with Different Hydrophobic Blocks for Simultaneous Delivery of Drugs and Genes. *Macromol. Rapid Commun.* **2010**, 31, (13), 1212-1217.

(227) Cruz, C.; Santos, S. D.; Cabrita, E. J.; Queiroz, J. A. Binding analysis between L-histidine immobilized and oligonucleotides by SPR and NMR. *Int. J. Biol. Macromol.* **2013**, 56, 175-180.

(228) Liao, S. M.; Du, Q. S.; Meng, J. Z.; Pang, Z. W.; Huang, R. B. The multiple roles of histidine in protein interactions. *Chem. Cent. J.* **2013**, 7, (1), 44.

(229) Yoshino, J.; Kano, N.; Kawashima, T. Fluorescent azobenzenes and aromatic aldimines featuring an N-B interaction. *Dalton Trans.* **2013**, 42, (45), 15826-15834.

(230) Yue, Z. G.; Wei, W.; Lv, P. P.; Yue, H.; Wang, L. Y.; Su, Z. G.; Ma, G. H. Surface charge affects cellular uptake and intracellular trafficking of chitosan-based nanoparticles. *Biomacromolecules* **2011**, 12, (7), 2440-2446.

(231) Chen, K.; Xu, J.; Luft, J. C.; Tian, S.; Raval, J. S.; DeSimone, J. M. Design of asymmetric particles containing a charged interior and a neutral surface charge: comparative study on in vivo circulation of polyelectrolyte microgels. *J. Am. Chem. Soc.* **2014**, 136, (28), 9947-9952.

(232) Manders, E. M. M.; Verbeek, F. J.; Aten, J. A. Measurement of co-localization of objects in dual-colour confocal images. *J. Microsc. (Oxford, U. K.)* **1993**, 169, (3), 375-382.

(233) Bacia, K.; Kim, S. A.; Schwille, P. Fluorescence cross-correlation spectroscopy in living cells. *Nat. Methods* **2006**, 3, (2), 83-89.

(234) Ramamoorth, M.; Narvekar, A. Non viral vectors in gene therapy- an overview. *J. Clin. Diagn. Res.* **2015**, 9, (1), GE01-06.

(235) Tappertzhofen, K.; Weiser, F.; Montermann, E.; Reske-Kunz, A.; Bros, M.; Zentel, R. Poly-L-Lysine-Poly[HPMA] Block Copolymers Obtained by RAFT Polymerization as Polyplex-Transfection Reagents with Minimal Toxicity. *Macromol. Biosci.* **2015**, 15, (8), 1159-1173.

(236) Chen, S.; Rong, L.; Lei, Q.; Cao, P. X.; Qin, S. Y.; Zheng, D. W.; Jia, H. Z.; Zhu, J. Y.; Cheng, S. X.; Zhuo, R. X.; Zhang, X. Z. A surface charge-switchable and folate modified system for co-delivery of proapoptosis peptide and p53 plasmid in cancer therapy. *Biomaterials* **2016**, 77, 149-163.

(237) Ohsaki, M.; Okuda, T.; Wada, A.; Hirayama, T.; Niidome, T.; Aoyagi, H. In Vitro Gene Transfection Using Dendritic Poly(L-lysine). *Bioconjugate Chem.* **2002**, 13, (3), 510-517.

(238) Neu, M.; Fischer, D.; Kissel, T. Recent advances in rational gene transfer vector design based on poly(ethylene imine) and its derivatives. *J. Gene Med.* **2005**, 7, (8), 992-1009.

(239) Mao, S.; Neu, M.; Germershaus, O.; Merkel, O.; Sitterberg, J.; Bakowsky, U.; Kissel, T. Influence of Polyethylene Glycol Chain Length on the Physicochemical and Biological Properties of Poly(ethylene imine)-graft-Poly(ethylene glycol) Block Copolymer/SiRNA Polyplexes. *Bioconjugate Chem.* **2006**, 17, (5), 1209-1218.

(240) Merdan, T.; Kunath, K.; Petersen, H.; Bakowsky, U.; Voigt, K. H.; Kopecek, J.; Kissel, T. PEGylation of Poly(ethylene imine) Affects Stability of Complexes with Plasmid DNA under in Vivo Conditions in a Dose-Dependent Manner after Intravenous Injection into Mice. *Bioconjugate Chem.* **2005**, 16, (4), 785-792.

(241) Mintzer, M. A.; Simanek, E. E. Nonviral Vectors for Gene Delivery. *Chem. Rev. (Washington, DC, U. S.)* **2009**, 109, (2), 259-302.

(242) Urbiola, K.; Blanco-Fernandez, L.; Navarro, G.; Rodl, W.; Wagner, E.; Ogris, M.; Tros de Ilarduya, C. Evaluation of improved PAMAM-G5 conjugates for gene delivery targeted to the transferrin receptor. *Eur. J. Pharm. Biopharm.* **2015**, 94, 116-122.

(243) Schaeublin, N. M.; Braydich-Stolle, L. K.; Schrand, A. M.; Miller, J. M.; Hutchison, J.; Schlager, J. J.; Hussain, S. M. Surface charge of gold nanoparticles mediates mechanism of toxicity. *Nanoscale* **2011**, 3, (2), 410-420.

(244) Xiao, K.; Li, Y.; Luo, J.; Lee, J. S.; Xiao, W.; Gonik, A. M.; Agarwal, R. G.; Lam, K. S. The effect of surface charge on in vivo biodistribution of PEG-oligocholic acid based micellar nanoparticles. *Biomaterials* **2011**, 32, (13), 3435-3446.

(245) Kedmi, R.; Ben-Arie, N.; Peer, D. The systemic toxicity of positively charged lipid nanoparticles and the role of Toll-like receptor 4 in immune activation. *Biomaterials* **2010**, 31, (26), 6867-6875.

(246) Shao, X. R.; Wei, X. Q.; Song, X.; Hao, L. Y.; Cai, X. X.; Zhang, Z. R.; Peng, Q.; Lin, Y. F. Independent effect of polymeric nanoparticle zeta potential/surface charge, on their cytotoxicity and affinity to cells. *Cell Proliferation* **2015**, 48, (4), 465-474.

(247) Chang, K.-L.; Higuchi, Y.; Kawakami, S.; Yamashita, F.; Hashida, M. Efficient Gene Transfection by Histidine-Modified Chitosan through Enhancement of Endosomal Escape. *Bioconjugate Chem.* **2010**, 21, (6), 1087-1095.

(248) Avila, L. A.; Aps, L. R.; Sukthankar, P.; Ploscariu, N.; Gudlur, S.; Simo, L.; Szoszkiewicz, R.; Park, Y.; Lee, S. Y.; Iwamoto, T.; Ferreira, L. C.; Tomich, J. M. Branched amphiphilic cationic oligopeptides form peptiplexes with DNA: a study of their biophysical properties and transfection efficiency. *Mol. Pharm.* **2015**, 12, (3), 706-715.

(249) Hashemi, M.; Parhiz, B. H.; Hatefi, A.; Ramezani, M. Modified polyethyleneimine with histidine-lysine short peptides as gene carrier. *Cancer Gene Ther.* **2011**, 18, (1), 12-19.

(250) Luan, L.; Meng, Q.; Xu, L.; Meng, Z.; Yan, H.; Liu, K. Peptide amphiphiles with multifunctional fragments promoting cellular uptake and endosomal escape as efficient gene vectors. *J. Mater. Chem. B* **2015**, 3, (6), 1068-1078.

(251) Wang, X.; Tai, Z.; Tian, J.; Zhang, W.; Yao, C.; Zhang, L.; Gao, Y.; Zhu, Q.; Gao, J.; Gao, S. Reducible chimeric polypeptide consisting of octa-D-arginine and tetra-L-histidine peptides as an efficient gene delivery vector. *Int. J. Nanomed.* **2015**, 10, 4669-4690.

(252) Isaksson, K.; Akerberg, D.; Posaric-Bauden, M.; Andersson, R.; Tingstedt, B. In vivo toxicity and biodistribution of intraperitoneal and intravenous poly-L-lysine and poly-L-lysine/poly-L-glutamate in rats. *J. Mater. Sci.: Mater. Med.* **2014**, 25, (5), 1293-1299.

(253) Ayyappan, J. P.; Sami, H.; Rajalekshmi, D. C.; Sivakumar, S.; Abraham, A. Immunocompatibility and toxicity studies of poly-L-lysine nanocapsules in sprague-dawley rats for drug-delivery applications. *Chem. Biol. Drug Des.* **2014**, 84, (3), 292-299.

(254) Midoux, P.; Pichon, C.; Yaouanc, J. J.; Jaffres, P. A. Chemical vectors for gene delivery: a current review on polymers, peptides and lipids containing histidine or imidazole as nucleic acids carriers. *Br. J. Pharmacol.* **2009**, 157, (2), 166-178.

(255) Chen, Q.-R.; Zhang, L.; Stass, S. A.; Mixson, A. J. Co-polymer of histidine and lysine markedly enhances transfection efficiency of liposomes. *Gene Ther.* **2000**, 7, 1698-1705.

(256) Leng, Q. Modified branched peptides with a histidine-rich tail enhance in vitro gene transfection. *Nucleic Acids Res.* **2005**, 33, (4), e40-e40.

(257) Chen, Q.-R.; Zhang, L.; Stass, S. A.; Mixson, A. J. Branched co-polymers of histidine and lysine are efficient carriers of plasmids. *Nucleic Acids Res.* **2001**, 29, (6), 1334-1340.

(258) Katayose, S.; Kataoka, K. Water-Soluble Polyion Complex Associates of DNA and Poly(ethylene glycol)-Poly(l-lysine) Block Copolymer. *Bioconjugate Chem.* **1997**, 8, (5), 702-707.

(259) Liu, G.; Molas, M.; Grossmann, G. A.; Pasumarthy, M.; Perales, J. C.; Cooper, M. J.; Hanson, R. W. Biological properties of poly-L-lysine-DNA complexes generated by cooperative binding of the polycation. *J. Biol. Chem.* **2001**, 276, (37), 34379-34387.

(260) McBride, J. W.; Massey, A. S.; McCaffrey, J.; McCrudden, C. M.; Coulter, J. A.; Dunne, N. J.; Robson, T.; McCarthy, H. O. Development of TMTP-1 targeted designer biopolymers for gene delivery to prostate cancer. *Int. J. Pharm.* **2016**, 500, (1-2), 144-153.

(261) Schellinger, J. G.; Pahang, J. A.; Johnson, R. N.; Chu, D. S.; Sellers, D. L.; Maris, D. O.; Convertine, A. J.; Stayton, P. S.; Horner, P. J.; Pun, S. H. Melittin-grafted HPMA-oligolysine based copolymers for gene delivery. *Biomaterials* **2013**, 34, (9), 2318-2326.

(262) Dosta, P.; Segovia, N.; Cascante, A.; Ramos, V.; Borros, S. Surface charge tunability as a powerful strategy to control electrostatic interaction for high efficiency silencing, using tailored oligopeptide-modified poly(beta-amino ester)s (PBAEs). *Acta Biomater.* **2015**, 20, 82-93.

(263) Petros, R. A.; DeSimone, J. M. Strategies in the design of nanoparticles for therapeutic applications. *Nat. Rev. Drug Discovery* **2010**, 9, (8), 615-627.

(264) Davis, M. E. The First Targeted Delivery of siRNA in Humans via a Self-Assembling, Cyclodextrin Polymer-Based Nanoparticle: From Concept to Clinic. *Mol. Pharm.* **2009**, 6, (3), 659-668.

(265) Caravan, P. Strategies for increasing the sensitivity of gadolinium based MRI contrast agents. *Chem. Soc. Rev.* **2006**, 35, (6), 512-523.

(266) Klemm, P. J.; Floyd, W. C., 3rd; Smiles, D. E.; Frechet, J. M.; Raymond, K. N. Improving T(1) and T(2) magnetic resonance imaging contrast agents through the conjugation of an

esteramide dendrimer to high-water-coordination Gd(III) hydroxypyridinone complexes. *Contrast Media Mol. Imaging* **2012**, 7, (1), 95-99.

(267) Shiraishi, K.; Kawano, K.; Maitani, Y.; Yokoyama, M. Polyion complex micelle MRI contrast agents from poly(ethylene glycol)-b-poly(L-lysine) block copolymers having Gd-DOTA; preparations and their control of T(1)-relaxivities and blood circulation characteristics. *J. Controlled Release* **2010**, 148, (2), 160-167.

(268) Shiraishi, K.; Kawano, K.; Minowa, T.; Maitani, Y.; Yokoyama, M. Preparation and in vivo imaging of PEG-poly(L-lysine)-based polymeric micelle MRI contrast agents. *J. Controlled Release* **2009**, 136, (1), 14-20.

(269) Longmire, M. R.; Ogawa, M.; Choyke, P. L.; Kobayashi, H. Dendrimers as high relaxivity MR contrast agents. *Wiley Interdiscip. Rev.: Nanomed. Nanobiotechnol.* **2014**, 6, (2), 155-162.

(270) Ye, M.; Qian, Y.; Tang, J.; Hu, H.; Sui, M.; Shen, Y. Targeted biodegradable dendritic MRI contrast agent for enhanced tumor imaging. *J. Controlled Release* **2013**, 169, (3), 239-245.

(271) Cheng, Z.; Al Zaki, A.; Jones, I. W.; Hall, H. K., Jr.; Aspinwall, C. A.; Tsourkas, A. Stabilized porous liposomes with encapsulated Gd-labeled dextran as a highly efficient MRI contrast agent. *Chem. Commun. (Cambridge, U. K.)* **2014**, 50, (19), 2502-2504.

(272) Winter, P. M.; Pearce, J.; Chu, Z.; McPherson, C. M.; Takigiku, R.; Lee, J. H.; Qi, X. Imaging of brain tumors with paramagnetic vesicles targeted to phosphatidylserine. *Magn. Reson. Imaging* **2015**, 41, (4), 1079-1087.

(273) Chen, Y.; Zhu, Q.; Tian, Y.; Tang, W.; Pan, F.; Xiong, R.; Yuan, Y.; Hu, A. Supramolecular aggregates from polyacrylates and Gd(III)-containing cationic surfactants as high-relaxivity MRI contrast agents. *Polym. Chem.* **2015**, 6, (9), 1521-1526.

(274) Korkusuz, H.; Ulbrich, K.; Welzel, K.; Koeberle, V.; Watcharin, W.; Bahr, U.; Chernikov, V.; Knobloch, T.; Petersen, S.; Huebner, F.; Ackermann, H.; Gelperina, S.; Kromen, W.; Hammerstingl, R.; Haupenthal, J.; Gruenwald, F.; Fiehler, J.; Zeuzem, S.; Kreuter, J.; Vogl, T. J.; Piiper, A. Transferrin-coated gadolinium nanoparticles as MRI contrast agent. *Mol. Imaging Biol.* **2013**, 15, (2), 148-154.

(275) Mi, P.; Kokuryo, D.; Cabral, H.; Kumagai, M.; Nomoto, T.; Aoki, I.; Terada, Y.; Kishimura, A.; Nishiyama, N.; Kataoka, K. Hydrothermally synthesized PEGylated calcium phosphate nanoparticles incorporating Gd-DTPA for contrast enhanced MRI diagnosis of solid tumors. *J. Controlled Release* **2014**, 174, 63-71.

(276) Na, H. B.; Hyeon, T. Nanostructured T1 MRI contrast agents. *J. Mater. Chem.* **2009**, 19, (35), 6267-6273.

(277) Davies, G. L.; Kramberger, I.; Davis, J. J. Environmentally responsive MRI contrast agents. *Chem. Commun. (Cambridge, U. K.)* **2013**, 49, (84), 9704-9721.

(278) Hingorani, D. V.; Bernstein, A. S.; Pagel, M. D. A review of responsive MRI contrast agents: 2005-2014. *Contrast Media Mol. Imaging* **2015**, 10, (4), 245-265.

(279) Viger, M. L.; Sankaranarayanan, J.; de Gracia Lux, C.; Chan, M.; Almutairi, A. Collective activation of MRI agents via encapsulation and disease-triggered release. *J. Am. Chem. Soc.* **2013**, 135, (21), 7847-7850.

(280) Martinelli, J.; Fekete, M.; Tei, L.; Botta, M. Cleavable beta-cyclodextrin nanocapsules incorporating Gd(III)-chelates as bioresponsive MRI probes. *Chem. Commun. (Cambridge, U. K.)* **2011**, 47, (11), 3144-3146.

(281) Liang, G.; Ronald, J.; Chen, Y.; Ye, D.; Pandit, P.; Ma, M. L.; Rutt, B.; Rao, J. Controlled self-assembling of gadolinium nanoparticles as smart molecular magnetic resonance imaging contrast agents. *Angew. Chem., Int. Ed.* **2011**, 50, (28), 6283-6286.

(282) Rabenstein, D. L.; Robert, J. M.; Peng, J. Multinuclear magnetic resonance studies of the interaction of inorganic cations with heparin. *Carbohydr. Res.* **1995**, 278, (2), 239-256.

(283) Rej, R. N.; Holme, K. R.; Perlin, A. S. Marked stereoselectivity in the binding of copper ions by heparin. Contrasts with the binding of gadolinium and calcium ions. *Carbohydr. Res.* **1990**, 207, (2), 143-152.

(284) Vercruysse, K. P.; Li, H.; Luo, Y.; Prestwich, G. D. Thermosensitive Lanthanide Complexes of Hyaluronan. *Biomacromolecules* **2002**, 3, (4), 639-643.

(285) Taupitz, M.; Stolzenburg, N.; Ebert, M.; Schnorr, J.; Hauptmann, R.; Kratz, H.; Hamm, B.; Wagner, S. Gadolinium-containing magnetic resonance contrast media: investigation on the possible transchelation of Gd3+ to the glycosaminoglycan heparin. *Contrast Media Mol. Imaging* **2013**, 8, (2), 108-116.

(286) Passirani, C.; Barratt, G.; Devissaguet, J.-P.; Labarre, D. Long-Circulating Nanopartides Bearing Heparin or Dextran Covalently Bound to Poly(Methyl Methacrylate). *Pharm. Res.* **1998**, 15, (7), 1046-1050.

(287) Zhang, J.; Shin, M. C.; David, A. E.; Zhou, J.; Lee, K.; He, H.; Yang, V. C. Long-circulating heparin-functionalized magnetic nanoparticles for potential application as a protein drug delivery platform. *Mol. Pharm.* **2013**, 10, (10), 3892-3902.

(288) Matsumura, Y.; Maeda, H. A New Concept for Macromolecular Therapeutics in Cancer Chemotherapy: Mechanism of Tumoritropic Accumulation of Proteins and the Antitumor Agent Smancs. *Cancer Res.* **1986**, 46, (12 Part 1), 6387-6392.

(289) Fang, J.; Nakamura, H.; Maeda, H. The EPR effect: Unique features of tumor blood vessels for drug delivery, factors involved, and limitations and augmentation of the effect. *Adv. Drug Delivery Rev.* **2011**, 63, (3), 136-151.

(290) Daldrup, H.; Shames, D. M.; Wendland, M.; Okuhata, Y.; Link, T. M.; Rosenau, W.; Lu, Y.; Brasch, R. C. Correlation of dynamic contrast-enhanced MR imaging with histologic tumor grade: comparison of macromolecular and small-molecular contrast media. *Am. J. Roentgenol.* **1998**, 171, (4), 941-949.

(291) Zhou, Z.; Lu, Z. R. Gadolinium-based contrast agents for magnetic resonance cancer imaging. *Wiley Interdiscip. Rev.: Nanomed. Nanobiotechnol.* **2013**, 5, (1), 1-18.

(292) Grek, C. L.; Tew, K. D. Redox metabolism and malignancy. *Curr. Opin. Pharmacol.* **2010**, 10, (4), 362-368.

(293) Chaiswing, L.; Oberley, T. D. Extracellular/Microenvironmental Redox State. *Antioxid. Redox Signaling* **2009**, 13, (4), 449-465.

(294) Najer, A.; Wu, D.; Bieri, A.; Brand, F.; Palivan, C. G.; Beck, H.-P.; Meier, W. Nanomimics of Host Cell Membranes Block Invasion and Expose Invasive Malaria Parasites. *ACS Nano* **2014**, 8, (12), 12560-12571.

(295) Najer, A.; Thamboo, S.; Duskey, J. T.; Palivan, C. G.; Beck, H.-P.; Meier, W. Analysis of Molecular Parameters Determining the Antimalarial Activity of Polymer-Based Nanomimics. *Macromol. Rapid Commun.* **2015**, 36, (21), 1923-1928.

(296) Grant, D.; Long, W. F.; Williamson, F. B. Infrared spectroscopy of heparin-cation complexes. *Biochem. J.* **1987**, 244, (1), 143-149.

(297) Bogdan, N.; Rodriguez, E. M.; Sanz-Rodriguez, F.; de la Cruz, M. C.; Juarranz, A.; Jaque, D.; Sole, J. G.; Capobianco, J. A. Bio-functionalization of ligand-free upconverting lanthanide doped nanoparticles for bio-imaging and cell targeting. *Nanoscale* **2012**, 4, (12), 3647-3650.

(298) Aguiar, K. R.; Santos, V. G.; Eberlin, M. N.; Rischka, K.; Noeske, M.; Tremiliosi-Filho, G.; Rodrigues-Filho, U. P. Efficient green synthesis of bis(cyclic carbonate)poly(dimethylsiloxane) derivative using CO2 addition: a novel precursor for synthesis of urethanes. *RSC Adv.* **2014**, 4, (46), 24334.

(299) Yang, Z.; Tu, Q.; Wang, J.; Huang, N. The role of heparin binding surfaces in the direction of endothelial and smooth muscle cell fate and re-endothelialization. *Biomaterials* **2012**, 33, (28), 6615-6625.

(300) Vexler, V. S.; Clément, O.; Schmitt-Willich, H.; Brasch, R. C. Effect of varying the molecular weight of the MR contrast agent Gd-DTPA-polylysine on blood pharmacokinetics and enhancement patterns. *J. Magn. Reson. Imaging* **1994**, 4, (3), 381-388.

(301) Chatterton, N.; Gateau, C.; Mazzanti, M.; Pecaut, J.; Borel, A.; Helm, L.; Merbach, A. The effect of pyridinecarboxylate chelating groups on the stability and electronic relaxation of gadolinium complexes. *Dalton Trans.* **2005**, (6), 1129-1135.

(302) Nicolle, G. M.; Tóth, É.; Schmitt-Willich, H.; Radüchel, B.; Merbach, A. E. The Impact of Rigidity and Water Exchange on the Relaxivity of a Dendritic MRI Contrast Agent. *Chem. - Eur. J.* **2002**, 8, (5), 1040-1048.

(303) Dunand, F. A.; Borel, A.; Helm, L. Gd(III) based MRI contrast agents: improved physical meaning in a combined analysis of EPR and NMR data? *Inorg. Chem. Commun.* **2002**, 5, (10), 811-815.

(304) Kellar, K. E.; Henrichs, P. M.; Hollister, R.; Koenig, S. H.; Eck, J.; Wei, D. High relaxivity linear Gd(DTPA)-polymer conjugates: The role of hydrophobic interactions. *Magn. Reson. Med.* **1997**, 38, (5), 712-716.

(305) Perazella, M. A. Current status of gadolinium toxicity in patients with kidney disease. *Clin. J. Am. Soc. Nephrol.* **2009**, 4, (2), 461-469.

(306) Lauffer, R. B. Paramagnetic metal complexes as water proton relaxation agents for NMR imaging: theory and design. *Chem. Rev. (Washington, DC, U. S.)* **1987**, 87, (5), 901-927.

(307) Thielbeer, F.; Chankeshwara, S. V.; Johansson, E. M. V.; Norouzi, N.; Bradley, M. Palladium-mediated bioorthogonal conjugation of dual-functionalised nanoparticles and their cellular delivery. *Chem. Sci.* **2013**, 4, (1), 425-431.

(308) Sistach, S.; Rahme, K.; Pérignon, N.; Marty, J.-D.; Viguerie, N. L.-d.; Gauffre, F.; Mingotaud, C. Bolaamphiphile Surfactants as Nanoparticle Stabilizers: Application to Reversible Aggregation of Gold Nanoparticles. *Chem. Mater.* **2008**, 20, (4), 1221-1223.

(309) Barbosa, I.; Garcia, S.; Barbier-Chassefière, V.; Caruelle, J.-P.; Martelly, I.; Papy-Garcia, D. Improved and simple micro assay for sulfated glycosaminoglycans quantification in biological extracts and its use in skin and muscle tissue studies. *Glycobiology* **2003**, 13, (9), 647-653.

(310) Barge, A.; Cravotto, G.; Gianolio, E.; Fedeli, F. How to determine free Gd and free ligand in solution of Gd chelates. A technical note. *Contrast Media Mol. Imaging* **2006**, 1, (5), 184-188.

Acknowledgments

Pursuing my PhD studies at the University of Basel brought me in contact with many dedicated scientists to whom I express my sincere thanks. First of all, I would like to thank Wolfgang Meier for giving me the opportunity to conduct inspiring research projects in his group and giving me the freedom to develop and establish as a critical researcher. Also, I would like to thank Cornelia Palivan for all her support and advice.

Further, I like to thank Nico Bruns for discussions, sharing his experiences, and his interest in my research, accepting the co-examination of my PhD thesis.

I would like to acknowledge Dirk deBruyn and Thomas Schuster for a nice introduction to the world of peptide self-assemblies and for sharing their expertise.

Moreover, I am very grateful to Viktoriia Postupalenko and Jason Duskey for their help in the lab, sharing their expertise, and for fruitful discussions. Jason I thank in particular for revising manuscripts, proposals, and parts of the thesis. I also thank Jens Gaitzsch, Gesine Gunkel-Grabole, Andrea Gomez, and Lionel Maurizi for revising parts of the thesis. Further, I thank Corey Rice for revising proposals.

I would like to thank my collaborator Francesco Santini from the University Hospital for nice discussions and MRI measurements. Further, I thank Adrian Najer for support with FCS and FCCS measurements and for discussions and help with manuscripts. I would like to thank Florian Seebeck for access to the peptide synthesizer, Gabi Persy for TEM micrographs, Eva Bieler and Marcel Düggelin from the microscopy facility for SEM and EDX measurements, Dimitrios Tsakiris from the University Hospital for anticoagulation assays, Judith Kobler Waldis from the department Umweltwissenschaften for ICP-OES analysis, and Janine Zankl for the introduction and assistance with FACS. I thank Gianni Morson, Ursula Sauder, and Vesna Olivieri for introduction and assistance with TEM and the whole microscopy facility for access and support.

Further, I would like to thank all current and former group members and officemates Fabian Itel, Juan Liu, Evgeniia Konishcheva, Justyna Kowal, Martin Rother, Bernadetta Gajewska, Samuel Lörcher, Serena Rigo, Kaspar Renggli, Patric Baumann, Pascal Tanner, Martin

Nussbaumer, Pascal Richard, Sagana Thamboo, Tomaz Einfalt, Mihai Lamora, Adrian Dinu, Roland Goers, Martina Garni, and Christoph Edlinger for a good working atmosphere in- and outside the labs.

I would like to thank the administrative and technical staff Jean-Pierre Ramseyer, Daniela Tischhauser, Maja Greuter, Michael Devereux, and Sven Kasper, also for Döner Büx. A special thank goes to Grischa Martin and Philipp Knöpfel from the workshop for help with mechanic related issues.

I am grateful to my family, friends, and skiing-, hiking-, traveling-, diving-, and concertmates.

Many thanks to Pink Floyd, the lab DJs, and Radio Paradise for an eclectic music mix in the labs.

Finally, I would like to acknowledge financial support by freiwillige akademische Gesellschaft Basel and Gebert Rüf Foundation.